UNIVERSITY OF CALIFORNIA

SANTA CRUZ

DESIGNS OF NITROGEN DONATING LIGANDS IN METAL ORGANIC POLYMERIC ANION EXCHANGERS AND IRON-BASED COORDINATION POLYMERS

A dissertation submitted in partial satisfaction

of the requirements for the degree of

DOCTOR OF PHILOSOPHY

in

CHEMISTRY

by

Eaindar Soe

December 2018

The Dissertation of Eaindar Soe is approved:

_____

Professor Scott R J. Oliver, Advisor

_____

Professor Shaowei Chen, Chair

_____

Professor Yat Li

_____

Lori Kletzer
Vice Provost and Dean of Graduate Studies

Table of Contents

List of Figures

Lists of Tables

List of Schemes

Dedication to

my family

Acknowledgments

I offer my enduring gratitude to the faculty, staff and my fellow students at the UCSC, who have inspired me to continue my work in this field. I owe thanks to my supervisor Dr. Scott R. J. Oliver, for his motivation, guidance, encouragement, patience, and financial support. His immense knowledge and enthusiasm and positive attitude towards science set a pattern for me. I could not have imagined having a great advisor and mentor for my Ph.D. study. I would also like to thank my committee members Dr. Shaowei Chen, Dr. Yat Li for their encouragement and insightful comments.

I want to thank my dearest family. My husband, Ye Nay Myo, my son, Eric Naymyo, my parents as well as my mother-in-law. Their love, support, and endless patience have taught me so much about sacrifice and compromise. I also want to thank Brenda Andrade and Judith Alvarado-Kim for being energetic and inspiring women chemists whom I can look up to. Without them, this effort would have been worth nothing.

I would like to thank all the fellow lab mates in Oliver research group: Ian Colinas, Jesse Hauser, Ana Chatenever, Yashar Abdollahian, Beatriz Elkhe and Judith Kim who have helped and encouraged me during the last five years. My sincere thanks to Dr. Indranil, Professor Allen Oliver and Professor Timothy Johnstone for their crystallography expertise contribution to this thesis.

CHAPTER (1)

Silver(I) Coordination Polymers and Iron-based Metal Organic Frameworks for Anion Exchange, Photoluminescence and Electrocatalysis

Abstract

Molecules are architectures of atoms, while crystal engineering of crystalline solids deals with targeted structures built from molecules. As the prototype of polymeric crystal engineering, coordination polymers (CPs), in some cases also described as metal–organic frameworks (MOFs), are an intriguing class of hybrid materials, which exist as infinite crystalline lattices extended from inorganic vertices (metal ions or clusters) and organic ligand supports by coordination interactions. The last decade has seen enormous research efforts in the syntheses and studies of coordination polymers. However, the emphasis is placed on the investigations of structural properties and potential applications of cationic coordination polymers such as anion exchange, photoluminescence, and electrocatalysis. In particular, silver(I) coordination polymers have established much attention due to its flexible coordination sphere which affords diverse topologies and dimensionalities. Besides the versatility of silver coordination geometry, synthesis of organic ligands represents equally important factors in the assembly process. Because of the facile formation of Ag-N bonds, N-donor containing ligands have widely been studied. Ag-ligand interactions are labile, which allows the silver CPs to control structural modifications for guest removal or ion exchange properties. Another interesting factor is that the presence of ligands and

metal ions linked in the crystal structure allows for various possible excitation/emission scenarios which also provide photoluminescence processes. Lastly, transitional metal coordination polymers can be controlled via synthesis by their pore size, crystallinity and availability of various functional groups which made them attractive as electrochemical storage materials for fuel cells.

1.1 Design of Coordination Polymers

Coordination polymers (CPs) are compounds that consist of metals or metal clusters coordinated to multifunctional organic ligands, and they have been studied for several decades. The ligand must be a bridging organic group. The metal atoms must solely be bridged by this organic ligand in at least in one extended dimension. Furthermore, at least one carbon atom must lie between the donor atoms (Figure 1.1). However, it was not until the early 1990s that systematic crystal-engineering approaches were adopted for the design of CPs. Shortly thereafter it was realized that porous coordination polymers (PCPs), also commonly known as metal-organic frameworks (MOFs), offer diverse porosity in the context of crystalline materials. Nowadays, CPs are often regarded as one-dimensional chains and two-dimensional (2D) layered structures whereas MOFs refer to high porosity three-dimensional (3D) networks.[1] In this regard, the possible applications arising from the remarkable physicochemical properties of CPs are widely recognized in gas adsorption, molecular/ionic separation, optics, electricity, magnetism, chirality, catalysis, and drug delivery.[2–6]

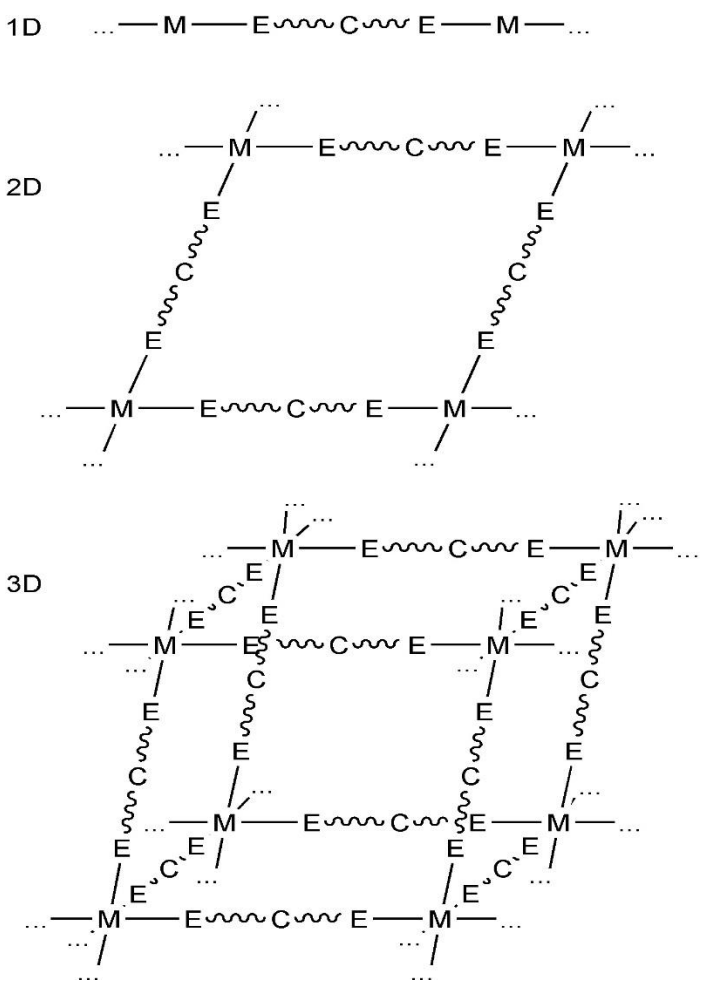

Figure 1.1: Schematic representation of the definition of 1D, 2D or 3D coordination polymers having organic bridging ligands with at least one carbon atom in between the donor atoms (E). Donor atoms (E) include O, N, S, P.

1.2 Cationic or Transitional Metal Coordination Polymers

A large range of accessible properties, both geometric and electronic in nature, are displayed by transition metals. Because their chemistry is well documented, they can be conveniently incorporated into coordination polymers. In terms of physically incorporating transition metals into CPs, there are two

approaches.[7] First, one can use them as building blocks to direct a certain framework topology, and second, they can be chosen based on their electronic functionality, such as for magnetism or redox potential. Both of these approaches can also be targeted together in the one material. The most commonly reported transition metals in CPs are those which show labile metal–ligand bonds, such as manganese, iron, cobalt, nickel, copper, zinc, palladium, silver, cadmium, gold and mercury. Typical coordination geometries that are seen in transition metals in coordination polymers include linear to octahedral (Figure 1.2). Thus, transition metals can be used as building blocks ranging from 2- to 6-connecting. For each metal ion and its respective oxidation state, the possible coordination geometries are well established so that particular ones can be targeted. For example, in CPs where linear linking metals are required, Ag^{+}, Au^{+} and Hg^{+} are often employed, whereas for square planar geometry Pt^{2+} and Pd^{2+} are common and for even greater coordination numbers $Mn^{2+/3+}$, $Fe^{2+/}Fe^{3+}$, $Co^{2+/3+}$ and Ni^{2+} can be targeted.

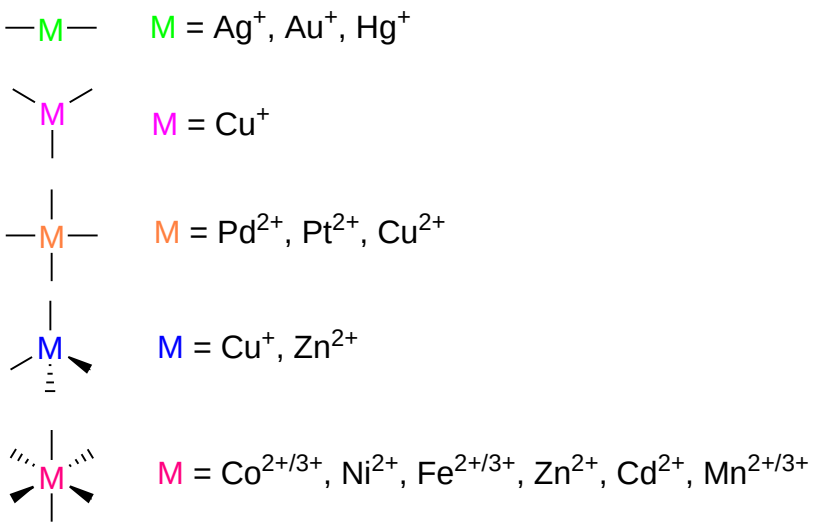

Figure 1.2: Illustration of some transition metal coordination environments and common metals that form them. Recreated from Batten *et al*.[7]

The properties of silver metal CPs will be briefly introduced and discussed with particular examples and will be outlined in more detail in the following chapter.

1.3 Silver(I) Coordination Polymers

Assembly of silver(I) coordination polymers (Ag CPs) has received massive attention in recent decades as being one of the most exciting research fields in supramolecular coordination chemistry.[8,9] Due to its flexible coordination sphere, the Ag^+ ion exhibits abundant coordination geometries, varying from linear to octahedral, corresponding to coordination numbers 2 to 6. Such coordination flexibility contributes to the structural diversity and dimensionalities of the Ag CPs, where 1D, 2D, and 3D network have been created. In addition, the flexibility of the Ag^+ coordination sphere affords the opportunity to study the mechanism of the self-

assembly process since Ag-ligand interactions are labile and even slight change of reaction conditions may change the topological structures. The role of many influencing factors, such as the functionality of the ligand, the ligand-to-metal ratio, the counter anion, the solvent, and the noncovalent interactions, have been widely studied in the self-assembly process of Ag CPs.

1.3.1 One- to Three-Dimensional Silver(I) Coordination Polymers

Comparing with other coordination polymers, silver(I) CPs have diverse coordination geometries varying from linear trigonal, tetrahedral, square planar, square pyramidal, and octahedral, in which the coordination number of the Ag^+ ion ranges from 2 to 6. Ag^+ ion with coordination number 2 comprises the most common mode in Ag CPs, which exhibit linear or bent coordination geometries. They can act as either a two-connecting node or a linear connector, thus resulting in a large number of Ag CPs, depending on the ligand with topologies varying from 1D to 3D framework (Figure 1.3). Among several numbers of CPs reported based on Ag^+, some significant studies will be reported in the following categories.

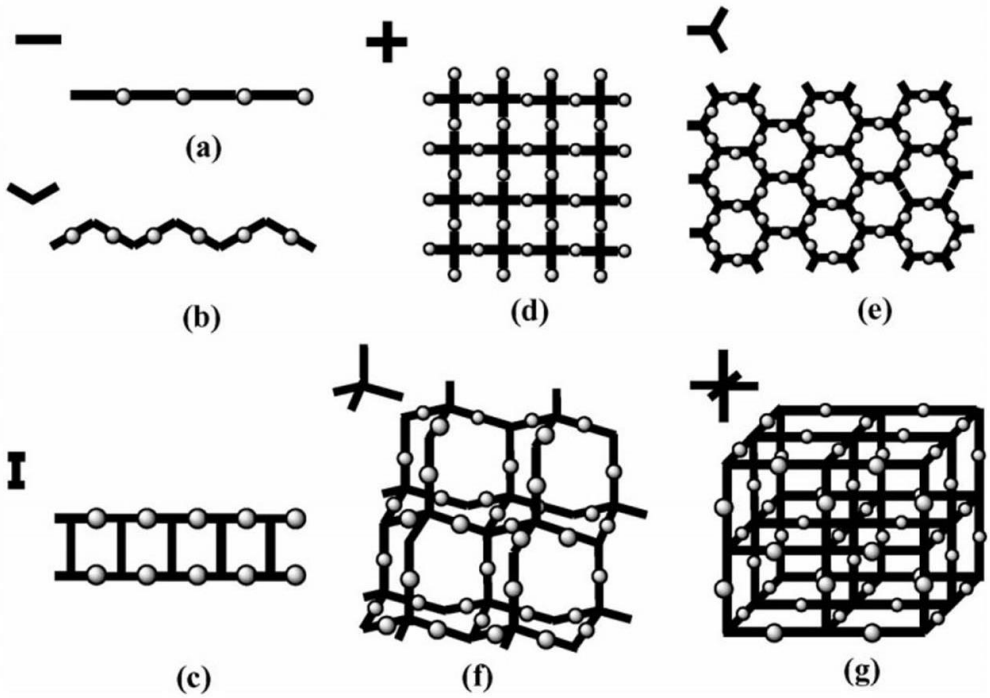

Figure 1.3: Silver(I) coordination polymers based on the two-coordinating Ag^+ ion: (a) linear chain; (b) zigzag chain; (c) ladder-like chain; (d) (4,4) net; (e) (6,3) net; (f) diamond net; (g) cubic net.[10]

An infinite 1D chain is the simplest and most common structural topology of Ag(I) CPs. However, the simple 1D chain can diversify in two ways (Figure 1.3a, 1.3b). One type is based on the connection mode and the shape of 1D chains. Such structural diversity is related to silver ion coordination geometry, ligand dentation and the metal-to-ligand ratio. The other type is caused by the twist and alignment of 1D chains in crystal packing. One example is SLUG-21, Ag_2(4,4′-bipyridine)$_2$ ($O_3SCH_2CH_2SO_3$)·$4H_2O$, a silver-based 1D cationic polymer synthesized by our group. The Ag is connected to 4,4′-bipyridine (bipy) as linker and 1,2-ethanedisulfonate (EDS) as a template. The Ag-bipy layer is defined by 4,4′-bipy ligand π-π stacking between adjacent 1D chains. The Ag(I) atoms with full d shell

form a linear geometry with Ag-N bond lengths in the range 2.156(6)-2.170(7) Å. Each end of the EDS molecule interacts electrostatically with adjacent cationic layers through one sulfonate oxygen, with Ag-O distances between 2.711(7) and 2.759(9) Å (Figure 1.4).

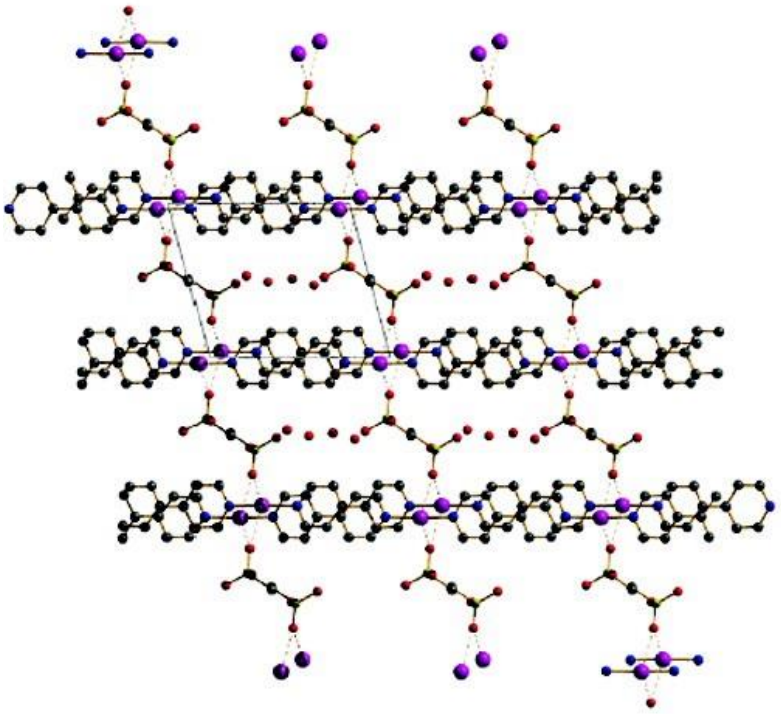

Figure 1.4: Crystallographic *a*-projection of 1D silver cationic CP, SLUG-21.[11]

Following the node and connector approach, the multifunctional ligands have successfully yielded a number of 2D Ag(I) CPs. Two typical 2D net topologies are the square grid (4,4) net and the honeycomb (6,3) net (Figure 1.3d, 1.3e). These networks can be assembled from the three-coordinate Ag^+ ion. A good example is $[(AgL)(PF_6)]_\infty$ (L = 2,5-bis(4-pyridyl)-1,3,4-thiadiazole), synthesized by Huang *et al.*[12] and possessed a three-connected ($4,8^2$) topology (Figure 1.5).

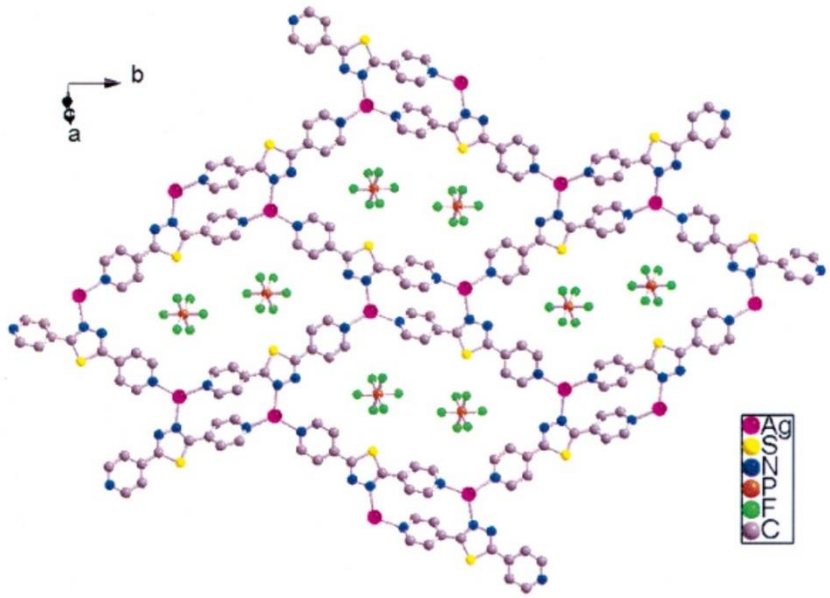

Figure 1.5: 2D (2/4,3) network of $[(AgL)(PF_6)]_\infty$ including the interior anions. Hydrogen atoms are omitted for clarity.[12]

The Ligand L is bridged three adjacent Ag(I) centers in a tridentate coordination fashion to generate a non-interpenetrating 2D network consisting of two types of metalacyclic grids. Two Ag(I)centers are linked by one L using two pyridyl N atoms to form the longer edge of a parallelogram.

Compared with 1D and 2D structures, the 3D Ag(I) CPs are expected to be more difficult to fabricate in a predictable way because of the highly flexible coordination geometry of the Ag^+ ions. Due to the flexibility of the Ag^+ environment, it is possible to engineer some typical 3D frameworks, including diamond or cubic nets, if reaction conditions are controlled properly (Figure 1.3f, 1.3g). The 3D silver complexes of diamondoid topology can be designed by four-coordinate Ag^+ in its tetrahedral coordination geometry. For example, this 3D polymeric complex with a

(10,3)-α type topology has been assembled using silver nitrate and the ligand diquinoxalino-2',3'-phenazine in a one pot synthesis.[13] In this structure, each Ag^+ ion is coordinated with four N donors from two different ligands in a distorted tetrahedral fashion, thus simplified as two-connecting linkers while each ligand coordinates to three Ag^+ ions as a tris(bidenate) ligand, acting as three-connecting nodes (Figure 1.6).

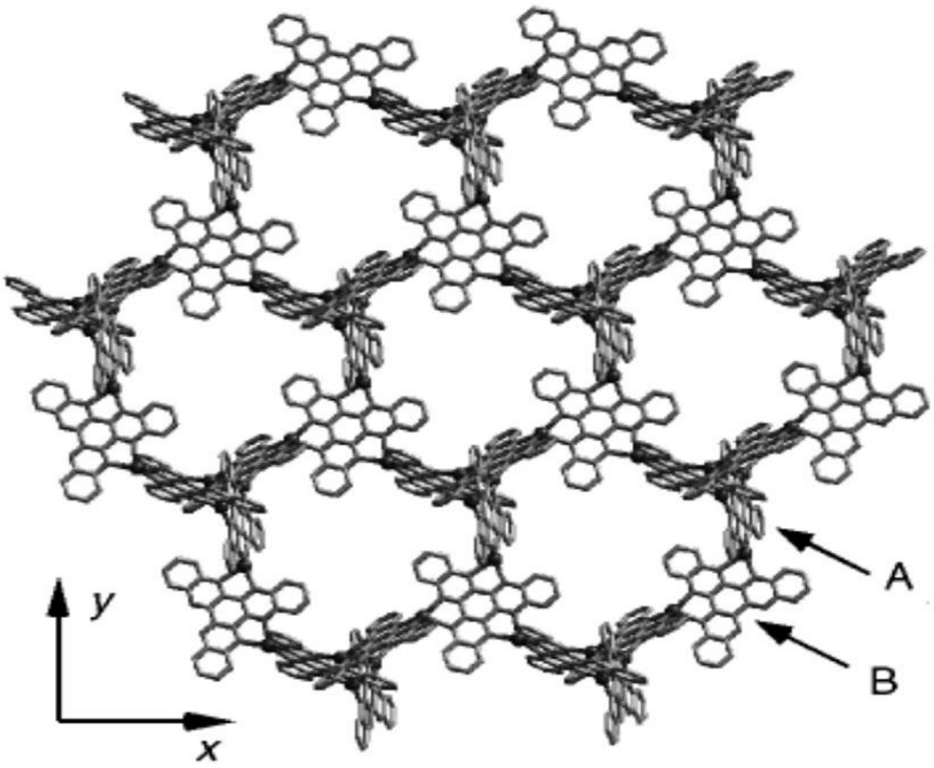

Figure 1.6: A representation of a single 3D network where two type of ligand arrangement are labeled as A and B.[13]

1.4 Silver(I) Coordination Polymers for Anion-Exchange Applications

1.4.1 Ligands

Besides the versatility of Ag^+ coordination geometry, design and synthesis of organic ligands represent more important factors in the assembly of diversified silver(I) CPs with desired structures and concomitant properties. By careful selection of specific ligands containing specific coordination donors and displaying adjustable conformations, a large number of silver(I) CPs have been generated from either a single ligand or from mixed ligands under controlled reaction conditions.[14] To design organic ligands for assembly of Ag(I) CPs, N, P, O or S atoms are usually chosen as the donors, as they contain one or more lone electron pairs to coordinate readily with an Ag^+ ion.

N-Donor-Containing Ligands

Among those ligands, N-donor-containing ligands have been widely exploited in the self-assembly Ag(I) CPs because of their facile formation of Ag-N bonds. The commonly used nitrogen ligands are pyridyl, imidazolyl, pyrazine, 4,4'-bipyridine and quinoxaline (Figure 1.7). Due to the N atom in these terminal groups having only one lone electron pair, at least two N donors usually coordinates an Ag^+ ion in one or more directions. These ligands can be classified conventionally as bidentate, tridentate and so on, depending on the number of coordinating N donors. For example, when 4,4'-bipyridine coordinates Ag^+ ion through two N donors, it acts as a bidentate ligand functionalizing as a perfect linear linker in many Ag(I) CPs. The

formation process of Ag^+ coordination complexes based on N-donor-containing ligands is normally reversible because the Ag-N donor dative bonds are labile, which makes the Ag^+ polymeric complexes generally crystallizable and ready for single-crystal X-ray diffraction analysis as well as excellent for ion exchange.

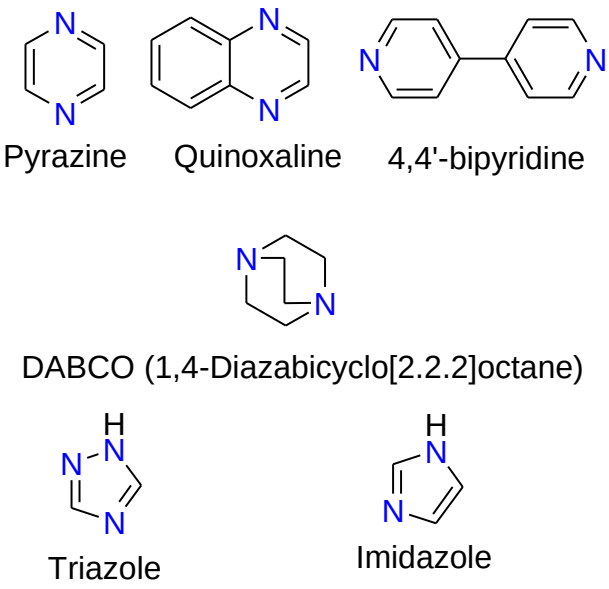

Figure 1.7: Most commonly used N-donor-containing ligands.

1.4.2. Anion Exchange Studies

Flexible/dynamic porous materials can be generated through the linking of flexible moieties with strong bonds (organic or inorganic) together with weaker bonds (i.e. π–π stacking, hydrogen bonding, and van der Waals interactions). The concept is that weaker interactions, such as π–π stacks, hydrogen bonds and van der Waals forces provide stability intrinsic to retaining porosity allowing concerted structural modifications to occur with guest removal and replacement.[15] The guest or charge-balancing anions located in the cavities or channels of porous silver(I) CPs can be

removed without causing collapse of the framework, or can be reinserted in some cases. Selective intercalation of guests is also reported for Ag CPs.

1.4.3. Silver(I)-Nitrogen Containing CPs for Anion Exchange

One of the interesting Ag(I) CPs for ion exchange was reported by the Shimizu group in 2005. The Ag(I) CP, $[Ag(4\text{-pyridinesulfonate})]_{\infty}$, is like a hybrid inorganic-organic solid, having a continuous rather than open grid structure, however, in contrast, the organic units are incorporated into the layer itself, as in coordination solids.[16]

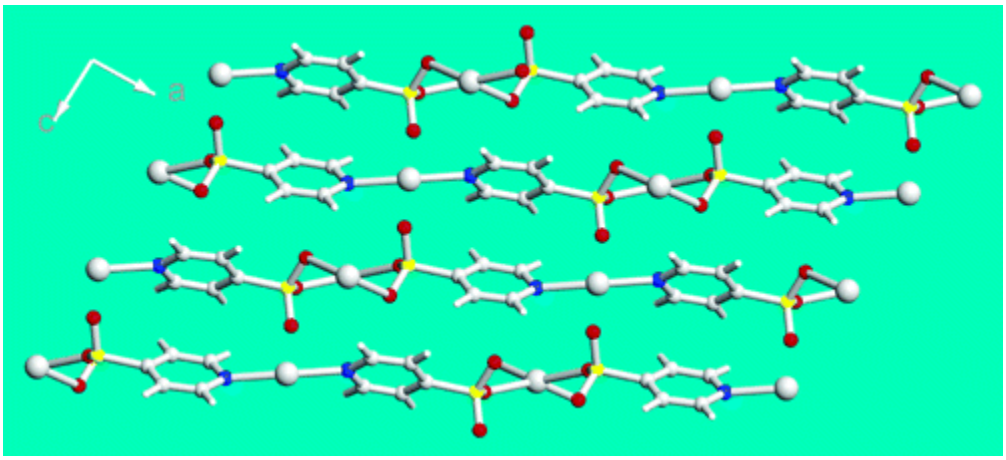

Figure 1.8: Ball-and-stick view of $[Ag(4\text{-pyridinesulfonate})]_{\infty}$ looking in the plane of the layers showing the relative orientation of four adjacent sheets.[16]

As shown in Figure 1.8, the layers can be described as bricks of $[Ag(L)_2]^-$ units cross-linked both horizontally and vertically by Ag^+ ligation to the sulfonate groups. Two types of silver ion are present in equal ratios; those which coordinate in a linear fashion to the pyridine moieties, and those which bridge sulfonates groups in a distorted tetrahedral manner. Notably, despite the perception of sulfonates as poor

ligands, the layers are robust and remain intact even in the presence of an equivalent of Lewis basic amine intercalates. This amine intercalation is highly selective for primary > secondary > tertiary amines and confirmed by PXRD (Figure 1.9).

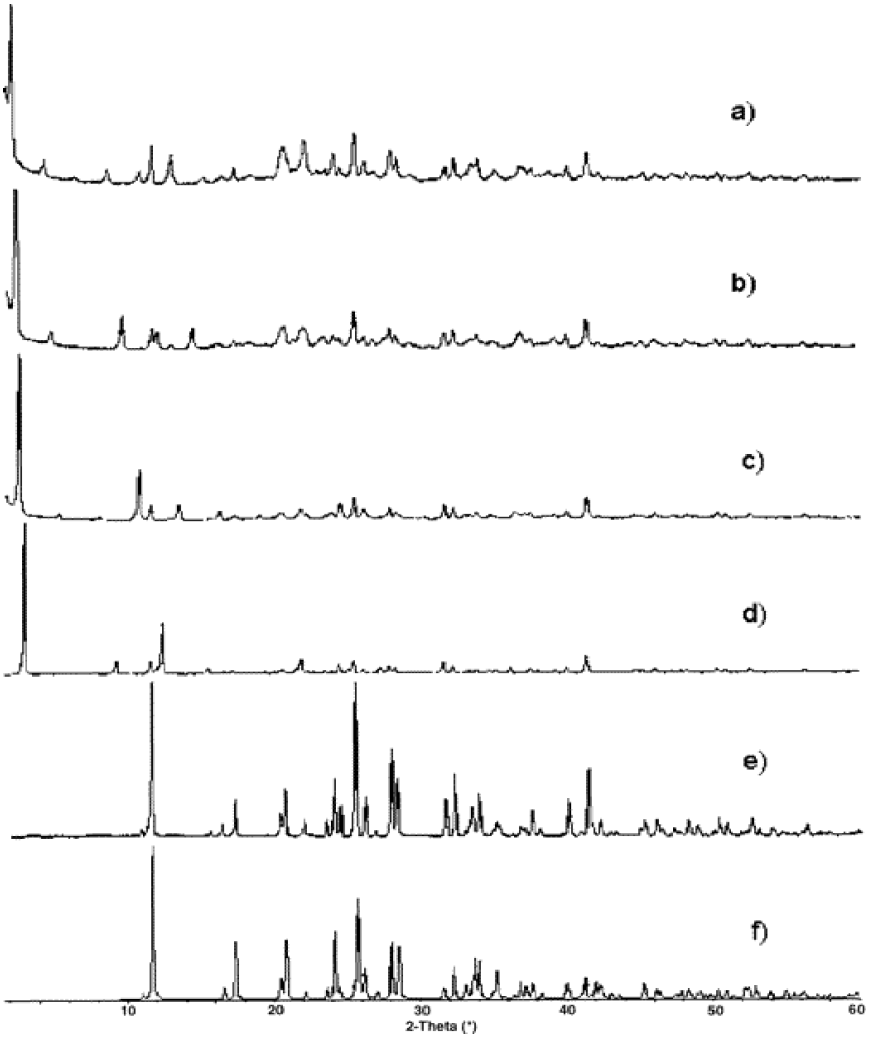

Figure 1.9: PXRD patterns for [Ag(4-pyridinesulfonate)]$_\infty$ exchanges with (a) tetradecylamine; (b) dodecylamine; (c) decylamine; (d) octylamine; (e) as-synthesized and (f) simulated from single-crystal data.[16]

To determine whether the intercalation was selective, the sorption experiments were repeated using guests containing other functional groups. In the presence of straight chain alkanes, nitriles, alcohols, and aldehydes, as well as benzene, toluene, and mesitylene, no guest uptake was observed. It can also reversibly generate one cycle to the parent host upon heating (PXRD data was not reported in the article).

The series of cationic Ag(I) bipyridine CPs, $[Ag\text{-}bipy]^{+}[X^{-}]$ (bipy = 4,4'-bipyridine) were developed by our group[17–20] and others[21–23] for their potential use in anion exchanges where (X^{-} = NO_3^{-}, ClO_4^{-}, BF_4^{-}, $CH_3CO_2^{-}$, $^{-}O_3S\text{-}R\text{-}SO_3^{-}$, CrO_4^{2-}, MnO_4^{-} or ReO_4^{-}). The following data (Table 1.1) represents Ag(I) bipyridine CPs for anion exchange that were reported by our group.

Table 1.1: Anions Adsorption Data for Reported Ag(I) bipyridine CPs

Ag(I) CPs	Target Anions	Adsorption Capacity (mg/g)	Equilibrium Time	Selectivity
SLUG-21[17]	MnO_4^-	283	48 h	NO_3^-, CO_3^{2-}
SLUG-21[17]	CrO_4^{2-}	60	48 h	NO_3^-, CO_3^{2-}
SBN[18]	ClO_4^-	354	1.2 h	LDH & commercial resins
SBN[23]	ReO_4^-	786	2 h	LDH & commercial resins
SBA[20]	ClO_4^-	310	0.5 h	LDH & commercial resins
SBA[20]	ReO_4^-	705	48 h	various anions
SBA[20]	MnO_4^-	351	48 h	various anions
SBA[20]	CrO_4^{2-}	160	48 h	various anions

Previously, our group created the design of an Ag(I) CP, referred to as SLUG-21, that exhibist excellent uptake of toxic oxyanions with outstanding selectivity.[17] It

consists of chains of alternating Ag(I) and 4,4'-bipyridine that π-π stack into cationic layers (Figure 1.10). The layers are charge balanced by ethanedisulfonate (EDS) anions and selectively exchange for permanganate, chromate and perrhenate, with a significantly high adsorption capacity of 292, 60 and 602 mg/g, respectively.[17] Reversibility in the uptake of oxyanions including perchlorate remained a challenge due to the lower affinity for alkylsulfonates.

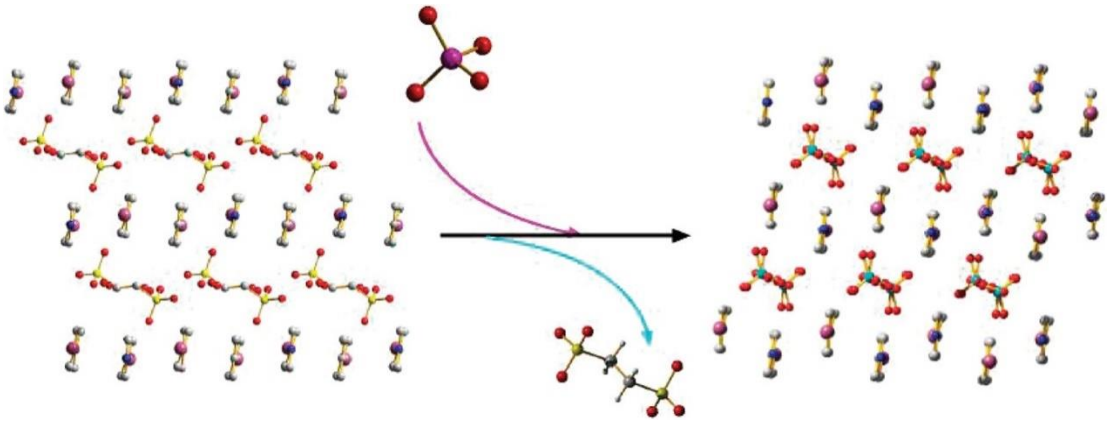

Figure 1.10: (Left) Crystallographic *a*-projection of (left) the SLUG-21 structure; (right) the crystal structure after perchlorate anion exchange.

Another interesting silver-bipyridine polymer, $[Ag(bipy)^{+}(NO_3)^{-}]$ (SBN), was previously synthesized by Yaghi;[21] later our group exclusively reported its preference for perchlorate (ClO_4^{-}) over nitrate, allowing for rapid exchange from ppm level perchlorate in contaminated water.[18] Regeneration of the nitrate form can occur offline in excess nitrate to obtain a concentrated perchlorate waste form. The anion preference can be understood by considering the SBN and $[Ag(bipy)^{+}(ClO_4)^{-}]$ SBP crystal structures (Figure 1.11).

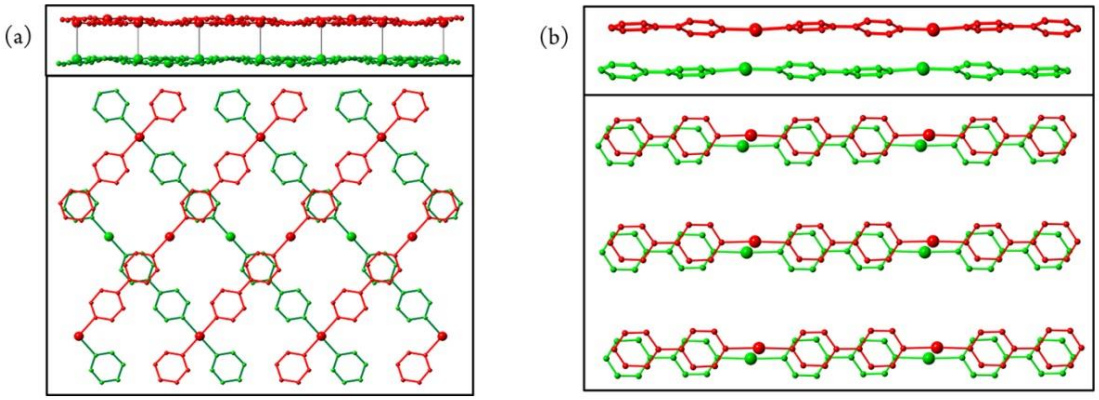

Figure 1.11: Crystallographic views of two [Ag-bipy+] "layers" (top in red, bottom in green; corresponding side views shown at top; anions and hydrogens omitted for clarity). (a) SBN and (b) SBP. [18]

For both, each Ag(I) is chelated by the nitrogens of two different 4,4′-bipyridine units, forming extended polymeric chains. For SBN, another layer is rotated by 90° (Figure 1.11a), whereas for SBP, the layers are eclipsed (Figure 1.11b). For SBN, only half of the pyridine rings did π-π stack in a staggered formation to the adjacent layer (Figure 1.11a, average distance 3.55 Å), while SBP formed all pyridine rings in eclipsed formation. (Figure 1.11b, average distance 3.47 Å). They reported that these two structures transform reversibly and are a consequence of the shape of the incoming anion that must pack between the cationic polymers. Nitrate is flat, and perchlorate is tetrahedral (spheroidal). Both structures are stoichiometrically equivalent, with one mole of the monomeric anion in their formulas. The anion oxygen-to-silver distances are typical of ionic bonding for SBN; however, half π-stacking for SBP. Therefore, SBP is more stable and accounts for rapid exchange of

nitrate for very dilute perchlorate. This perchlorate-nitrate cycling (each cycle 24 h) shows continued excellent reversibility up to seven cycles and were reported by ion chromatography (IC) in Table 1.2.

Table 1.2: Adsorption capacity of perchlorate trapping cycles by SBN

Cycle no.	**1st**	**2nd**	**3rd**	**4th**	**5th**	**6th**	**7th**
mg SBP/g SBN	344.36	264.93	248.63	243.05	329.86	216.35	195.59

SBN was also tested for selective perchlorate capture in the presence of multiple-fold excess of potentially competing common anions such as hydrotalcite ($Mg_6Al_2(CO_3)(OH)_{16}\cdot 4H_2O$, Ni_3Al-LDH (layered double hydroxides), Purolite A530E, and Amberlite IRA-400 resin (Figure 1.12).

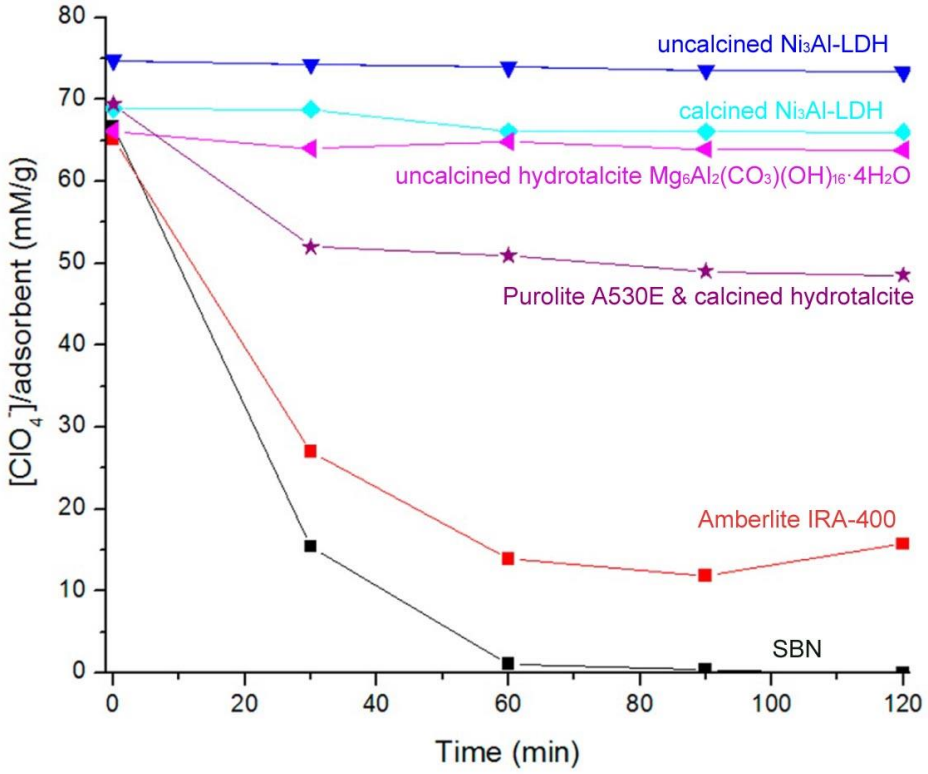

Figure 1.12: Perchlorate uptake by gram of solid versus time by IC.[18]

A rapid decrease of approximately 98% of the perchlorate concentration was observed within 60 min for SBN. In the case of the other anion exchangers, only Amberlite showed a significant 78% perchlorate uptake, versus 4-12% for calcined hydrotalcite and Ni_3Al-LDH.

Recently, SBN has also been shown to be an excellent exchange material for the capture and immobilization of perrhenate (ReO_4^-), a surrogate for the radioactive contaminant pertechnetate ($^{99}TcO_4^-$) in a nice study by Zhu *et al.*[23] They compared the SBN to anion exchange materials (Mg-Al-LDH, NDTB-1, $Yb_3O(OH)_6Cl$, and

Purolite A532E resin) that were specifically designed for TcO_4^-/ReO_4^- uptake and found that while the resins reached their sorption capacity in 2 hours, SBN could reach its capacity in 10 min. Additionally, after 12 hours, the SBN reached a ReO_4^- loading of 714 mg/g, which is more than all other sorbent materials tested (Figure 1.13). Finally, they tested perrhenate uptake at a variety of pH levels and found excellent capacity in a solution with a pH as low as 3 and as high as 9.

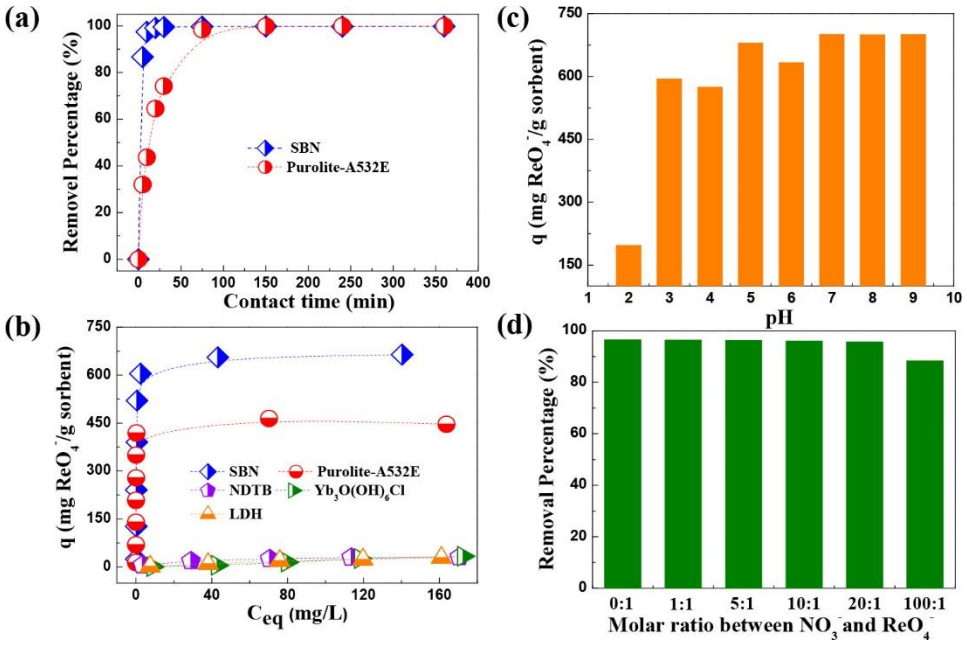

Figure 1.13: (a) Sorption kinetics data of ReO_4^- into SBN and A532E. (b) Sorption isotherms of ReO_4^- by SBN compared with LDH, NDTB-1, Purolite-A532E, and $Yb_3O(OH)_6Cl$ materials. (c) Effect of pH on the sorption of ReO_4^- into SBN. (d) Effect of competing NO_3^- on the uptake of ReO_4^- by SBN.[23]

The irreversibility in this case is due to the solubility differences between SBN and $[Ag(bipy)^+(ReO_4)^-]$ (SBR). Whereas SBN was originally reported as having a solubility of 0.80 mmol/L, corresponding to a $K_{sp} = 5.12 \times 10^{-10}$, the solubility product found for SBR was as small as 2.16×10^{-13}. This, of course, is beneficial as

effective trapping and containment of nuclear waste is currently the best mode of remediation. The solubilities can likely be, at least somewhat, attributed to the structures of the materials, where the SBR (obtained by single-crystal-to-single-crystal exchange) is a head-to-tail co-linear arrangement of the polymers, which should have more structural durability than the previously described SBN (Figure 1.14).

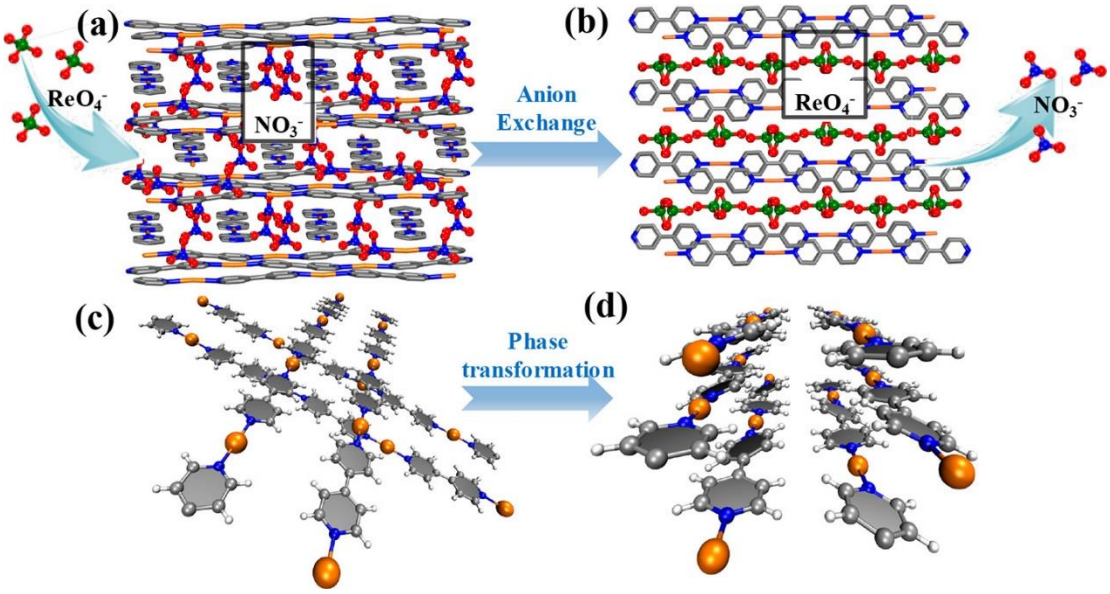

Figure 1.14: Crystal structures of SBN (a) and SBR (b) showing a single-crystal to single-crystal structural transformation mechanism. Black square regions represent locations of NO_3^- (a) and ReO_4^- (b). Packing modes of $[Ag(bipy)]^+$ chains of (c) SBN and (d) SBR in the 3D space.[23]

Another effective Ag(I) coordination polymer, $[Ag(bipy)^+(CH_3CO_2)^-\cdot 6H_2O]$ (SBA) was also recently developed by our group.[20] Most Ag-bipyridine structures have the guest anions sandwiched between layers of π-stacked polymeric chains. The Ag(1) coordinated by the nitrogens of two 4,4′-bipyridine units and one oxygen from

two separate $CH_3CO_2^-$ units define a distorted square planar geometry (Figure 1.15a). Our group reported that SBA releases its environmentally benign acetate anions upon perchlorate, permanganate, perrhenate, nitrate and chromate uptake to 99.9%, 98.5%, 91.5%, 64.4%, and 46.4% respectively, with near record high loading capacities of 310, 351, 705, 125 and 160 g/mg, respectively.

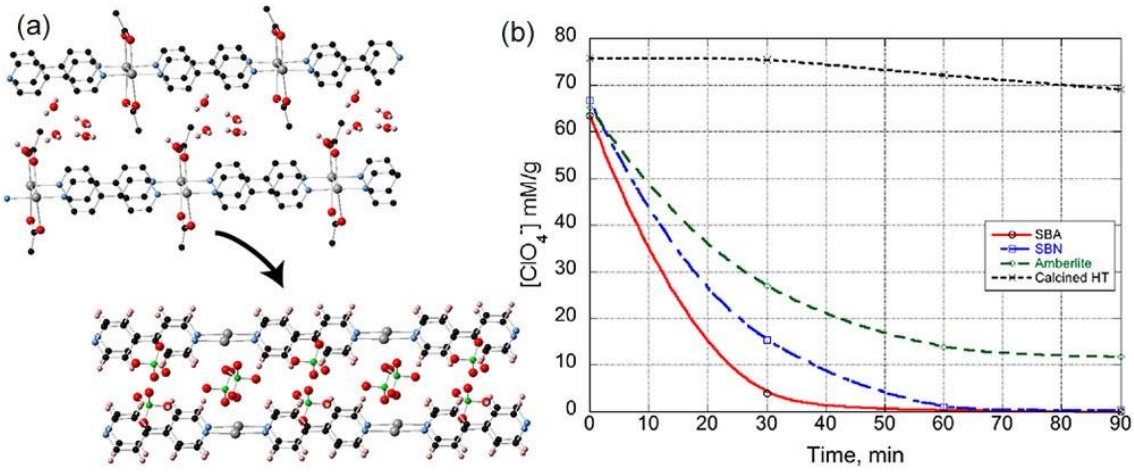

Figure 1.15: (a) Crystallographic *a* projection of SBA (top) and SBR (bottom). (b) SBA compared with SBN, Amberlite IRA-400 exchange resin, and hydrotalcite shows the decrease of perchlorate in mM ClO_4^- per gram of material.[20]

The perchlorate uptake capacity is 310 mg/g and is 94% complete within 30 min, the kinetics following a second-order reaction mechanism with $k = 0.0845(1)\ M^{-1}s^{-1}$. With an outstanding exchange activity, they also conducted 1 to 30 ppm level of low perchlorate concentration typical of most underground contaminated plumes and reported with up to 98.8% mol/mol exchange completion. SBA shows superior kinetics perchlorate uptake over SBN, Amberlite IRA-400 and calcined hydrotalcite (Figure 1.15b).

They studied exchange over a range of pH levels and SBA achieved 92% uptake of perchlorate at as low pH as 4. Finally, they tested actual contaminated groundwater with a perchlorate concentration of ca. 53 ppm, as shown in Figure 1.16. From the initial test, SBA removed 92.5% perchlorate at 30 min, and up to 95.9% after 60 min.

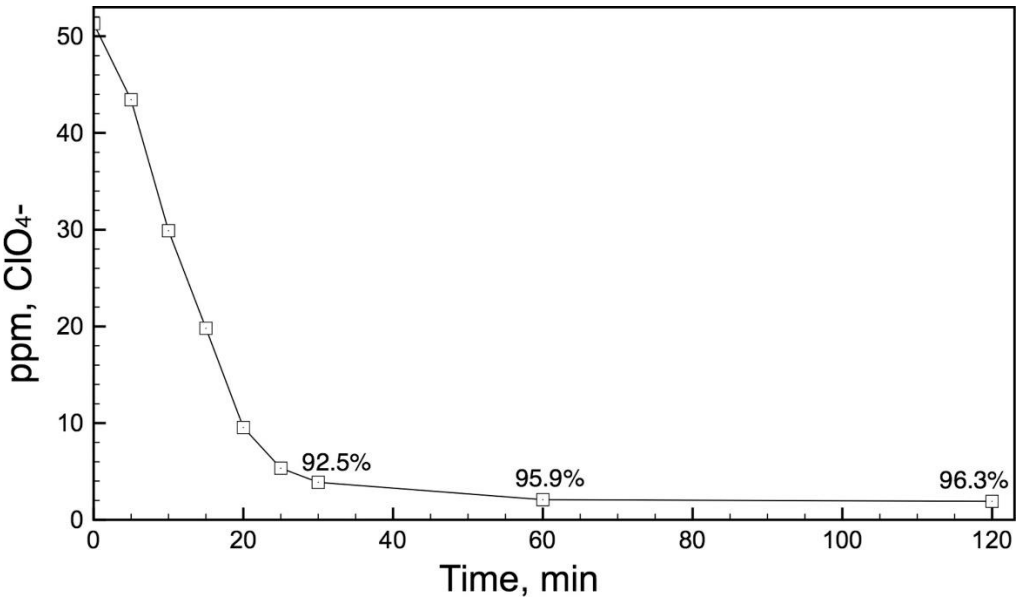

Figure 1.16: Removal of perchlorate versus time for the contaminated groundwater.[20]

The above Ag(I) CPs demonstrated remarkable results in ion exchange for various anions due to their versatile yet simple structural properties. Therefore, they may potentially show a way to design more new silver(I) CPs and selective anion exchange.

1.5 Photoluminescent Properties of Metal Coordination Polymers

1.5.1 Luminescence Concepts

Coordination polymers (CPs) and the particular subgroup metal-organic frameworks (MOFs) encompass one of the most studied and versatile classes of materials, with an increasing impact on the scientific literature.[6] The intrinsic characteristics of the CPs constituting metal ions or clusters as well as organic linkers instill these materials with equally endless functionalities. Recently, interest has been extended to the photoluminescence (PL) performance of CPs since benefiting from their tunable hybrid structure, they own abilities to transfer the well-known properties of conventional inorganic phosphors (with enormous application in solid state lighting and biomedicine)[24,25] into a new generation of smart materials with potential applications such as photodevices,[26] sensors[27] and optical storage.[28]

The presence of ligands and metal ions linked in the crystal structure allows for various possible excitation/emission scenarios which provide photoluminescence processes characterized not only by different intrinsic features (intensity, color, lifetime) but also by a distinct response to an external stimulus (presence of another molecule in the vicinity).[29]

Luminescence can be defined as the emission of light upon absorption of energy under the condition that the energy source is not heat based, which refers to incandescence. There are two main types of luminescence: fluorescence, which is a spin-allowed radiative transition from the lowest singlet excited state S_1 of the

fluorophore to its singlet ground state S_0; and phosphorescence, which refers to the spin-forbidden radiative transition from the lowest triplet state T_1 to ground state S_0 (Figure 1.17).[30,31] Luminescence in coordination polymers generally arises from the building components: conjugated organic ligands and/or metal ions or clusters, although in some cases adsorbed guest molecules may also contribute to the emission. Therefore, there are four modes of electron transfer mechanisms: (1) Linkers: the π electrons in conjugated organic compounds which absorb UV and visible region. It contributes greatly to luminescence, which can be classified as linker-based luminescence or ligand-to-ligand charge transfer (LLCT); (2) Framework metal ions: metal-to-ligand charge transfer (MLCT) or ligand-to-metal charge transfer (LMCT) nurtures from interactions among ligands (when different ligands are present) and metal ions rendering emissions strongly dependent on a particular CP; (3) Guest-centered emission and guest-sensitization; (4) Exciplex emission or excimer: π-π interactions between adjacent conjugated linkers or between a linker and a guest molecule can produce an excited complex that typically exhibits broad, featureless luminescence.

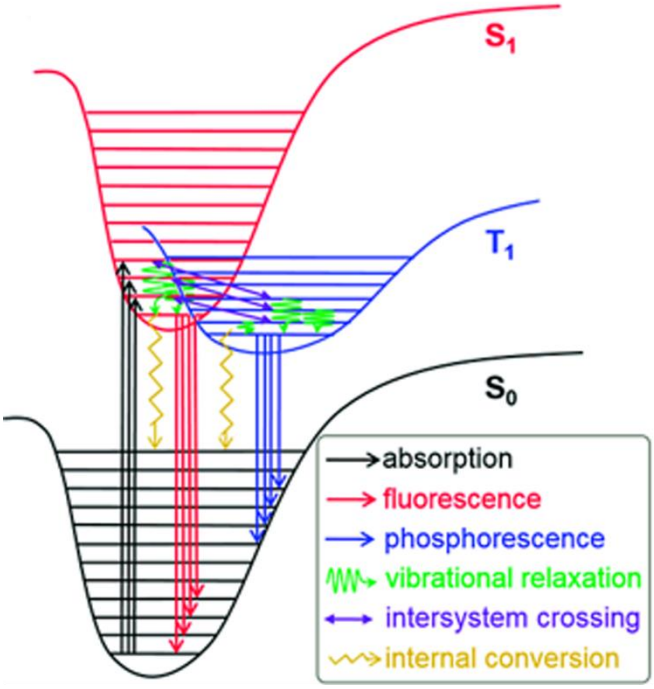

Figure 1.17: Jablonski diagram displaying schematically the electronic states of the organic linker involved in luminescence phenomena.[32]

1.5.2. Ligand-Based Charge-Transfer Luminescence

Charge-transfer luminescence is generated from an allowed transition from the charge-transfer excited state to the ground state. LMCT involves the electronic transition from an organic linker-localized orbital to a metal-centered orbital, while MLCT corresponds to the electronic transition from a metal-centered orbital to an organic linker-localized orbital (Figure 1.18). A wide variety of π-conjugated organic molecules are often used as linkers due to their rigidity, and their backbones are typically functionalized with carboxylate groups or nitrogen containing groups for metal-ligand coordination. Usually, the fluorescence emission from ligands is similar to their emission behavior in solution: the transitions are either π–π* or n–π* in nature.

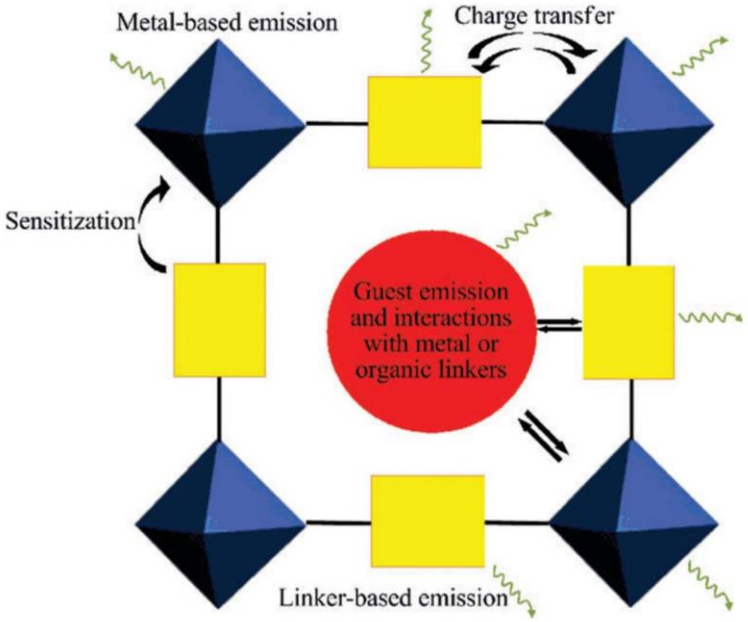

Figure 1.18: Representation of emission possibilities in porous metal organic polymers, wherein metal clusters (blue octahedra) are linked by organic linkers (yellow rectangles) with an incorporated guest (red circle).[30]

However, the fluorescence properties such as maximum emission wavelength and lifetime of organic linkers in metal CPs are often different from those of the free ligands. Because the organic linkers are stabilized within metal CPs, the nonradiative decay rate is reduced and leads to increased fluorescence intensity, lifetimes, and quantum efficiencies. In the solid state, the interactions make the molecules close together, which enable charge transfer among the organic ligands/linkers, resulting in a shift of spectra and broadening of the emission. Besides, the size and nature of metal ions, the orientation, arrangement of linkers, and the coordination environment within metal CPs can affect the fluorescence properties of the organic linkers because these factors will induce their different intramolecular or intermolecular interactions among the linkers. Therefore, controlling these interactions is critical to tuning the

luminescence properties of metal CPs for a particular application. In the particular case of the present work, the charge transfer or ligand-based luminescence is frequently observed in d^{10} metal-based coordination polymers.

1.5.3. Transition-Metal Based Luminescent Coordination Polymers

Luminescence from metal coordination polymers containing transition-metal ions in the framework is typically centered on the linker rather than on the metal but the material can also participate LMCT or MLCT between the metal and linker. Depending on the metal's electronic configuration and relative metal and linker orbital energies, the metal ion can have varying degrees of influence on the emission.

1.5.3.1. Cadmium(II) and Zinc(II) Luminescent Coordination Polymers

Metal CPs with transition-metal ions without unpaired electrons, especially those having d^{10} configurations, can yield linker-based highly emissive materials. The most commonly reported structures are for Cd(II) and Zn(II), which have filled, core-like d-orbitals and thus no d–d transitions are possible. The cubic IRMOF series offers an instructive example.[33] Crystals of the prototypical IRMOF-1, Zn_4O(1,4-benzene dicarboxylate)$_3$ consisting of basic zinc acetate units linked by benzene are reported to emit at 525 nm, which is the result of LMCT.[34] *Ab initio* studies of the IRMOF-1 electronic structure indicate that the highest occupied valence orbitals are dominated by p-orbitals of the aromatic carbon atoms, with a small contribution from the carboxylate structure.[35] IRMOF-1 featuring linkers with a greater degree of π-conjugation, including IRMOF-11 (Zn_4O(4,5,9,10-tetrahydropyrene 2,7-

dicarboxylate)$_3$), IRMOF-13 (Zn_4O(2,7-pyrene dicarboxylate)$_3$) and Zn_4O(4,4'-stilbenedicarboxylate)$_3$), which all show emission spectra similar to the linker alone.[33] The increased conjugation of these linkers compared to benzene results in a decrease in the π–π^* energy gap, and therefore the pathway for energy transfer to metal-based states becomes less efficient or is removed entirely, localizing the emission on the linker, as shown in Figure 1.19.

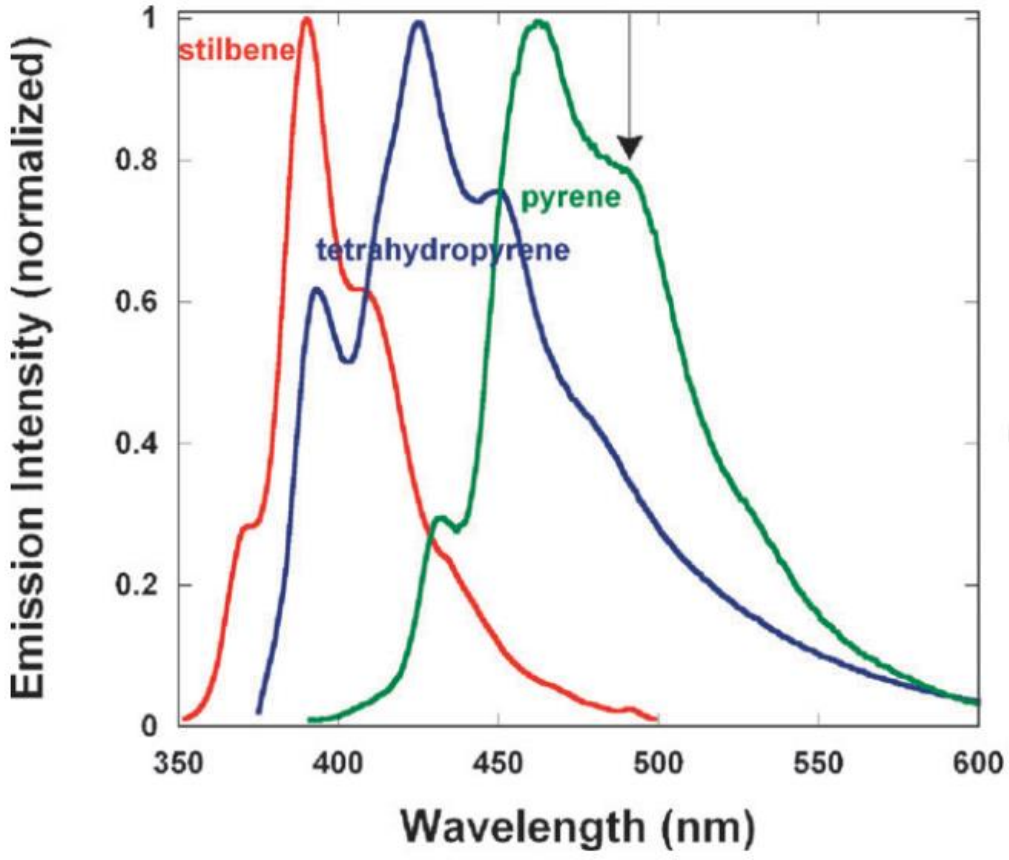

Figure 1.19: Emission spectra of three cubic MOFs consisting of Zn_4O units linked by dicarboxylates of stilbene, 4,5,9,10-tetrahydropyrene, and pyrene. The arrow indicates the position of the emission of IRMOF-1.[34]

Other MOFs containing benzene-based carboxylate linker that exhibits LMCT include a Cd framework $[Cd(Htma)(bpy)(H_2O)](H_2tp)_{0.5}\cdot 2H_2O]$ (tma - trimesatetma, bpy - 4,4'-bipyridine and tp - terephthalate). The Cd hybrid coordination polymer formed a 2D bilayer architecture through π–π interaction and their emission peaks at 360, 416, 481 and 513 nm (λ_{ex} = 311 nm) exhibited LMCT bands. Another intriguing example of how MOF luminescence can be tuned is provided by Huang *et al*., who demonstrated that emission can be toggled between linker-based and LMCT processes in the hydrated versus dehydrated crystals of $[Cd_3$(2,6-di-(4-triazolyl)pyridine$)_6](BF_4)_2(SiF_6)(OH)_2 13.5H_2O$.[36] In this case, water in the lattice prevents efficient energy transfer from the linker to metal centers, resulting in linker-centered luminescence in the UV (382 nm). Upon dehydration, the emission shifts to 438 nm as a result of LMCT.

1.5.3.2. Silver(I) Luminescent Coordination Polymers

Although Cd(II) and Zn(II) MOFs are the most commonly reported luminescent MOFs, there are a few reports of those based on Ag(I). The d electrons are in the valence orbitals of Ag(I) which enables MLCT, while in Zn(II) and Cd(II) these are core-like d-orbitals. Excitation of the 2-D layered structure Ag(4-(2-pyrimidylthiomethyl)benzoate) at λ = 370 nm produces an intense green emission with a peak maximum at 530 nm, the origin of which was assigned to LMCT and/or MLCT modified by metal-centered (ds/dp) states having Ag–Ag interactions.[37] The complex $[Ag(4,4'\text{-bipy})]_n[Ag(1,2,4\text{-benezenetricaboxylate})]_n$ exhibits an intense

fluorescent emission band with a maximum at 502 nm (λ_{ex} = 410 nm) due to MLCT.[38] In 2009, the Wang group reported a first direct white-light-emitting silver MOF, [Ag(4-cyanobenzoate)]$_n$·nH$_2$O, with tunable yellow to white luminescence by variation of excitation light.[39] The material displays a maximum emission at around 427 and 566 nm when excited at 355 and 330 nm, respectively. When irradiated at 330 nm, the emission intensity at 427 nm is decreased, but the emission intensity at approximately 513, 566, and 617 nm is enhanced, generating yellow luminescence. When adjusting the excitation light to 350 nm, the emission peaks at 427 and 566 nm are very strong, which results in direct white light to the naked eye (Figure 1.20). These emissions can be attributed to ligand-centered and MLCT coexisting in the absorption transition of the Ag(I)MOF.

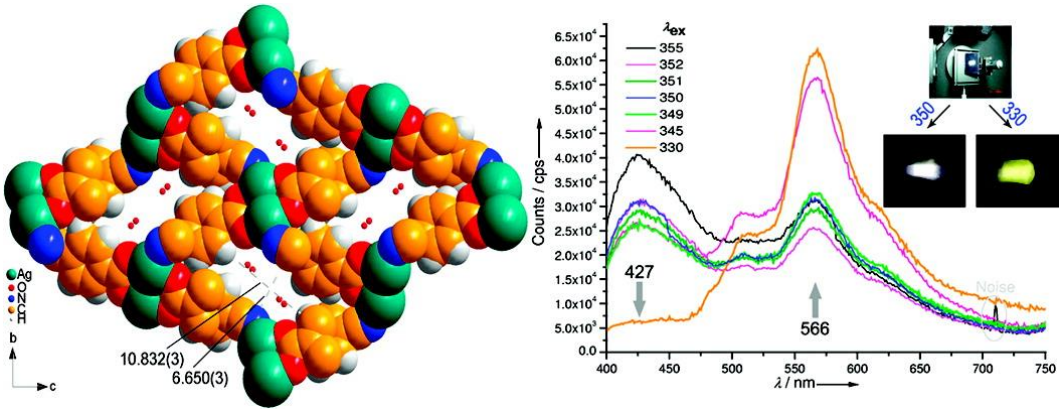

Figure 1.20: 3D packing diagram of [Ag(4-cyanobenzoate)]$_n$·nH$_2$O viewed along *a* direction (left); Solid-state PL spectra of [Ag(4-cyanobenzoate)]$_n$·nH$_2$O by variation of excitation light under the same metrical condition (right). Inset shows the PL images of a sample excited by 350 and 330 nm light, respectively.[39]

The Commission Internationale de l'Eclairage (CIE) chromaticity coordinates of the white-light emissions excited by 350- and 349-nm light are approximately (0.31,

0.33) and (0.33, 0.34), respectively, comparable to that of pure white light. Therefore, the MOF can be tuned from yellow to white by direct variation of excitation wavelength, indicating it can be potentially used as a single white phosphor for a white light-emitting device equipped with a deep UV GaN LED, which has light output at 325 and 350 nm.

The Etaiw group reported another interesting silver coordination polymer, $[Ag(C_8H_6N_2)^+][NO_3^-]$, a weakly luminescent material with potential use as a luminescent probe.[40]

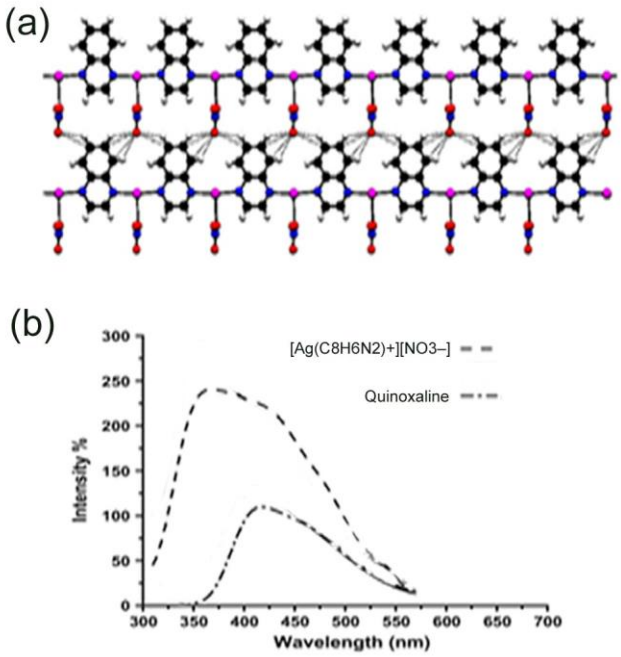

Figure 1.21: (a) 2D sheet of the packing diagram of $[Ag(C_8H_6N_2)^+][NO_3^-]$ viewed along *b* direction ; (b) Emission spectra of quinoxaline ligand and solid state $[Ag(C_8H_6N_2)^+][NO_3^-]$) ($\lambda_{ex}$ = 300 nm).[40]

Self-assembly of $[Ag(C_8H_6N_2)^+][NO_3^-]$ by hydrogen bonds, π–π stacking and short contacts grow the structure to a 3D network creating wide channels to accommodate the coordinated nitrate ions (Figure 1.21a). The material exhibits a strong emission band at 355 nm and showed a blue shift than the free ligand (Figure 1.21b). The emission spectra data corresponds to the close lying π–π* transitions and resulting ligand-based luminescence polymer.

1.6 Metal-Organic Frameworks as Electrochemical Catalysts

1.6.1 Fuel Cells and Their Electrochemistry Fundamentals

Global warming caused by excess greenhouse gas emission is an international concern. In need of reducing the global temperature incline below 1.5 °C per century to comply with the Paris agreement,[41] it is essential to develop clean and sustainable energy technology that is universally accessible. Fuel cells powered by hydrogen from renewable sources are the ideal solution for environmentally friendly energy devices. The most common type of fuel cells, both in research and in commercial use, is polymer electrolyte membrane fuel cells (PEMFCs). Unlike most other types of fuel cells, PEMFC uses a quasi-solid electrolyte, which is based on a polymer backbone with side-chains possessing acid-based groups. The numerous advantages of this family of electrolytes make the PEM fuel cell particularly attractive for smaller-scale terrestrial applications such as transportation, home-based distributed power, and portable power applications. The distinguishing features of PEMFC include relatively low-temperature (under 80 °C) operation, high power density, a

compact system, and ease in handling liquid fuel.[42] A PEM fuel cell consists of an electrolyte sandwiched between two electrodes. At the surfaces of the two electrodes, two electrochemical reactions take place. At the anode, over which hydrogen gas passes, occurs the hydrogen oxidation reaction (HOR). At the cathode, over which oxygen or air passes, occurs the oxygen reduction reaction (ORR). The two electrode reactions are shown in Figure 1.22.

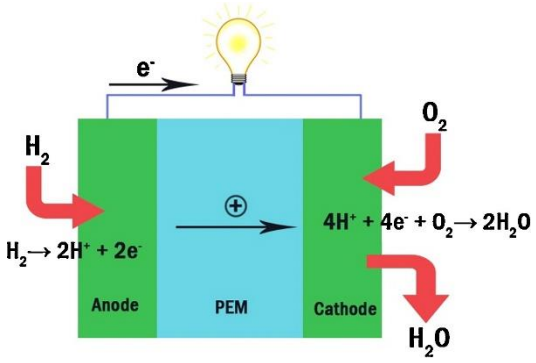

Figure 1.22: Operating principle of an H_2 fuel cell (PEM = polymer electrolyte membrane).[43]

The ORR ideally takes place via the four-electron pathway to ensure the fuel cell generates the maximum power output and water as the only exhaust.[44]The other pathway involves the production of hydrogen peroxide through a two-electron pathway. The presence of hydrogen peroxide not only leads to low energy conversion efficiency but also produces reactive peroxide radical species. Therefore, the ORR is well recognized as sluggish. The slow kinetics constitutes one of the major voltage losses due to a high reduction overpotential in the performance of a PEMFC and is a major limitation of the fuel cell performance. Thus, the investigation of ORR remains a major focus of PEMFC research.

Considering the PEMFCs operate at low temperatures (80 °C), the reactions must be sped up with the help of efficient catalysts to achieve the desired high-power density. Traditionally, platinum (Pt) and Pt-based materials are widely used as active electrocatalysts for ORR.[45] In long-term fuel cell operation, the stability and durability of the catalyst is always problematic. Carbon oxidation and Pt sintering or agglomeration can result in loss of electroactive surface on the catalysts, degrading fuel cell performance. These problems are more pronounced when the PEMFC operates at high temperatures. It is highly desirable to find efficient and inexpensive alternatives to Pt-based catalysts for fuel cell reactions, especially for the ORR at the cathode which requires much more Pt because of the slower reaction speed.[46] The imminent challenge is to develop new catalysts that can have long-term stability under fuel cell operating conditions and survive fault-tolerant condition and are amenable to high-volume production with high yields and exceptional quality.[47]

1.6.2. MOFs as Promising Materials in Fuel Cells

Recently, there has been a growing interest in developing MOF-based materials for electrochemical energy storage. MOFs, which have been demonstrated to be indispensable for clean energy storage and conversion, have also shown great potential in fuel cells. Electrochemical energy storage in pristine MOFs depends mainly on the design of particle size, active surface area, pore size distribution, crystallinity and availability of functional groups for use as electrocatalysts in electrodes. One of the significant advances of non-precious metal catalysts is the development of metal–nitrogen–carbon (M–N–C) catalysts derived from transition

metal macrocycle precursors. Early research found that cobalt phthalocyanine was active for ORR catalysis by Jasinski in 1964.[48] Catalysts were first obtained by adsorbing Fe-N_4 or Co-N_4 macrocycles on a carbon support and pyrolyzing the resulting material in an inert atmosphere.[49] Activation in an inert atmosphere of the similar transition metal-polymer composite through pyrolysis further improved the catalytic activity. Later, researchers substituted mixtures of much cheaper transition metal salts and nitrogen precursors for the macrocycles and found that they also obtained improved ORR activity and enhanced stability.[50] It has been suggested that the micropores in the catalyst are required for the catalytic activity. From these requirements, it is evident that MOFs are the ideal candidate for preparing M–N–C catalysts. MOF precursors with rich M–N–C sites and tunable microstructure can be achieved from a precise molecular design.

The first example of a MOF derived ORR catalyst was found by activating cobalt imidazolate frameworks (active Co-IM) at high temperature, and it is since this research that more attention has been paid to this field.[51] The purple crystals of cobalt imidazolate frameworks (Co-IM) were developed by using 3,5-imidazolate, and Co $(NO_3)_2 \cdot 6H_2O$ in N,N-dimethylacetamide (DMA) under solvothermal conditions. Single-crystal X-ray studies revealed that every cobalt atom binds four nitrogen atoms from four 3,5-imidazolate ligands, and each 3,5-imidazolate ligand connects with two cobalt atoms to form a three-dimensional (3D) porous structure with a Co–Co distance of approximately 8.1Å along the [100] direction (Figure 1.23). A Brunauer–Emmett–Teller (BET) specific surface area (SSA) showed a porosity of

305 m^2g^{-1}. The Co-IM was heat-treated to produce an ORR catalyst at 600, 700 and 750 °C, respectively.

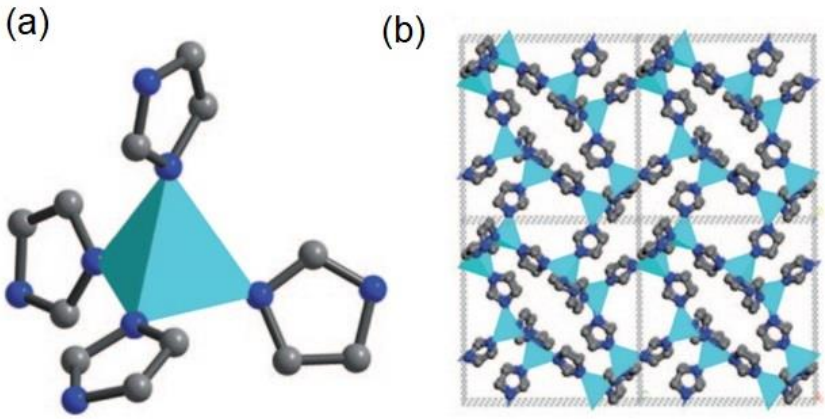

Figure 1.23: a) Local Co–N_4 coordination moiety; b) structure packing of Co-IM along the [100] direction (color scheme: turquoise=Co, blue=N, gray=C).[51]

Upon thermal activation, the material underwent the structural transformation and no longer maintains long-range lattice order. The imidazolate groups gradually convert to carbonaceous form whereas a fraction of the nitrogen is retained as pyridinic or pyrrolic-like moieties. Such moieties are known to form catalytic sites by coordinating the transition metal by nitrogen;[52] an example is Co–N_4, shown by the proposed structure in Figure 1.24.

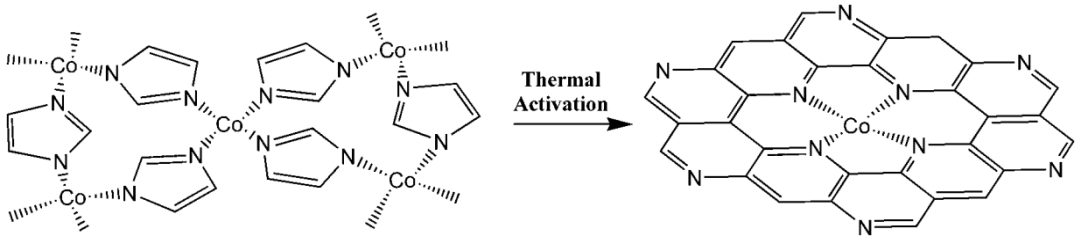

Figure 1.24: Proposed structural conversion from Co-IM to the active catalytic site.[51]

The active Co-IM displays a BET SSA of 265 m^2g^{-1} and a significant fraction of the micropore volume. Increasing the activation temperature to 900 °C led to a reduction in SSA for both micropore and mesopore regions, exemplifying the direct correlation between the surface area and the catalyst activity. The sample that achieved best ORR catalyst activity was pyrolyzed at a temperature of 750 °C, resulting in an onset potential of 0.83 V and half-wave potential of 0.68 V in acidic medium (Figure 1.25). The number of transferred electrons, *n*, for ORR ranged from 3.2 to 3.5.

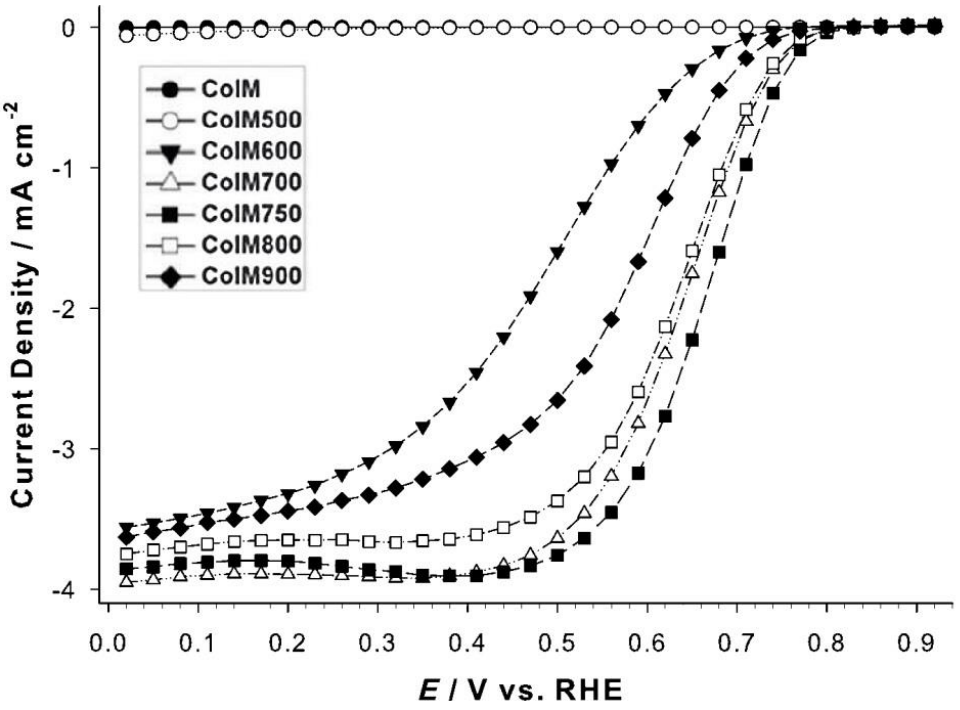

Figure 1.25: Faradaic current density as a function of the potential with reference to the reversible hydrogen electrode (RHE) for Co-IM at different temperatures.[51]

When iron replaced the cobalt center resulting in iron imidazole framework (Fe-IM), the catalytic activity is better than the Co-IM catalysts.[53] In Fe-IM, Fe^{2+} ions were coordinated tetrahedrally or octahedrally through imidazolate ions to yield a

continuous 3D framework. In order to study conductivity, pristine Fe-IM crystals were pyrolyzed at temperatures of 700, 800 and 900 °C, respectively. From three different pyrolysis conditions, Fe-IM pyrolyzed at 800 °C (FeIM800) demonstrated a better ORR catalytic activity, with an onset potential of 0.859 V and the better number of electrons transferred (3.59 to 3.78). The electrochemical performance was further improved by mixing the precursors with a Zn^{2+} zeolitic imidazolate framework, ZIF-8. The FeIM/ZIF-8 mixture had the best performance of all, with the highest onset potential 0.915 V, half-wave potential of 7.55 V and close to four electrons transfer (3.83 to 3.93). The iron content in the FeIM/ZIF-8 mixture was 5.29 weight %.

1.7. Conclusion and Outlook

Luminescent coordination polymers (CPs) are certainly very promising multifunctional materials for chemical sensors, LED devices, and biomedicine. As compared to the research on functional CPs for gas storage, separation, and heterogeneous catalysis, the research on luminescent CPs is still at the early stage. While luminescent CPs are still at an early stage of development, it is evident from the examples cited above that these materials represent a promising avenue of research. CPs have thus far been investigated for luminescent properties owing to their structural diversity and modulability, and tunability of emission behavior by structure type. Due to this precedence, the following chapter will describe the methodology of new materials that have been developed thorough characterization methods to assess the luminescent behavior.

With a remarkable efficiency, high-energy density PEMFC fuel cells are considered a green energy technology that meets the energy requirements to power future electric vehicles and other energy-consuming devices. Yet, the high cost and poor durability of noble metal catalysts used in fuels cells limit their potential application within the consumer marketplace. Advanced electrode catalysts made from a MOF template/precursor, with high activity and sufficient stability, are drawing considerable interest as alternatives to noble metals.[54] With rich active sites, highly accessible surface area, and ordered porous channels, these kinds of MOF-derived metal-free electrocatalysts demonstrate excellent ORR activity and long-term durability in alkaline media. The presence of transition metal/metal oxide nanocrystals is essential to developing higher graphitized nanocarbon structures, yielding more conductive and even more active and durable catalysts. Additionally, the incorporation of transition metals within the doped-carbon matrix may aid in promoting the metal species to participate toward M-N_x-C sites, resulting in improved intrinsic activity. In-depth theoretical and experimental studies are needed to delicately design MOF-derived electrocatalysts with desirable pore sizes and dimensions for specific applications. It is also essential to clarify the role of the MOF skeleton in the overall catalytic activity. The future trend is leaning toward improving the utilization of Pt group metals or replacing them completely with less expensive metals such as Co, Fe, or Ni, for cost-effectiveness. Therefore, the following chapter (5) will discuss the ration design and synthesis during precursor development of MOF-derived electrocatalysts for ORR activity.

1.8. References

(1) Furukawa, H.; Ko, N.; Go, Y. B.; Aratani, N.; Choi, S. B.; Choi, E.; Yazaydin, A. Ö.; Snurr, R. Q.; O'Keeffe, M.; Kim, J.; et al. Ultrahigh Porosity in Metal-Organic Frameworks. *Science* **2010**, *329* (5990), 424–428. https://doi.org/10.1126/science.1192160.

(2) Kitagawa, S.; Matsuda, R. Chemistry of Coordination Space of Porous Coordination Polymers. *Coord. Chem. Rev.* **2007**, *251* (21), 2490–2509. https://doi.org/10.1016/j.ccr.2007.07.009.

(3) Chen, B.; Xiang, S.; Qian, G. Metal−Organic Frameworks with Functional Pores for Recognition of Small Molecules. *Acc. Chem. Res.* **2010**, *43* (8), 1115–1124. https://doi.org/10.1021/ar100023y.

(4) Wang, Z.; M. Cohen, S. Postsynthetic Modification of Metal–Organic Frameworks. *Chem. Soc. Rev.* **2009**, *38* (5), 1315–1329. https://doi.org/10.1039/B802258P.

(5) Ma, Z.; Moulton, B. Recent Advances of Discrete Coordination Complexes and Coordination Polymers in Drug Delivery. *Coord. Chem. Rev.* **2011**, *255* (15), 1623–1641. https://doi.org/10.1016/j.ccr.2011.01.031.

(6) Janiak, C.; K. Vieth, J. MOFs, MILs and More: Concepts, Properties and Applications for Porous Coordination Networks (PCNs). *New J. Chem.* **2010**, *34* (11), 2366–2388. https://doi.org/10.1039/C0NJ00275E.

(7) Batten, S. R.; Neville, S. M.; Turner, D. R. *Coordination Polymers: Design, Analysis and Application*; Royal Society of Chemistry, 2008.

(8) Khlobystov, A. N.; Blake, A. J.; Champness, N. R.; Lemenovskii, D. A.; Majouga, A. G.; Zyk, N. V.; Schröder, M. Supramolecular Design of One-Dimensional Coordination Polymers Based on Silver(I) Complexes of Aromatic Nitrogen-Donor Ligands. *Coord. Chem. Rev.* **2001**, *222* (1), 155–192. https://doi.org/10.1016/S0010-8545(01)00370-8.

(9) Zheng, S.-L.; Tong, M.-L.; Chen, X.-M. Silver(I)–Hexamethylenetetramine Molecular Architectures: From Self-Assembly to Designed Assembly. *Coord. Chem. Rev.* **2003**, *246* (1–2), 185–202. https://doi.org/10.1016/S0010-8545(03)00116-4.

(10) Su, C.-Y.; Chen, C.-L.; Zhang, J.-Y.; Kang, B.-S. Silver(I) Coordination Polymers. In *Design and Construction of Coordination Polymers*; Wiley-Blackwell, 2009; pp 111–144. https://doi.org/10.1002/9780470467336.ch5.

(11) Fei, H.; Paw U, L.; Rogow, D. L.; Bresler, M. R.; Abdollahian, Y. A.; Oliver, S. R. J. Synthesis, Characterization, and Catalytic Application of a Cationic Metal−Organic Framework: Ag2(4,4′-Bipy)2(O3SCH2CH2SO3). *Chem. Mater.* **2010**, *22* (6), 2027–2032. https://doi.org/10.1021/cm9032308.

(12) Huang, Z.; Du, M.; Song, H.-B.; Bu, X.-H. Effect of Anions on the Framework Formation of Novel AgI Coordination Polymers with Angular Bridging Ligands. *Cryst. Growth Des.* **2004**, *4* (1), 71–78. https://doi.org/10.1021/cg0341095.

(13) Bu, X.-H.; Biradha, K.; Yamaguchi, T.; Nishimura, M.; Ito, T.; Tanaka, K.; Shionoya, M. A Novel Polymeric AgI Complex Consisting of Two Three-

Dimensional Networks Which Are Enantiometric and Interpenetrating. *Chem. Commun.* **2000**, *0* (19), 1953–1954. https://doi.org/10.1039/B003183F.

(14) Hong, M.-C.; Chen, L. Design and Construction of Coordination Polymers. In *Design and Construction of Coordination Polymers*; John Wiley & Sons, Inc.: New Jersey, 2009; pp 111–144.

(15) Batten, S. R.; Neville, S. M.; Turner, D. R. Porous Coordination Polymers. In *Coordination Polymers*; Royal Society of Chemistry, 2009; pp 313–344. https://doi.org/10.1039/9781847558862-00313.

(16) May, L. J.; Shimizu, G. K. H. Highly Selective Intercalation of Primary Amines in a Continuous Layer Ag Coordination Network. *Chem. Mater.* **2005**, *17* (2), 217–220. https://doi.org/10.1021/cm048471y.

(17) Fei, H.; Bresler, M. R.; Oliver, S. R. J. A New Paradigm for Anion Trapping in High Capacity and Selectivity: Crystal-to-Crystal Transformation of Cationic Materials. *J. Am. Chem. Soc.* **2011**, *133* (29), 11110–11113. https://doi.org/10.1021/ja204577p.

(18) Colinas, I. R.; Silva, R. C.; Oliver, S. R. J. Reversible, Selective Trapping of Perchlorate from Water in Record Capacity by a Cationic Metal–Organic Framework. *Environ. Sci. Technol.* **2016**, *50* (4), 1949–1954. https://doi.org/10.1021/acs.est.5b03455.

(19) R. Colinas, I.; K. Inglis, K.; Blanc, F.; J. Oliver, S. R. Anion Exchange Dynamics in the Capture of Perchlorate by a Cationic Ag-Based MOF. *Dalton Trans.* **2017**, *46* (16), 5320–5325. https://doi.org/10.1039/C7DT00475C.

(20) Citrak, S. C.; Popple, D.; Delgado-Cunningham, K.; Tabler, K.; Bdeir, K.; Oliver, A. G.; Kvam, P. B.; Oliver, S. R. J. Extremely Rapid Uptake of Perchlorate with Release of an Environmentally Benign Anion: Silver Bipyridine Acetate. *Cryst. Growth Des.* **2018**, *18* (3), 1891–1895. https://doi.org/10.1021/acs.cgd.7b01797.

(21) Yaghi, O. M.; Li, H. T-Shaped Molecular Building Units in the Porous Structure of Ag(4,4‘-Bpy)·NO3. *J. Am. Chem. Soc.* **1996**, *118* (1), 295–296. https://doi.org/10.1021/ja953438l.

(22) Blake, A. J.; Champness, N. R.; Hubberstey, P.; Li, W.-S.; Withersby, M. A.; Schröder, M. Inorganic Crystal Engineering Using Self-Assembly of Tailored Building-Blocks. *Coord. Chem. Rev.* **1999**, *183* (1), 117–138. https://doi.org/10.1016/S0010-8545(98)00173-8.

(23) Zhu, L.; Xiao, C.; Dai, X.; Li, J.; Gui, D.; Sheng, D.; Chen, L.; Zhou, R.; Chai, Z.; Albrecht-Schmitt, T. E.; et al. Exceptional Perrhenate/Pertechnetate Uptake and Subsequent Immobilization by a Low-Dimensional Cationic Coordination Polymer: Overcoming the Hofmeister Bias Selectivity. *Environ. Sci. Technol. Lett.* **2017**, *4* (7), 316–322. https://doi.org/10.1021/acs.estlett.7b00165.

(24) Lustig, W. P.; Mukherjee, S.; Rudd, N. D.; Desai, A. V.; Li, J.; Ghosh, S. K. Metal–Organic Frameworks: Functional Luminescent and Photonic Materials for Sensing Applications. *Chem. Soc. Rev.* **2017**, *46* (11), 3242–3285. https://doi.org/10.1039/C6CS00930A.

(25) Valeur, B.; Berberan-Santos, M. N. *Molecular Fluorescence: Principles and Applications*; John Wiley & Sons, 2012.

(26) Li, Y.; Hu, Y.; Zhao, Y.; Shi, G.; Deng, L.; Hou, Y.; Qu, L. An Electrochemical Avenue to Green-Luminescent Graphene Quantum Dots as Potential Electron-Acceptors for Photovoltaics. *Adv. Mater.* **2011**, *23* (6), 776–780. https://doi.org/10.1002/adma.201003819.

(27) Wang, X.; Wolfbeis, O. S.; Meier, R. J. Luminescent Probes and Sensors for Temperature. *Chem. Soc. Rev.* **2013**, *42* (19), 7834–7869. https://doi.org/10.1039/C3CS60102A.

(28) Hong, E. Y.-H.; Poon, C.-T.; Yam, V. W.-W. A Phosphole Oxide-Containing Organogold(III) Complex for Solution-Processable Resistive Memory Devices with Ternary Memory Performances. *J. Am. Chem. Soc.* **2016**, *138* (20), 6368–6371. https://doi.org/10.1021/jacs.6b02629.

(29) Paz, F. A. A.; Klinowski, J.; F. Vilela, S. M.; C. Tomé, J. P.; S. Cavaleiro, J. A.; Rocha, J. Ligand Design for Functional Metal–Organic Frameworks. *Chem. Soc. Rev.* **2012**, *41* (3), 1088–1110. https://doi.org/10.1039/C1CS15055C.

(30) Allendorf, M. D.; Bauer, C. A.; Bhakta, R. K.; Houk, R. J. T. Luminescent Metal–Organic Frameworks. *Chem. Soc. Rev.* **2009**, *38* (5), 1330–1352. https://doi.org/10.1039/B802352M.

(31) Cui, Y.; Yue, Y.; Qian, G.; Chen, B. Luminescent Functional Metal–Organic Frameworks. *Chem. Rev.* **2012**, *112* (2), 1126–1162. https://doi.org/10.1021/cr200101d.

(32) Sebastian, E. S.; Rodríguez-Diéguez, A.; Seco, J. M.; Cepeda, J. Coordination Polymers with Intriguing Photoluminescence Behavior: The Promising Avenue for Greatest Long-Lasting Phosphors. *Eur. J. Inorg. Chem.* **2018**, *2018* (20–21), 2155–2174. https://doi.org/10.1002/ejic.201800124.

(33) Eddaoudi, M. Systematic Design of Pore Size and Functionality in Isoreticular MOFs and Their Application in Methane Storage. *Science* **2002**, *295* (5554), 469–472. https://doi.org/10.1126/science.1067208.

(34) Bordiga, S.; Lamberti, C.; Ricchiardi, G.; Regli, L.; Bonino, F.; Damin, A.; Lillerud, K.-P.; Bjorgen, M.; Zecchina, A. Electronic and Vibrational Properties of a MOF-5 Metal–Organic Framework: ZnO Quantum Dot Behaviour. *Chem. Commun.* **2004**, *0* (20), 2300–2301. https://doi.org/10.1039/B407246D.

(35) Civalleri, B.; Napoli, F.; Noël, Y.; Roetti, C.; Dovesi, R. Ab-Initio Prediction of Materials Properties with CRYSTAL: MOF-5 as a Case Study. *CrystEngComm* **2006**, *8* (5), 364–371. https://doi.org/10.1039/B603150C.

(36) Huang, Y.-Q.; Ding, B.; Song, H.-B.; Zhao, B.; Ren, P.; Cheng, P.; Wang, H.-G.; Liao, D.-Z.; Yan, S.-P. A Novel 3D Porous Metal–Organic Framework Based on Trinuclear Cadmium Clusters as a Promising Luminescent Material

Exhibiting Tunable Emissions between UV and Visible Wavelengths. *Chem. Commun.* **2006**, *0* (47), 4906–4908. https://doi.org/10.1039/B610185B.

(37) Han, L.; Yuan, D.; Wu, B.; Liu, C.; Hong, M. Syntheses, Structures and Properties of Three Novel Coordination Polymers with a Flexible Asymmetrical Bridging Ligand. *Inorganica Chim. Acta* **2006**, *359* (7), 2232–2240. https://doi.org/10.1016/j.ica.2005.12.077.

(38) Zhang, S.; Wang, Z.; Zhang, H.; Cao, Y.; Sun, Y.; Chen, Y.; Huang, C.; Yu, X. Self-Assembly of Two Fluorescent Supramolecular Frameworks Constructed from Unsymmetrical Benzene Tricarboxylate and Bipyridine. *Inorganica Chim. Acta* **2007**, *360* (8), 2704–2710. https://doi.org/10.1016/j.ica.2007.01.023.

(39) Wang, M.-S.; Guo, S.-P.; Li, Y.; Cai, L.-Z.; Zou, J.-P.; Xu, G.; Zhou, W.-W.; Zheng, F.-K.; Guo, G.-C. A Direct White-Light-Emitting Metal-Organic Framework with Tunable Yellow-to-White Photoluminescence by Variation of Excitation Light. *J. Am. Chem. Soc.* **2009**, *131* (38), 13572–13573. https://doi.org/10.1021/ja903947b.

(40) Etaiw, S. E. H.; El-bendary, M. M.; Fouda, A. E.-A. S.; Maher, M. Synthesis and Structure Characterizations of Coordination Polymers Based on Silver(I) and Nitrogen Donors. *J. Inorg. Organomet. Polym. Mater.* **2014**, *25* (4), 702–711. https://doi.org/10.1007/s10904-014-0148-3.

(41) United Nations Framework Convention on Climate Change, Adoption of the Paris Agreement, Proposal by the President. 2015.

(42) Zhang, J. *PEM Fuel Cell Electrocatalysts and Catalyst Layers: Fundamentals and Applications*; Springer Science & Business Media, 2008.

(43) Ren, Y.; Chia, G. H.; Gao, Z. Metal–Organic Frameworks in Fuel Cell Technologies. *Nano Today* **2013**, *8* (6), 577–597. https://doi.org/10.1016/j.nantod.2013.11.004.

(44) Shimizu, K.; Sepunaru, L.; G. Compton, R. Innovative Catalyst Design for the Oxygen Reduction Reaction for Fuel Cells. *Chem. Sci.* **2016**, *7* (5), 3364–3369. https://doi.org/10.1039/C6SC00139D.

(45) Neyerlin, K. C.; Gu, W.; Jorne, J.; Gasteiger, H. A. Determination of Catalyst Unique Parameters for the Oxygen Reduction Reaction in a PEMFC. *J. Electrochem. Soc.* **2006**, *153* (10), A1955. https://doi.org/10.1149/1.2266294.

(46) Wu, G.; More, K. L.; Johnston, C. M.; Zelenay, P. High-Performance Electrocatalysts for Oxygen Reduction Derived from Polyaniline, Iron, and Cobalt. *Science* **2011**, *332* (6028), 443–447. https://doi.org/10.1126/science.1200832.

(47) Debe, M. K. Electrocatalyst Approaches and Challenges for Automotive Fuel Cells. *Nature* **2012**, *486* (7401), 43–51. https://doi.org/10.1038/nature11115.

(48) Jasinski, R. A New Fuel Cell Cathode Catalyst. *Nature* **1964**, *201* (4925), 1212–1213. https://doi.org/10.1038/2011212a0.

(49) Dodelet, J.-P. Oxygen Reduction in PEM Fuel Cell Conditions: Heat-Treated Non-Precious Metal-N4 Macrocycles and Beyond. In *N4-Macrocyclic Metal*

Complexes; Springer, New York, NY, 2006; pp 83–147. https://doi.org/10.1007/978-0-387-28430-9_3.

(50) Lefèvre, M.; Proietti, E.; Jaouen, F.; Dodelet, J.-P. Iron-Based Catalysts with Improved Oxygen Reduction Activity in Polymer Electrolyte Fuel Cells. *Science* **2009**, *324* (5923), 71–74. https://doi.org/10.1126/science.1170051.

(51) Ma, S.; Goenaga, G. A.; Call, A. V.; Liu, D.-J. Cobalt Imidazolate Framework as Precursor for Oxygen Reduction Reaction Electrocatalysts. *Chem. – Eur. J.* **2011**, *17* (7), 2063–2067. https://doi.org/10.1002/chem.201003080.

(52) Cross-Laboratory Experimental Study of Non-Noble-Metal Electrocatalysts for the Oxygen Reduction Reaction - ACS Applied Materials & Interfaces (ACS Publications) https://pubs.acs.org/doi/full/10.1021/am900219g (accessed Jul 24, 2018).

(53) Zhao, D.; Shui, J.-L.; Chen, C.; Chen, X.; M. Reprogle, B.; Wang, D.; Liu, D.-J. Iron Imidazolate Framework as Precursor for Electrocatalysts in Polymer Electrolyte Membrane Fuel Cells. *Chem. Sci.* **2012**, *3* (11), 3200–3205. https://doi.org/10.1039/C2SC20657A.

(54) Song, Z.; Cheng, N.; Lushington, A.; Sun, X.; Song, Z.; Cheng, N.; Lushington, A.; Sun, X. Recent Progress on MOF-Derived Nanomaterials as Advanced Electrocatalysts in Fuel Cells. *Catalysts* **2016**, *6* (8), 116. https://doi.org/10.3390/catal6080116.

Chapter (2)

Aqueous Anion Exchange by Cationic Silver Pyrazine Coordination Polymers

Abstract

We report the first example of linker modification for an N-donor Ag-based cationic material while maintaining and in some cases increasing the anion exchange capacity. Cationic silver(I) pyrazine nitrate selectively traps harmful oxo-anions from water such as permanganate, perrhenate and a variety of α,ω-alkanedicarboxylates. The host-guest interaction between the cationic layers of □-stacked silver pyrazine polymers and the incoming/outgoing interlamellar anions allows for the exchange. We chose these anions as initial examples of exchange for potential water purification. The exchange capacity over 24 h reached 435 and 818 mg/g for permanganate and perrhenate, respectively, a record for crystalline metal-organic materials and over five times the exchange capacity compared to commercial resin. The material also undergoes organic exchange as an analog for pharmaceutical waste, some of which have a carboxylate functionality at the neutral pH range typical of natural water sources. Both the as-synthesized and exchanged materials are characterized by a variety of analytical techniques.

2.1. Introduction

2.1.1. Silver Pyrazine Coordination Polymers

Open-framework metal–organic polymers, derived from the combination of selected transition metal and multi-dentate bridging ligands, have attracted much attention owing to their various potential applications including electrocatalysis,[1] magnetism,[2] luminescence,[3] gas storage,[4] ion exchange[5] and heterogeneous catalysis.[6,7] Coordination polymers (CPs) based on Ag(I) cations are attracting a great deal of attention, in part because they are structurally versatile.[8,9] The coordination sphere of the d^{10} metal, Ag(I), is very flexible and can adopt coordination numbers two to six and various geometries from linear to trigonal, tetrahedral, trigonal pyramidal and octahedral.[10] The structural flexibility of these complexes is essential for the investigation of non-covalent host-guest interactions, as weak intermolecular forces significantly affect the geometry and topology of the Ag(I) coordination polymers in the solid state.[11]

There has been much recent interest in the study of linear 1-D silver coordination polymers involving bridging N-heterocyclic ligands.[12,13] The simplest such ligand is pyrazine, which has two nitrogen donors in its six-ring. Using a 1:1 ratio with silver nitrate, silver(I) pyrazine structures can be synthesized. [14,15] Simple mononuclear complexes, $[Ag(C_4H_4N_2)]^+$ and $[Ag(C_4H_4N_2)_2]^+$, were first reported in the 1960s[16] and have since been the subject of various studies including measurements of stability constants,[16] infrared spectroscopy[17] and mass spectroscopy.[18] The structure was clearly shown to be a linear shape when its X-ray

crystal structure was reported in 1966.[19] Due to the lability of the Ag-donor atom bond,[20] the process of coordination polymer formation is highly reversible. As a result, the Ag(I) coordination polymers can readily be crystallized with various counter-anions, allowing investigation by single crystal X-ray diffraction. Our group is thus interested in developing new anion exchange chemistry using silver pyrazine CPs.

2.1.2. Anion Exchange Interest and Motivation

Many of the priority pollutants in wastewater listed by the U.S. Environmental Protection Agency (EPA) are in their oxo-anionic form, for example, pertechnetate (TcO_4^-), chromate (CrO_4^{2-}) and arsenate (AsO_4^{3-}).[21] These toxic, harmful anions are problematic in the vitrification of low activity radioactive waste, weakening the integrity of the waste glass by forming spinels.[22] Another class of water-borne toxic anion pollutants are organic, generated through both industrial and personal use. EPA classifies many of these pollutants as pharmaceutical and personal care products (PPCPs).[23] Many pharmaceuticals are sold in their acid form and consequently form anions when dissolved in water. Pharmaceutical anions and their metabolites are a growing problem because of ineffective removal in most wastewater treatment facilities.[24] Resins with cationic groups and exchangeable counter anions are still considered the standard ion exchanger.[25,26] Due to their organic polymer nature, these resins are of limited thermal and chemical stability.[27] One alternative to possibly replace resins is layered double hydroxides (LDHs), an isostructural group of materials containing cationic brucite type layers that are charged balanced by

interlayer anions with general formula $[M^{2+}_{1-x}M^{3+}_{x}(OH)_2](A^{n-}_{x/n})\cdot xH_2O$ where M^{2+} and M^{3+} are a range of metals, A^{n-} is the intercalated anion, and x is ratio of $M^{3+}/(M^{2+} + M^{3+})$. LDHs suffer from low selectivity and re-intercalation of common anions such as carbonate or sulfate due to the memory effect.[28,29]

Owing to the structural diversity and weak host-guest interaction, cationic coordination polymers are gaining considerable attention for anion exchange. Silver-based CPs in particular have been previously studied for their ability to selectively trap anions *via* a crystal-to-crystal transition.[30,31] We reported silver(I) with 4,4-bipyridine polymers with ethanedisulfonate (EDS, $^{-}O_3S(CH_2)_2SO_3^{-}$) as a charge balance anion.[32] We subsequently reported oxo-anion pollutants exchange materials such as $[Cu_4(OH)_6^{2+}][EDS^{2-}]\cdot 2H_2O$[33] and $[M(H_2O)_n(4,4'\text{-bipyridine})_2^{2+}[EDS^{2-}]$ [M = Cu(I), Ag(I), Co(II) or Zn(II)].[32,34,35] We subsequently described silver-4,4'-bipyridine nitrate (SBN)[36,37] and acetate (SBA)[38] materials in the absence of EDS anions with even higher capacity, rate, selectivity and reversibility for trapping of perchlorate from water. Wang and coworkers recently reported a variety of cationic extended materials, denoted as SCU-n (Soochow University, structure No. n) with outstanding performance for TcO_4^{-}/ReO_4^{-} removal.[39–42] These authors also recently reported organic polymers with similar properties.[42,43] There have also been significant advances with selective crystallization approaches for anion removal[44] and very recently Zr_6O_8-based cationic MOFs, though the latter require ligands with multiple step syntheses and are somewhat limited in terms of selectivity.[45,46]

In this study, a variety of anionic pollutants including chromate, perrhenate (as an analog for pertechnetate) and α,ω-alkanedicarboxylates (as analogs for anionic pharmaceutical pollutants) were exchanged into the cationic CP Ag-pyrazine nitrate. The weak interaction between the interlamellar nitrates and the cationic silver pyrazine layers likely allows for the high capacity exchange.

2.2. Experimental

2.2.1. Reagents

Silver nitrate ($AgNO_3$, Alfa Aesar, 99%) and pyrazine [$(C_4H_4N)_2$, Acros Organics, 99%] were used as-received for the synthesis. For the exchange studies, the following were used as-purchased: potassium chromate (K_2CrO_4, Fischer Scientific), potassium permanganate ($KMnO_4$, Acros Organics), sodium tetrafluoroborate ($NaBF_4$, Acros Organics), potassium chloride (KCl, Fischer Scientific), potassium bromide (KBr, Acros Organics), potassium iodide (KI, Spectrum Chemical), sodium perrhenate ($NaReO_4$, Alfa Aesar), disodium malonate ($[^{-}O_2C\text{-}CH_2\text{-}CO_2^{-}]Na_2$, TCI America), disodium succinate ($[^{-}O_2C\text{-}(CH_2)_2\text{-}CO_2^{-}]Na_2$, TCI America), disodium glutarate ($[^{-}O_2C\text{-}(CH_2)_3\text{-}CO_2^{-}]Na_2$, TCI America), adipic acid ($[^{-}O_2C\text{-}(CH_2)_6\text{-}CO_2^{-}]Na_2$, TCI America), disodium sebacate ($[^{-}O_2C\text{-}(CH_2)_8\text{-}CO_2^{-}]Na_2$, TCI America), ascorbic acid ($C_6H_8O_6$, Fischer Scientific), salicylic acid ($HOC_6H_4CO_2H$, Fischer Scientific), terephthalic acid [$C_6H_4(CO_2H)_2$, TCI America], 2,6-naphthalene dicarboxylic acid ($C_{10}H_6(CO_2H)_2$, TCI America) and Purolite A530E (Purolite).

2.2.2. Synthesis

Silver nitrate and pyrazine (1:1 molar ratio) were added together in 10 mL of Millipore water and the mixture was kept at 70 °C for 1 h. The reaction mixture was then cooled in an ice bath and rinsed with cold water and acetone. The filtration gave rise to white needle-like small crystals (yield: 65.8% based on $AgNO_3$). Silver malonate direct synthesis was performed by mixing silver nitrate and sodium malonate (1:1 molar ratio) together in 10 mL of Millipore water and the mixture was stirred at room temperature for 1 h. The product was filtered and rinsed with water and acetone (yield: 63.4% based on $AgNO_3$).

2.2.3. Anion Exchange

The exchange reactions were performed by placing $[Ag(pyz)^+][NO_3^-]$ (0.2 mmol) and the anion of interest (0.2 mmol) in 10 mL of Millipore water. The resulting systems were kept under magnetic stirring at room temperature for 24 h. Equimolar quantities were used for all anion exchanges but modified if necessary according to the charge of the incoming anion. The selectivity tests were performed by introducing the material into a sealed beaker containing 10 mL Millipore water and the anion mixture of interest (0.2 mmol for both). The reaction was stirred for 24 h under ambient conditions.

2.2.4. Instrumental Details for Characterization

Powder X-ray Diffraction (PXRD) data were obtained on a Rigaku Americas Miniflex Plus powder diffractometer, scanning from 2° to 40° (2θ) at a rate of 3°·

min^{-1} with a 0.02° step size under Cu-Kα radiation (λ = 1.5418 Å). Inductively coupled plasma optical emission spectrometry (ICP-OES) data were acquired on a Perkin Elmer Optima 4300DV, run in radial mode using yttrium as an internal standard. Fourier Transform Infrared (FT-IR) data was collected on a Perkin Elmer, Spectrum One FT-IR spectrometer. Thermogravimetric analysis (TGA) was performed using a TA Instruments 2050 TGA, heating from 25 to 600 °C with a gradient of 10 °C/min and nitrogen flow. *In situ* variable temperature PXRD (VT-PXRD) was performed on a Rigaku SmartLab X-Ray Diffractometer with Cu-K□□radiation (□= 1.57418 Å) from 2° to 70° (2□) at a scan rate of 2°/min and 0.02° step size. The samples were heated at a rate of 10°C/min and held at the set temperature for 5 min before scanning. SEM images were collected with a FEI Quanta 3D Dualbeam microscope.

2.3. Results and Discussion

2.3.1. Synthesis and Structure Properties

The Ag(I) pyrazine structure (Scheme 1) was synthesized with both hydrothermal and room temperature condition. It was a slight modification of the literature method.[19] The crystals formed within 1 h under low heat, as evidenced by the match of experimental PXRD pattern to theoretical pattern simulated from single crystal data (Figure 1).

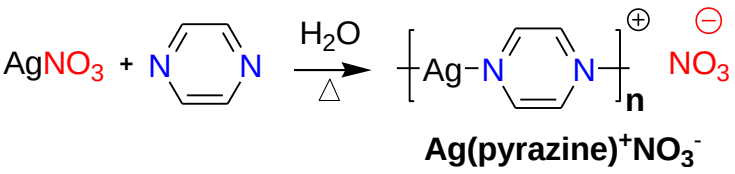

Scheme 2.1: Reaction scheme of [Ag(pyrazine)$^{+}$][NO_3^{-}].

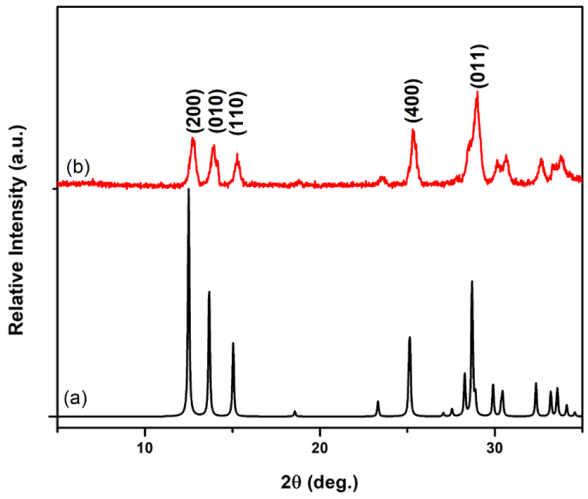

Figure 2.1: PXRD pattern of [Ag(pyrazine)$^{+}$][NO_3^{-}]: (a) theoretical; (b) as-synthesized.

Table 2.1: Crystal data and structure refinement of [Ag(pyrazine)$^{+}$][NO_3^{-}]

empirical formula	$C_4H_4AgN_3O_3$
formula weight (g)	249.97
wavelength (Å)	0.71073, Mo-Kα
crystal system	Triclinic
space group	$P\bar{1}$
unit cell dimensions (Å, °)	a = 3.4831(7)
	b = 6.4226(12)
	c = 14.177(3)
	α = 90.147(11)
	β = 95.880(14)
	γ = 90.159(19)
volume (Å^3)	315.48(11)
Z, calculated density (g/cm^3)	2, 2.623
absorption coefficient (mm^{-1})	3.147
color of crystal	colorless
θ range for data collection (°)	3.17 to 28.79
index ranges	$-4 \le h \le 4$, $-8 \le k \le 8$, $-19 \le l \le 3$
completeness to θ	95.9% (θ = 25.242°)
collected/unique reflections	1580/1501 [R(int) = 0.0453]
absorption correction	multi-scan
max. and min. transmission	0.478 and 0.746
refinement method	full-matrix least-squares on F^2

data / restraints / parameters	1580 / 36 / 101
goodness of fit on F^2	1.155
final indices [$I > 2\sigma$ (I)]	$R_1 = 0.0484$, $wR_2 = 0.1130$
R indices (all data)	$R_1 = 0.0541$, $wR_2 = 0.1181$
Largest diff. peak and hole ($e \cdot Å^{-3}$)	2.343 and –2.519

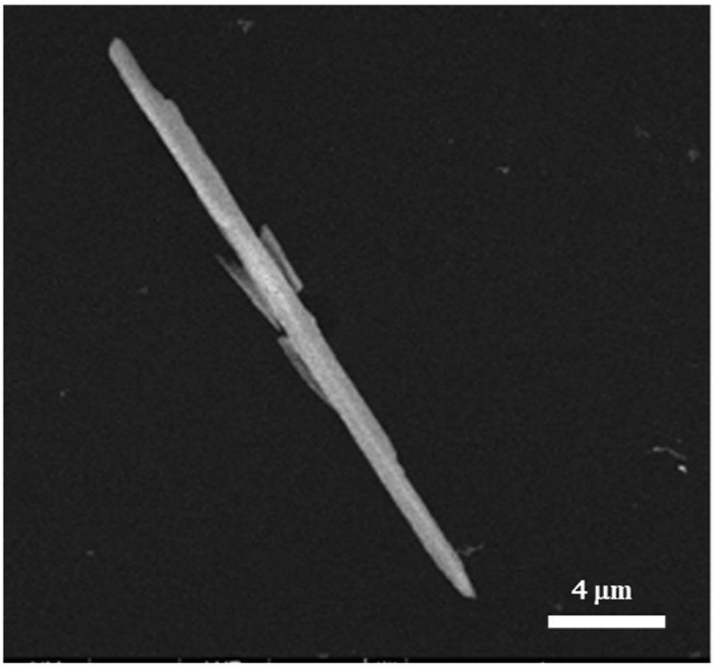

Figure 2.2: SEM image of a needle-shaped crystal of [Ag(pyrazine)$^+$][NO_3^-].

The silver pyrazine nitrate polymers crystallize as colorless needle crystals (Figure 2) and crystallographic data is summarized in Table 1. The crystals are in the $P\bar{1}$ space group of the triclinic crystal system. Single XRD revealed that the structure contains one dimensional silver(I) pyrazine chains □-stacked [3.483(2) to 3.975(4) Å] into layers with charge-balancing nitrate anions between the layers (Figure 3). The

chains are slightly kinked with Ag-N distance 2.211(7) to 2.229(7) Å (Table 2). Within the polymeric chain, the N–Ag–N is significantly bent at an angle of 157.4(2) °, likely due to the presence of weakly coordinating oxygen atoms of nearby nitrate anions. The bond length between Ag(I) and the oxygen from nitrate was 2.558(6) Å, creating weak covalent Ag-O bonds[47] that play a crucial role in the anion exchangeability (vi*de infra*).

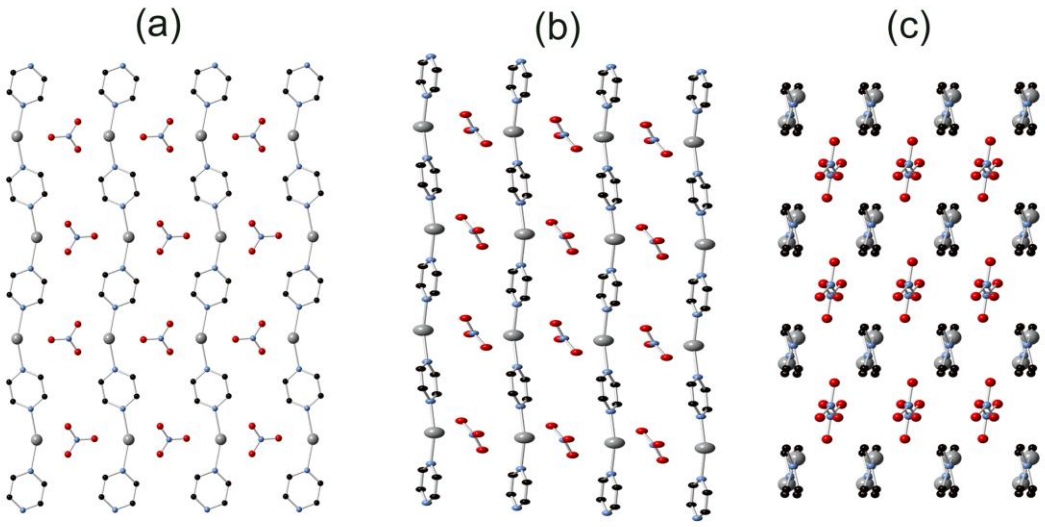

Figure 2.3: Crystallographic views of [Ag(pyrazine)$^{+}$][NO_3^{-}]: (a) *a*-projection; (b) *b*-projection;(c) *c*-projection (hydrogen atoms are omitted for clarity; silver = gray, nitrogen = blue, oxygen = red, carbon = black).

Table 2.2. Selected bond lengths (Å) and angles (º) in [Ag(pyrazine)$^{+}$][NO_3^{-}].

Ag(1)-N(1)	2.211(7) Å
Ag(1)-N(2)	2.229(7) Å
Ag(1)-O(2)	2.558(6) Å
N(2)-Ag(1)-N(2)	157.4(2) º

The thermal behavior of [Ag(pyrazine)$^{+}$][NO_3^{-}] was investigated by *in-situ* variable temperature powder X-ray diffraction (VT-PXRD) and thermogravimetric analysis (TGA), both under nitrogen (Figure 4). At 145 °C, an additionalcrystalline phase appeared [first peak ~ 12° (2θ)] and both are gone by 225 °C. The TGA trace showed a corresponding weight loss around 175 °C and is likely due to the partial loss of pyrazine (calculated: 20.8%, observed: 18.1%). At 400 °C, VT-PXRD shows a mixed phase of silver nitrate (ICDD PDF #00-043-0649), silver oxide (ICDD PDF #03-065-3289) and silver metal (ICDD PDF #01-071-5025).

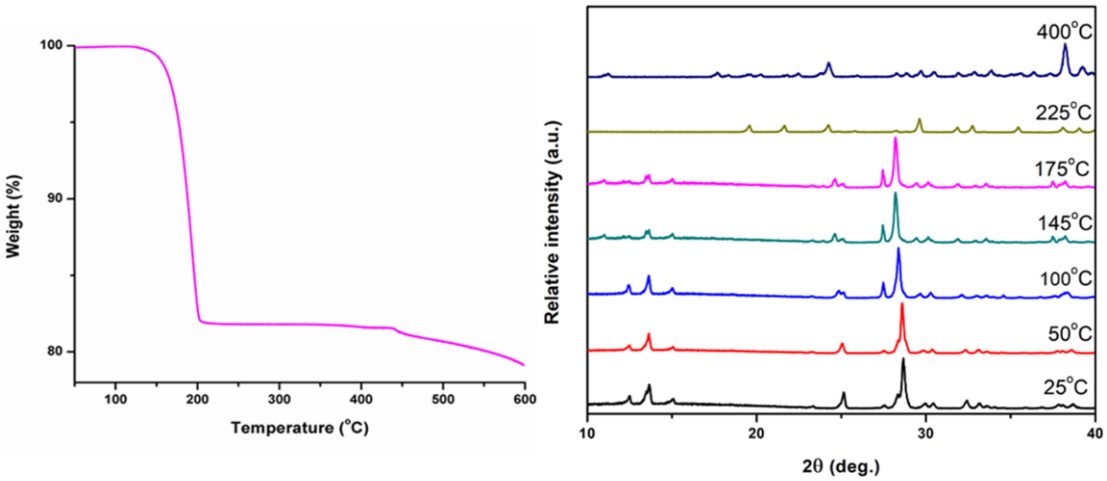

Figure 2.4: Thermal analysis of [Ag(pyrazine)$^{+}$][NO_3^{-}]: (left) TGA trace and (right) variable temperature PXRD.

2.3.2. Anion Exchange Results

All of the anion exchange studies of [Ag(pyrazine) $^{+}$][NO_3^{-}] were performed in aqueous conditions and pH 7. The first exchange investigated was organic using various α,ω-alkanedicarboxylate anions. An equimolar ratio of malonate, succinate, glutarate, adipate and sebacate in aqueous solution were tested (Figure 5). The principal peak of the as-synthesized nitrate-containing material is at 12.5° (2θ), corresponding to a basal spacing of 7.1 Å (Table 3). Based on the relative carbon chain length and size of carbonate end groups [$^{-}O_2C(CH_2)_nCO_2^{-}$], it was expected that succinate (n = 2), glutarate (n = 3), adipate (n = 4) and sebacate (n = 8) would shift the principal (200) peak to lower 2θ values as the interlayer distance

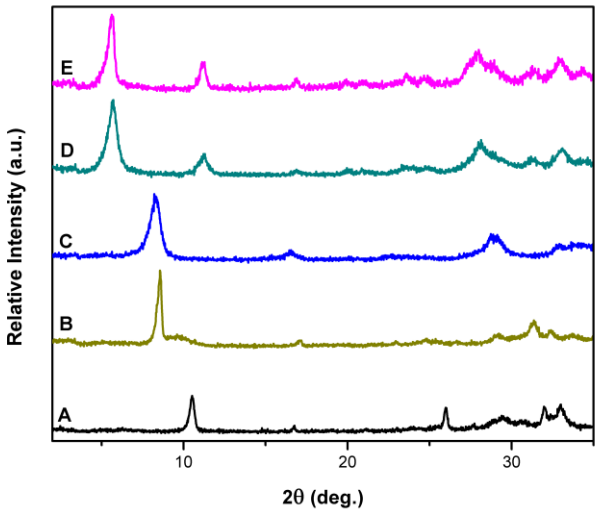

Figure 2.5: PXRD of as-synthesized $[Ag(pyrazine)^{+}][NO_3^{-}]$ (a) and after exchange with $[^{-}O_2C(CH_2)_nCO_2^{-}]$: (b) n = 1, malonate; (c) n = 2, succinate; (d) n = 3, glutarate; (e) n = 4, adipate; (f) n = 8, sebacate.

increases. Malonate (n = 1) shifted to higher 2θ value due to its shortest length. Exchange was confirmed by directly synthesizing silver malonate from silver nitrate and disodium malonate in a 1:1 ratio: the identical PXRD pattern was obtained (Figure 6c), with slight variation in intensity due to the fine microcrystalline nature of the directly synthesized material. As expected, longer carbon chains shifted the prominent peak to lower angle, with sebacate being the longest of the dicarboxylates tested (Table 3). Attempts to reverse the exchange have been unsuccessful to date, implying the organic-intercalated materials are of higher stability. The $[Ag(pyrazine)^{+}][^{-}O_2C(CH_2)_nCO_2^{-}]$ materials are thermally stable up to ### °C (Figure S1), which supports the irreversibility. The appearance of carboxylate peaks in the FTIR spectra also confirms that exchange has taken place (Figure 7). The C=O

and C-O stretches of carboxylate bands were found at 1570 and 1300 cm^{-1}, respectively.

Table 2.3. Principal PXRD peak (2θ and d-spacing values) for $[Ag(pyrazine)^{+}][NO_3^{-}]$ and the organic-exchanged materials

Anions	2θ (°)	d spacing (Å)
As synthesized	12.5	7.1
Malonate	16.6	5.3
Succinate	11.9	7.4
Glutarate	8.5	10.4
Adipate	8.0	11.0
Sebacate	5.7	15.5

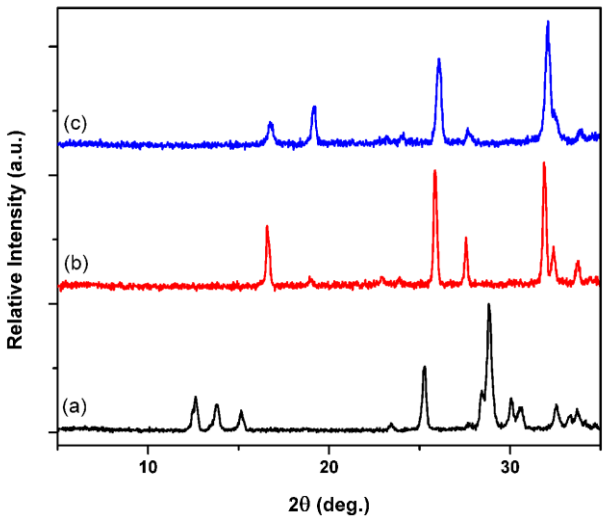

Figure 2.6: PXRD pattern of $[Ag(pyrazine)^{+}][NO_3^{-}]$: (a) as-synthesized (black); (b) exchanged with sodium malonate (red); (c) directly synthesized silver malonate (blue).

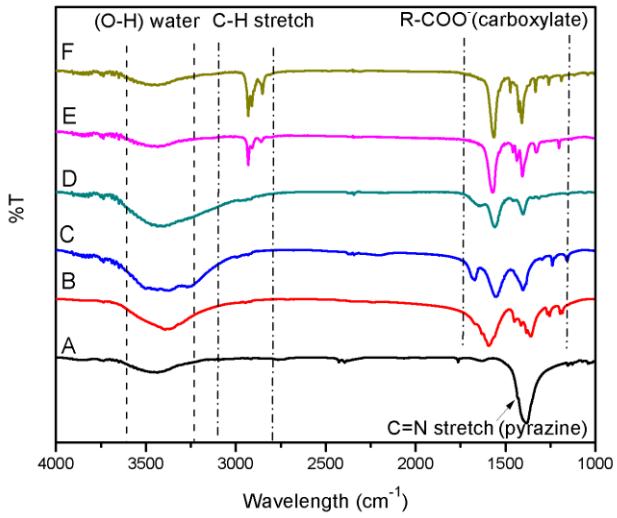

Figure 2.7: FTIR spectra of: (a) as-synthesized $[Ag(pyrazine)^{+}][NO_3^{-}]$;after exchange with $[^{-}O_2C(CH_2)_nCO_2^{-}]$: (b) n = 1, malonate; (c) n = 2, succinate; (d) n = 3, glutarate; (e) n = 4, adipate; (f) n = 8, sebacate.$^{-}$].

The selectivity amongst the α,ω-alkanedicarboxylates was also tested to see if there is a preference between them. The exchange started out with a mixture of even (C2, C4 and C8) or odd (C1, C3 and C8) carbon chain length dicarboxylates (Figure 8). In all tests, sebacate $[^{-}O_2C(CH_2)_8CO_2^{-}]$ was the only phase observed, likely due to its greater amphiphilicity and thus stability of the n = 8 phase *via* van der Waals packing.

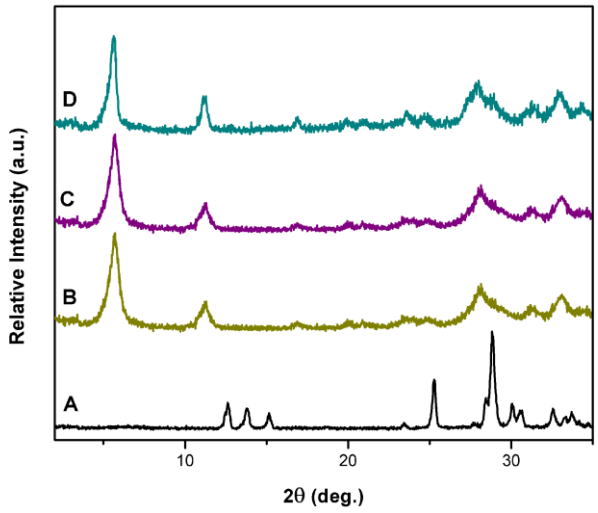

Figure 2.8: PXRD pattern of: (a) as-synthesized [Ag(pyrazine)$^{+}$][NO_3^{-}]; (b) the product after exchange with malonate, glutarate and sebacate in competition; (c) after succinate, adipate and sebacate in competition; (d) exchange with sebacate only.

In addition to α,ω-alkanedicarboxylates, the material displayed high capacity inorganic anion exchange for water-borne metal oxo-anion pollutants. Permanganate, tetrafluoroborate and perrhenate were studied. The latter was chosen as a group 7 surrogate for pertechnetate, which is a problematic radioactive pollutant during the vitrification of nuclear waste.[48] An equimolar amount of permanganate and as-synthesized [Ag(pyrazine)$^{+}$][NO_3^{-}] were introduced into aqueous solution under mild stirring. As monitored by UV-Vis spectroscopy, the permanganate concentration rapidly decreased by 32% to 57% with reaction intervals of 0.5 h to 3.5 h (Figure 9). The permanganate uptake was 92% after 24 h and the adsorption capacity was 435 mg/g.

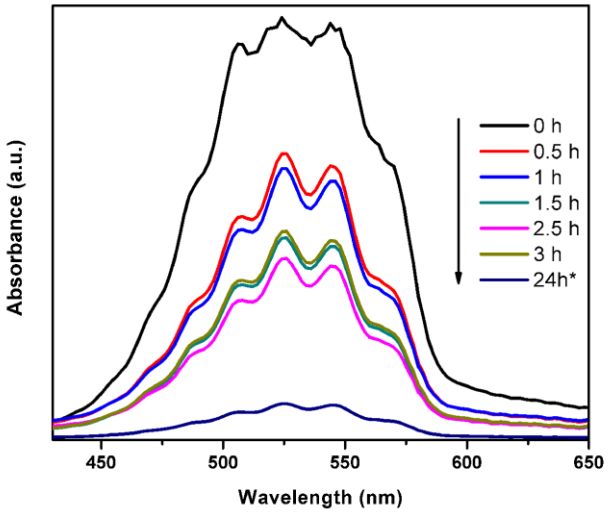

Figure 2.9: UV-Vis spectra of permanganate solution during anion exchange with $[Ag(pyrazine)^{+}][NO_3]^{-}$ at increasing time interval.

Similarly, perrhenate exchanged successfully according to PXRD (Figure 10), where the powder pattern correlated to the $[Ag(C_4H_4N_2)^{+}][ReO_4^{-}]$ structures from liteature.[49] ICP-OES was used to quantitatively monitor the Re uptake (Table 4, Figure 10), reaching over 82% removal from solution in 24h.

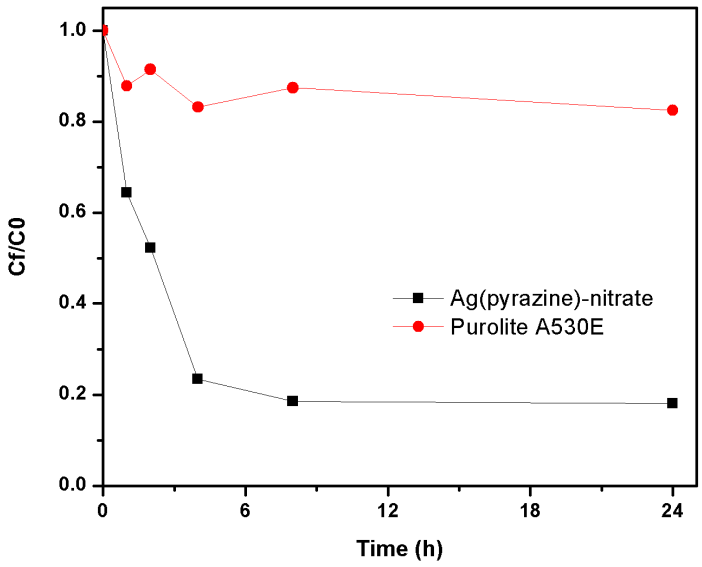

Figure 2.10: Concentration of Re based on ICP-OES vs. time for anion exchange by [Ag(pyrazine)$^{+}$] [NO_3^-] (black) and Purolite A530E (red).

Table 2.4. The adsorption capacity of 0.7 mmol of perrhenate in 50 mL aqueous solution with an equimolar ratio of [Ag(pyrazine)$^{+}$][NO_3^-] and Purolite A530E during 24 h intervals, as monitored by ICP-OES

Time (h)	[Ag(pyrazine)$^{+}$][NO_3^-]		Purolite A530E	
	Adsorption (mg/g)	Removal (%)	Adsorption (mg/g)	Removal (%)
1	355.2	35.6	121.6	12.2
2	476.6	47.8	85.6	8.6
4	764.7	76.6	167.7	12.6
8	812.6	81.4	125.5	16.8
24	818.0	82.0	175.0	17.5

The adsorption capacity of [Ag(pyrazine)$^{+}$][NO_3^-] is 818 mg ReO_4^-/g of material, higher than that of SLUG-21 (602 mg/g),[32] SCU-8 (534 mmol/mol),[39] SCU-100 (541

mg/g)[40], SCU-101 (217 mg/g)[42], NDTB (72% removal in 36h),[50] UiO-66-NH_3^+ (159 mg/g)[51] and SBN (786 mg/g).[43] The rate of uptake, however, is slower than that of SBN, SCU-8, SCU-100 and SCU-101. [Ag(pyrazine)$^+$][NO_3^-] is thus the best performing metal-organic based material in terms of capacity but did not outperform the recently reported organic polymer, SCU-CPN-1 (999 mg/g).[41] PXRD before and after anion exchange confirmed that [Ag(pyrazine)$^+$][NO_3^-] retains its crystalline layered character after intercalation, with the *d*-spacing slightly increasing from 7.0 to 7.4 Å due to the larger anion (Figure 11). The exchanges for both permanganate and perrhenate are permanent, and reusability is, in fact, undesirable for a highly problematic pollutant such as the radionuclide pertechnetate.

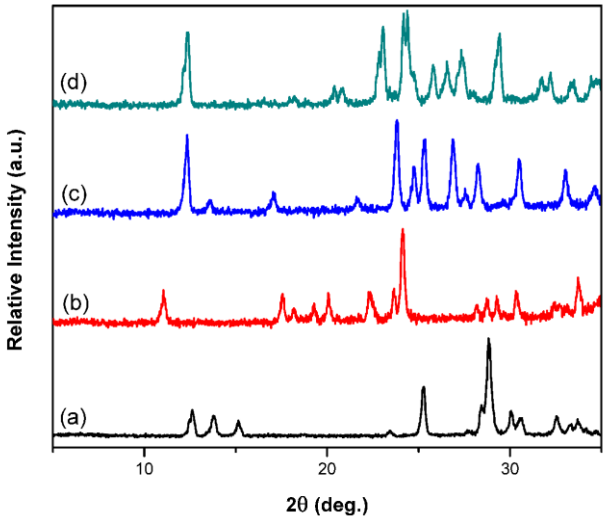

Figure 2.11: PXRD spectra of as-synthesized [Ag(pyrazine)$^+$][NO_3^-] (a) and after exchange with BF_4^- (b), MnO_4^- (c) and ReO_4^- (d).

Since BF_4^-, MnO_4^-, and ReO_4^- are all tetrahedral geometry, we were interested in the selectivity. According to PXRD data, perrhenate outperformed the other anions (Figure 12). We attempted to prepare crystals suitable for single crystal

X-ray diffraction in order to have a deeper understanding of the specific binding. Among them, only $[Ag(pyrazine)^{+}][ReO_4]^{-}$ successfully yielded colorless needle-type crystals, matching the theoretical pattern based on the crystal data reported by Maggard *et. al.*[49] The ReO_4^{-} tetrahedra, which reside in the spaces between the silver pyrazine layers, are separated at a distance of 4.61 Å from Ag-O-Re. the individual layers. Each ReO_4^{-} tetrahedron bonds via three O vertices to three different Ag^{+} in the layer [Ag–O distance 2.603(3) to 2.686(5) Å], with the fourth vertex either above or below the layer. Wang *et al*. showed that for $[Ag(4,4'\text{-bipyridine})^{+}][ReO_4]^{-}$, perrhenate has a stronger electrostatic interaction with the polymers that creates a better match of coordinating environment.

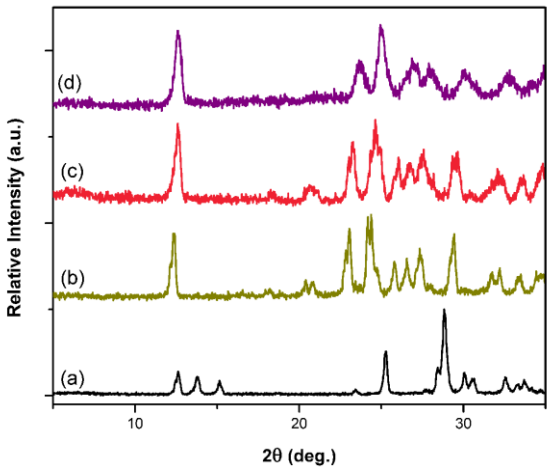

Figure 2.12: PXRD spectra of as- synthesized $[Ag(pyrazine)^{+}]\ [NO_3]^{-}$ (a) and after exchange with: (b) ReO_4^{-}; (c) BF_4^{-} and ReO_4^{-} in competition; (d) BF_4^{-}, MnO_4^{-} and ReO_4^{-} in competition.

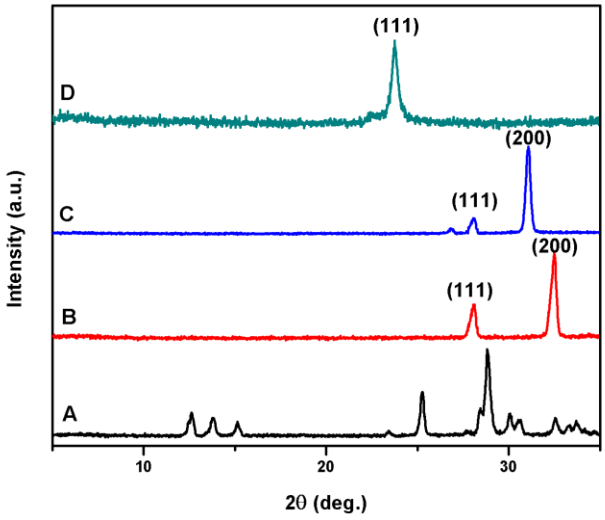

Figure 2.13: PXRD: (a) as- synthesized [Ag(pyrazine)$^{+}$][NO_3^{-}]; after exchange attempt with: (b) Cl^{-}; (c) Br^{-}; (d) I^{-}.

Attempts to exchange for Br^{-}, Cl^{-} and I^{-} were not successful since the silver strongly binds to the halide, forming the corresponding silver halide (Figure 13). Indeed, PXRD analysis charred the materials to a black color due to the sensitivity of silver halides to light.

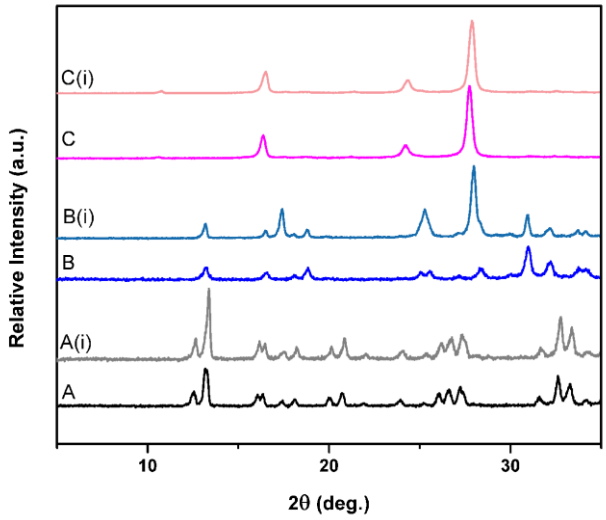

Figure 2.14: PXRD spectra of: (a) after exchange with salicylic acid; (a-i) directly synthesized silver salicylate; (b) after exchange with *p*-terephthalate; (b-i) directly synthesized silver terephthalate; (c) after exchange with 2,6-naphthalene dicarboxylate; (c-i) directly synthesizd silver 2,6-naphthalene dicarboxylate.

Attempts to intercalate other aromatic dicarboxylates such as salicylic acid, *p*-terephthalate, and 2,6-naphthalene dicarboxylate were not successful, likely due to the limited aqueous solubility of these analytes at neutral pH. Other reportsof the intercalation of terephthalate derivatives into cationic materials occurred in basic aqueous solutions.[52,53] PXRD data revealed that the exchange products turned out to be identical to the directly synthesized silver dicarboxylates (Figure 14), confirming that pyrazine in this case had been lost upon the exchange attempt.

2.4. Conclusions and Remarks

The cationic material silver(I) pyrazine shows the highest capacity to date for perrhenate (435 and 818 mg/g for permanganate and perrhenate, respectively) uptake for a metal-organic extended structure, making it potentially useful to trap pertechnetate. The capacity and kinetics far outperform the anion exchange resin Purolite 530E. Unlike some of the recently reported cationic MOFs, all of the synthesis and exchange occur aqueously, for the potential treatment of contaminated water. With the formation of a new crystal structure driving the reaction, the anions become permanently trapped. Reuse of the material would, in fact, be undesirable for a highly problematic radionuclide. The material also displays superior uptake toward over organic water-borne pollutants through a series of α,ω-alkanedicarboxylates. The ability to modify the linker of these types of N-donor Ag-based cationic materials opens up the possibility for further tuning the anion propensity and thus use towards water purification and pollution abatement.

2.5. References

(1) Jasinski, R. A New Fuel Cell Cathode Catalyst. *Nature* **1964**, *201* (4925), 1212–1213. https://doi.org/10.1038/2011212a0.

(2) Humphrey, S. M.; Wood, P. T. Multiple Areas of Magnetic Bistability in the Topological Ferrimagnet [Co3(NC5H3(CO2)2-2,5)2(M3-OH)2(OH2)2]. *J. Am. Chem. Soc.* **2004**, *126* (41), 13236–13237. https://doi.org/10.1021/ja046351l.

(3) Dong, Y.-B.; Jin, G.-X.; Smith, M. D.; Huang, R.-Q.; Tang, B.; zur Loye, H.-C. [Ag2(C33H26N2O2)(H2O)2(SO3CF3)2]·0.5C6H6: A Luminescent Supramolecular Silver(I) Complex Based on Metal−Carbon and Metal−Heteroatom Interactions. *Inorg. Chem.* **2002**, *41* (19), 4909–4914. https://doi.org/10.1021/ic020228i.

(4) Furukawa, H.; Cordova, K. E.; O'Keeffe, M.; Yaghi, O. M. The Chemistry and Applications of Metal-Organic Frameworks. *Science* **2013**, *341* (6149), 1230444. https://doi.org/10.1126/science.1230444.

(5) J. Oliver, S. R. Cationic Inorganic Materials for Anionic Pollutant Trapping and Catalysis. *Chem. Soc. Rev.* **2009**, *38* (7), 1868–1881. https://doi.org/10.1039/B710339P.

(6) Fujita, M.; Kwon, Y. J.; Washizu, S.; Ogura, K. Preparation, Clathration Ability, and Catalysis of a Two-Dimensional Square Network Material Composed of Cadmium(II) and 4,4'-Bipyridine. *J. Am. Chem. Soc.* **1994**, *116* (3), 1151–1152. https://doi.org/10.1021/ja00082a055.

(7) Seo, J. S.; Whang, D.; Lee, H.; Jun, S. I.; Oh, J.; Jeon, Y. J.; Kim, K. A Homochiral Metal–Organic Porous Material for Enantioselective Separation and Catalysis. *Nature* **2000**, *404* (6781), 982–986. https://doi.org/10.1038/35010088.

(8) Batten, S. R.; Robson, R. Interpenetrating Nets: Ordered, Periodic Entanglement. *Angew. Chem. Int. Ed.* **1998**, *37* (11), 1460–1494. https://doi.org/10.1002/(SICI)1521-3773(19980619)37:11<1460::AID-ANIE1460>3.0.CO;2-Z.

(9) Blake, A. J.; Champness, N. R.; Hubberstey, P.; Li, W.-S.; Withersby, M. A.; Schröder, M. Inorganic Crystal Engineering Using Self-Assembly of Tailored Building-Blocks. *Coord. Chem. Rev.* **1999**, *183* (1), 117–138. https://doi.org/10.1016/S0010-8545(98)00173-8.

(10) Hong, M.-C.; Chen, L. Design and Construction of Coordination Polymers. In *Silver(I) Coordination Polymers*; Su, C-Y.; John Wiley & Sons, Inc.: New Jersey, 2009; pp 111–144.

(11) Khlobystov, A. N.; Blake, A. J.; Champness, N. R.; Lemenovskii, D. A.; Majouga, A. G.; Zyk, N. V.; Schröder, M. Supramolecular Design of One-Dimensional Coordination Polymers Based on Silver(I) Complexes of Aromatic Nitrogen-Donor Ligands. *Coord. Chem. Rev.* **2001**, *222* (1), 155–192. https://doi.org/10.1016/S0010-8545(01)00370-8.

(12) Munakata, M.; Wu, L. P.; Kuroda-Sowa, T. Toward the Construction of Functional Solid-State Supramolecular Metal Complexes Containing Copper(I)

And Silver(I). In *Advances in Inorganic Chemistry*; Sykes, A. G., Ed.; Academic Press, 1998; Vol. 46, pp 173–303. https://doi.org/10.1016/S0898-8838(08)60151-8.

(13) Chen, C.-L.; Kang, B.-S.; Su, C.-Y. Recent Advances in Supramolecular Design and Assembly of Silver(I) Coordination Polymers. *Aust. J. Chem.* **2006**, *59* (1), 3–18.

(14) Stoehr, C. Ueber Pyrazine. *J. Für Prakt. Chem.* **1893**, *48* (1), 18–23. https://doi.org/10.1002/prac.18930480103.

(15) Wolff, L. Synthese Des Pyrazins. *Berichte Dtsch. Chem. Ges.* **1893**, *26* (2), 1830–1833. https://doi.org/10.1002/cber.189302602132.

(16) Schmidt, J. G.; Trimble, R. F. The Stability Constants of the Mono- and Dipyrazine Silver Complexes. *J. Phys. Chem.* **1962**, *66* (6), 1063–1065. https://doi.org/10.1021/j100812a022.

(17) Stidham, H. D.; Chandler, J. A. Chemical and Infra-Red Spectroscopic Studies of Metal(II) Halide Complexes of Pyrazine. *J. Inorg. Nucl. Chem.* **1965**, *27* (2), 397–403. https://doi.org/10.1016/0022-1902(65)80358-X.

(18) Pierce, J. L.; Busch, K. L.; Cooks, R. G.; Walton, R. A. Secondary-Ion Mass Spectra of Nonvolatile Silver Complexes. *Inorg. Chem.* **1983**, *22* (18), 2492–2494. https://doi.org/10.1021/ic00160a005.

(19) Vranka, R. G.; Amma, E. L. Metal Ion-Aromatic Complexes. II. The Crystal Structure of the 1:1 Silver Nitrate-Pyrazine Complex. *Inorg. Chem.* **1966**, *5* (6), 1020–1025. https://doi.org/10.1021/ic50040a016.

(20) Che, C.-M.; Lau, T.-C. Ruthenium and Osmium: High Oxidation States. In *Comprehensive Coordination Chemistry II*; McCleverty, J. A., Meyer, T. J., Eds.; Pergamon: Oxford, 2003; pp 733–847. https://doi.org/10.1016/B0-08-043748-6/04215-8.

(21) Keith, L.; Telliard, W. ES&T Special Report: Priority Pollutants: I-a Perspective View. *Environ. Sci. Technol.* **1979**, *13* (4), 416–423. https://doi.org/10.1021/es60152a601.

(22) Izak, P.; Hrma, P.; Arey, B. W.; Plaisted, T. J. Effect of Feed Melting, Temperature History, and Minor Component Addition on Spinel Crystallization in High-Level Waste Glass. **2001**, 13.

(23) Daughton, C. G. PPCPs in the Environment: Future Research — Beginning with the End Always in Mind. In *Pharmaceuticals in the Environment*; Springer, Berlin, Heidelberg, 2004; pp 463–495. https://doi.org/10.1007/978-3-662-09259-0_33.

(24) Castiglioni, S.; Bagnati, R.; Fanelli, R.; Pomati, F.; Calamari, D.; Zuccato, E. Removal of Pharmaceuticals in Sewage Treatment Plants in Italy. *Environ. Sci. Technol.* **2006**, *40* (1), 357–363. https://doi.org/10.1021/es050991m.

(25) Jana, S.; Praharaj, S.; Panigrahi, S.; Basu, S.; Pande, S.; Chang, C.-H.; Pal, T. Light-Induced Hydrolysis of Nitriles by Photoproduced α-MnO2 Nanorods on Polystyrene Beads. *Org. Lett.* **2007**, *9* (11), 2191–2193. https://doi.org/10.1021/ol070750e.

(26) Praharaj, S.; Nath, S.; Panigrahi, S.; Ghosh, S. K.; Basu, S.; Pande, S.; Jana, S.; Pal, T. Layer-by-Layer Deposition of Bimetallic Nanoshells on Functionalized Polystyrene Beads. *Inorg. Chem.* **2006**, *45* (4), 1439–1441. https://doi.org/10.1021/ic051915n.

(27) Mark, R.; Findley, W. N. Thermal Expansion Instability and Creep in Amine-Cured Epoxy Resins. *Polym. Eng. Sci.* **1978**, *18* (1), 6–15. https://doi.org/10.1002/pen.760180103.

(28) Chibwe, K.; Jones, W. Intercalation of Organic and Inorganic Anions into Layered Double Hydroxides. *J. Chem. Soc. Chem. Commun.* **1989**, *0* (14), 926–927. https://doi.org/10.1039/C39890000926.

(29) Hibino, T.; Tsunashima, A. Characterization of Repeatedly Reconstructed Mg−Al Hydrotalcite-like Compounds: Gradual Segregation of Aluminum from the Structure. *Chem. Mater.* **1998**, *10* (12), 4055–4061. https://doi.org/10.1021/cm980478q.

(30) Li, C.-P.; Chen, J.; Guo, W.; Du, M. Anion-Directed Assembly and Crystal Transformation of Ag(I) Coordination Polymers with a Versatile Tripyridyltriazole Ligand 3,4-Bis(2-Pyridyl)-5-(4-Pyridyl)-1,2,4-Triazole. *J. Solid State Chem.* **2015**, *223*, 95–103. https://doi.org/10.1016/j.jssc.2014.06.038.

(31) Du, M.; Zhao, X.-J.; Guo, J.-H.; R. Batten, S. Direction of Topological Isomers of Silver(i) Coordination Polymers Induced by Solvent , and Selective Anion-

Exchange of a Class of PtS-Type Host Frameworks. *Chem. Commun.* **2005**, *0* (38), 4836–4838. https://doi.org/10.1039/B508479B.

(32) Fei, H.; Bresler, M. R.; Oliver, S. R. J. A New Paradigm for Anion Trapping in High Capacity and Selectivity: Crystal-to-Crystal Transformation of Cationic Materials. *J. Am. Chem. Soc.* **2011**, *133* (29), 11110–11113. https://doi.org/10.1021/ja204577p.

(33) Fei, H.; Oliver, S. R. J. Copper Hydroxide Ethanedisulfonate: A Cationic Inorganic Layered Material for High-Capacity Anion Exchange. *Angew. Chem. Int. Ed.* **2011**, *50* (39), 9066–9070. https://doi.org/10.1002/anie.201104200.

(34) Fei, H.; Rogow, D. L.; Oliver, S. R. J. SLUG 22- Reversible Anion Exchange and Catalytic Properties of Two Cationic Metal−Organic Frameworks Based on Cu(I) and Ag(I). *J. Am. Chem. Soc.* **2010**, *132* (20), 7202–7209. https://doi.org/10.1021/ja102134c.

(35) Fei, H.; Han, C. S.; Robins, J. C.; Oliver, S. R. J. SLUG-35 A Cationic Metal–Organic Solid Solution Based on Co(II) and Zn(II) for Chromate Trapping. *Chem. Mater.* **2013**, *25* (5), 647–652. https://doi.org/10.1021/cm302585r.

(36) Colinas, I. R.; Silva, R. C.; Oliver, S. R. J. Reversible, Selective Trapping of Perchlorate from Water in Record Capacity by a Cationic Metal–Organic Framework. *Environ. Sci. Technol.* **2016**, *50* (4), 1949–1954. https://doi.org/10.1021/acs.est.5b03455.

(37) R. Colinas, I.; K. Inglis, K.; Blanc, F.; J. Oliver, S. R. Anion Exchange Dynamics in the Capture of Perchlorate by a Cationic Ag-Based MOF. *Dalton Trans.* **2017**, *46* (16), 5320–5325. https://doi.org/10.1039/C7DT00475C.

(38) Citrak, S. C.; Popple, D.; Delgado-Cunningham, K.; Tabler, K.; Bdeir, K.; Oliver, A. G.; Kvam, P. B.; Oliver, S. R. J. Extremely Rapid Uptake of Perchlorate with Release of an Environmentally Benign Anion: Silver Bipyridine Acetate. *Cryst. Growth Des.* **2018**, *18* (3), 1891–1895. https://doi.org/10.1021/acs.cgd.7b01797.

(39) Li, Y.; Yang, Z.; Wang, Y.; Bai, Z.; Zheng, T.; Dai, X.; Liu, S.; Gui, D.; Liu, W.; Chen, M.; et al. A Mesoporous Cationic Thorium-Organic Framework That Rapidly Traps Anionic Persistent Organic Pollutants. *Nat. Commun.* **2017**, *8* (1). https://doi.org/10.1038/s41467-017-01208-w.

(40) Sheng, D.; Zhu, L.; Xu, C.; Xiao, C.; Wang, Y.; Wang, Y.; Chen, L.; Diwu, J.; Chen, J.; Chai, Z.; et al. Efficient and Selective Uptake of TcO4– by a Cationic Metal–Organic Framework Material with Open Ag+ Sites. *Environ. Sci. Technol.* **2017**, *51* (6), 3471–3479. https://doi.org/10.1021/acs.est.7b00339.

(41) Li, J.; Dai, X.; Zhu, L.; Xu, C.; Zhang, D.; Silver, M. A.; Li, P.; Chen, L.; Li, Y.; Zuo, D.; et al. 99TcO4− Remediation by a Cationic Polymeric Network. *Nat. Commun.* **2018**, *9* (1). https://doi.org/10.1038/s41467-018-05380-5.

(42) Zhu, L.; Sheng, D.; Xu, C.; Dai, X.; Silver, M. A.; Li, J.; Li, P.; Wang, Y.; Wang, Y.; Chen, L.; et al. Identifying the Recognition Site for Selective Trapping of 99TcO4– in a Hydrolytically Stable and Radiation Resistant

Cationic Metal–Organic Framework. *J. Am. Chem. Soc.* **2017**, *139* (42), 14873–14876. https://doi.org/10.1021/jacs.7b08632.

(43) Zhu, L.; Xiao, C.; Dai, X.; Li, J.; Gui, D.; Sheng, D.; Chen, L.; Zhou, R.; Chai, Z.; Albrecht-Schmitt, T. E.; et al. Exceptional Perrhenate/Pertechnetate Uptake and Subsequent Immobilization by a Low-Dimensional Cationic Coordination Polymer: Overcoming the Hofmeister Bias Selectivity. *Environ. Sci. Technol. Lett.* **2017**, *4* (7), 316–322. https://doi.org/10.1021/acs.estlett.7b00165.

(44) Custelcean, R. Anions in Crystal Engineering. *Chem. Soc. Rev.* **2010**, *39* (10), 3675–3685. https://doi.org/10.1039/B926221K.

(45) Wang, T. C.; Vermeulen, N. A.; Kim, I. S.; Martinson, A. B. F.; Stoddart, J. F.; Hupp, J. T.; Farha, O. K. Scalable Synthesis and Post-Modification of a Mesoporous Metal-Organic Framework Called NU-1000. *Nat. Protoc.* **2016**, *11* (1), 149–162. https://doi.org/10.1038/nprot.2016.001.

(46) Drout, R. J.; Otake, K.; Howarth, A. J.; Islamoglu, T.; Zhu, L.; Xiao, C.; Wang, S.; Farha, O. K. Efficient Capture of Perrhenate and Pertechnetate by a Mesoporous Zr Metal–Organic Framework and Examination of Anion Binding Motifs. *Chem. Mater.* **2018**, *30* (4), 1277–1284. https://doi.org/10.1021/acs.chemmater.7b04619.

(47) Lindley, P. F.; Woodward, P. An X-Ray Investigation of Silver Nitrate: A Unique Metal Nitrate Structure. *J. Chem. Soc. Inorg. Phys. Theor.* **1966**, *0* (0), 123–126. https://doi.org/10.1039/J19660000123.

(48) Braterman, P. S.; Phol, P. I.; Xu, Z.-P.; Brinker, C. J.; Yang, Y.; Bryan, C. R.; Yu, K.; Xu, H.; Wang, Y.; Gao, H. *Potential Applications of Nanostructured Materials in Nuclear Waste Management.*; SAND2003-3313, 917460; 2003. https://doi.org/10.2172/917460.

(49) Lin, H.; Yan, B.; Boyle, P. D.; Maggard, P. A. Synthesis and Properties of Pyrazine-Pillared Ag3Mo2O4F7 and AgReO4 Layered Phases. *J. Solid State Chem.* **2006**, *179* (1), 217–225. https://doi.org/10.1016/j.jssc.2005.10.037.

(50) Wang, S.; Alekseev, E. V.; Diwu, J.; Casey, W. H.; Phillips, B. L.; Depmeier, W.; Albrecht-Schmitt, T. E. NDTB-1: A Supertetrahedral Cationic Framework That Removes TcO4− from Solution. *Angew. Chem. Int. Ed.* **2010**, *49* (6), 1057–1060. https://doi.org/10.1002/anie.200906397.

(51) Banerjee, D.; Xu, W.; Nie, Z.; Johnson, L. E. V.; Coghlan, C.; Sushko, M. L.; Kim, D.; Schweiger, M. J.; Kruger, A. A.; Doonan, C. J.; et al. Zirconium-Based Metal–Organic Framework for Removal of Perrhenate from Water. *Inorg. Chem.* **2016**, *55* (17), 8241–8243. https://doi.org/10.1021/acs.inorgchem.6b01004.

(52) Millange, F.; Walton, R. I.; Lei, L.; O'Hare, D. Efficient Separation of Terephthalate and Phthalate Anions by Selective Ion-Exchange Intercalation in the Layered Double Hydroxide Ca2Al(OH)6·NO3·2H2O. *Chem. Mater.* **2000**, *12* (7), 1990–1994. https://doi.org/10.1021/cm0002057.

(53) Crepaldi, E. L.; Tronto, J.; Cardoso, L. P.; Valim, J. B. Sorption of Terephthalate Anions by Calcined and Uncalcined Hydrotalcite-like

Compounds. *Colloids Surf. Physicochem. Eng. Asp.* **2002**, *211* (2), 103–114. https://doi.org/10.1016/S0927-7757(02)00233-9.

Chapter (3)

Design and Synthesis of Two Cationic Silver Quinoxaline Coordination Polymers

Abstract

We report two cationic silver-based coordination polymers with N-donating quinoxaline as the linker. $[Ag(quinoxaline)^{+}][^{-}O_3S(CH_2)_2\,SO_3^{-}]_{0.5}\cdot 2H_2O$ (which we denote as SLUG-37 for University of California, Santa Cruz, structure No. 37; quinoxaline = $C_8H_6N_2$) and $[Ag(quinoxaline)^{+}][CH_3CO_2^{-}]$ (SLUG-38) were solved by single crystal X-ray diffraction and further characterized by several solid-state techniques. Both structures consist of cationic 1D Ag-quinoxaline chains arranged into π-stacked layers, with charge-balancing anions residing in the interlamellar space. The materials can be synthesized hydrothermally as well as in higher yield by reflux or room temperature conditions. Both display excellent thermal stability to 350 °C as evidenced by thermogravimetric analysis and variable temperature powder X-ray diffraction. The luminescent behavior of SLUG-37 exhibits a strong white emission making it potentially useful as white LEDs.

3.1. Introduction

3.1.1. Silver Quinoxaline Coordination Polymers

Coordination polymers (CPs) are generally defined as covalently extended compounds in which metal ions or metal-containing clusters act as nodes and organic ligands as linkers [1]. Inorganic coordination polymers are mostly inherently negative or neutral since low-valent metals are surrounded by at least several negative ligands. The formation of positively charged building blocks thus goes against the natural tendency of the species involved [2]. A breakthrough came in 2001 when Oliver lab introduced cationic BING-5 structure where nitrate and lead fluoride was mixed in the correct ratio and conditions.[3] Since then, numerous cationic extended materials have been reported for anion exchange properties [4–6].

Silver(I) CPs are interesting not only because of their structural diversity but also due to their rich physiochemical properties, which might find applications in conductive materials, antibacterial agents, luminescent materials, ion exchange, gas adsorption and supramolecular chirality.[2,3] Due to its flexible coordination sphere, the Ag^{+} ions vary from linear to octahedral geometry. A large number of silver(I) coordination polymers therefore exist, with diverse topologies and dimensionalities [9]. The most common coordination mode in silver(I) CPs is linear or angular geometries. For example, $[AgL^{+}][C_3F_7CO_3^{-}]$ (where L is a bent-shaped bipyridine ligand with a dendritic ethylene oxide unit) gives a zigzag one-dimensional (1D) chain.[10] Other interesting Ag^{+}-based CP geometries include trigonal planar with the tripodal ligand *cis,trans*-1,3,5-triaminocyclohexane[11]. Another is the tetrahedral with the tetradentate

ligand 2,3,4,5-tetra(4-pyridyl)thiophene[12], resulting in a three-dimensional (3D) framework $[AgL^+][X^-]$ ($X^- = BF_4^-, PF_6^-$ or AsF_6^-). Using six bis(monodentate) pyrazine ligands, Ag^+ adopts octahedral geometry, forming a six-connected 3D network with the □-polonium topology [13]. This rational design of organic linker contributes to the structure diversity and enriches the properties and potential uses of silver(I) CPs.

Nitrogen containing heterocyclic derivatives are excellent neutral ligands for generating cationic architectures together with metal cations. Among the ligands, quinoxalines are good candidates for molecular building blocks because of their rod-like rigidity and length. The first silver quinoxaline structures, $[Ag_2(C_8H_6N_2)_2{}^{2+}][ClO_4^-]_2$ and $[Ag(C_8H_6N_2)^+][ClO_4^-]$ and $[Ag_2(C_8H_6N_2)_4{}^{2+}][NO_3^-]_2$, were reported in 1989 [14]. Many silver(I) CPs based on quinoxaline, pyrazine and their derivatives have been studied for their antimicrobial and luminescent properties [10-11]. Several organosulfonates can be used as the counter-anion to form these extended networks, such as trifluoromethanesulfonate or phenyl sulfonate [17]. Our group and others have used 1,2-ethanedisulfonate [EDS, $^-O_3S(CH_2)_2SO_3^-$] as a structure directing agent for layered inorganic-organic hybrids such as $Cu[O_3S(CH_2)_2SO_3]\cdot 4H_2O$[18], $Cu_4(OH)_6[O_3S(CH_2)_2SO_3]\cdot 2H_2O$ [19], $Co_7(OH)_{12}[O_3S(CH_2)_2SO_3]\cdot 2H_2O$[20], $Pb_2F_2[O_3S(CH_2)_2SO_3]$[21], and $Er_{12}(OH)_{29}(H2O)_5[O_3S(CH_2)_2SO_3]_{3.5}\cdot 5H_2O$[22] where at least one sulfonate oxygen covalently bonds to the inorganic layer. EDS resides in the interlamellar region and charge-balances the extended structure. Due to this

precedence, we have investigated silver(I) with quinoxaline as linker and EDS as structure directing agent.

3.1.2. Luminescent Applications

The presence of both inorganic and organic components in CPs make them very promising as a multifunctional luminescent material.[18,19] The metal ions and/or conjugated organic moieties can provide a platform to generate emission. CPs have thus far been investigated for luminescent properties owing to: (i) higher thermal stability compared to organic chromophores; (ii) structural diversity and modulability; (iii) tunability of emission behavior by structure type; (iv) amenability to application development due to their crystalline nature.[20,21] In general, silver(I) polymeric complexes exhibit emission bands that can originate from any of $n \rightarrow \pi$, $\pi \rightarrow \pi^*$ intraligand, metal-to-ligand charge transfer (MLCT), ligand-to-metal charge transfer (LMCT), ligand-to-ligand charge transfer (LLCT) [27]. Luminescent CPs have attracted significant attention due to their potential use in light-emitting diodes (LEDs), chemical sensors and photochemical applications [25]. Among the various chemical aspects of quinoxaline, we focus on its versatility to afford a material luminescent at room temperature. Metal quinoxaline complexes reported thus far are weakly emissive compounds (quantum yield: 0.18 ± 0.08) [28]. For the silver coordination polymer $[Ag(C_8H_6N_2)^+][NO_3^-]$, a weakly luminescent material was reported with potential use as a luminescent probe [29]. Here, we report two new silver quinoxaline CPs using EDS and acetate as charge-balancing anion.

3.2. Experimental

3.2.1. Reagents

Silver acetate ($AgCH_3CO_2$ Fisher, 99%), 1,2-ethanedisulfonate disodium salt [EDS Na_2: $O_3SCH_2CH_2SO_3Na_2$), Acros Organics, 96%)], 1,2-ethanedisulfonic acid dihydrate (EDSA: $HO_3SCH_2CH_2SO_3H{\cdot}2H_2O$, TCI America, 95%) and quinoxaline ($C_8H_6N_2$, Sigma-Aldrich, ≥ 95%) were used as-received.

3.2.2. Synthesis

SLUG-37

Yellow-orange needle-like crystals of $[Ag(quinoxaline)^+][^-O_3SCH_2CH_2SO_3^-]_{0.5}{\cdot}H_2O$ (which we denote as SLUG-37, for University of California, Santa Cruz, structure No. 37) were synthesized under hydrothermal conditions. $AgCH_3CO_2$ (0.17 g, 1.0 mmol), quinoxaline (0.17 g, 1.3 mmol) and 1,2-ethanedisulfonate disodium salt (0.23 g, 1.0 mmol) or 1,2-ethanedisulfonic acid dihydrate (0.19 g, 1.0 mmol) were added to deionized water (10 mL) in 1.0 : 1.3 : 1.0 : 400 molar ratios, respectively. The reaction mixture was stirred at room temperature for 15 min and transferred into a 15mL capacity Teflon line autoclave filled to 2/3 capacity. The autoclave was heated statically in an oven at a given temperature (between 100 and 150 °C) for 1 to 5 d. SLUG-37 can also be synthesized by refluxing or stirring at room temperature. These latter reactions were carried out with the same ratio of reactants and the crystals were filtrated after *ca*. 1 h of refluxing at 70 °C or after 1 d of stirring at room temperature. SLUG-37 yield was 66% (0.24 g) for hydrothermal, 85% (0.31 g) for

refluxing and 74% (0.27 g) for room temperature. Elemental analysis (Galbraith Laboratories, Inc., Knoxville, TN): 29.12% C (calculated: 28.90%), 3.09% H (calculated: 5.01%) and 7.50% N (calculated: 7.49%).

SLUG-38

Yellow crystals of [Ag(quinoxaline)$^{+}$][$CH_3CO_2^{-}$] (which we denote as SLUG-38, for University of California, Santa Cruz, structure No. 38) were synthesized through hydrothermal conditions. $AgCH_3CO_2$ (0.17 g, 1.0 mmol) and quinoxaline (0.13 g, 1.0 mmol) were added to deionized water (10 mL) in 1.0 : 1.0 : 400 molar ratios, respectively. The reaction mixture was stirred at room temperature for 15 min and transferred into a 15mL capacity Teflon line autoclave filled to 2/3 capacity. The autoclave was heated statically in an oven at 125 °C for 5 d. The yield was 74% based on silver acetate.

3.3. Results and Discussion

3.3.1. Crystal Structure and Characterization

SLUG-37 and SLUG-38 crystals can be synthesized hydrothermally with reproducible crystal size and morphology (Scheme 1, Figure 1). SLUG-37 crystals are long needles ~ 400 μm × 50 μm in size whereas SLUG-38 crystals are rectangular plates ~ 600 μm × 200 μm in size. SLUG-37 could form over the temperature range 100 – 150 °C and 1 to 5 d. Reflux and room temperature conditions gave smaller blocks of SLUG-37 (Figure 1b,c) but approximately the same yield as hydrothermal conditions. SLUG-38 could only be achieved by hydrothermal synthesis 150 °C for 5 d and the block crystals stacked compactly together (Figure 1d). SLUG-38 could not formed by reflux or room temperature methods, likely due to its lower stability (*vide infra*).

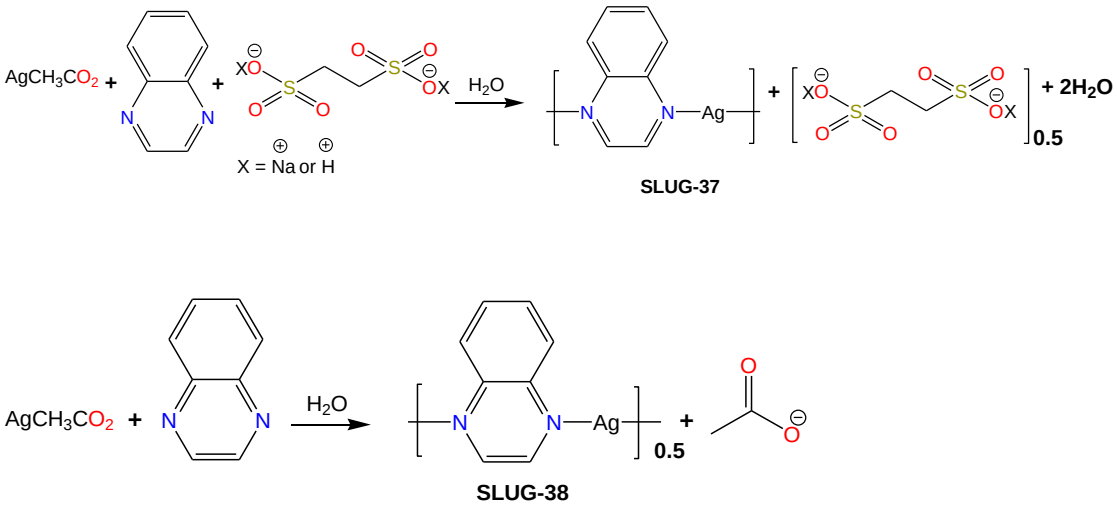

Scheme 3.1. Reaction scheme of SLUG-37 and SLUG-38.

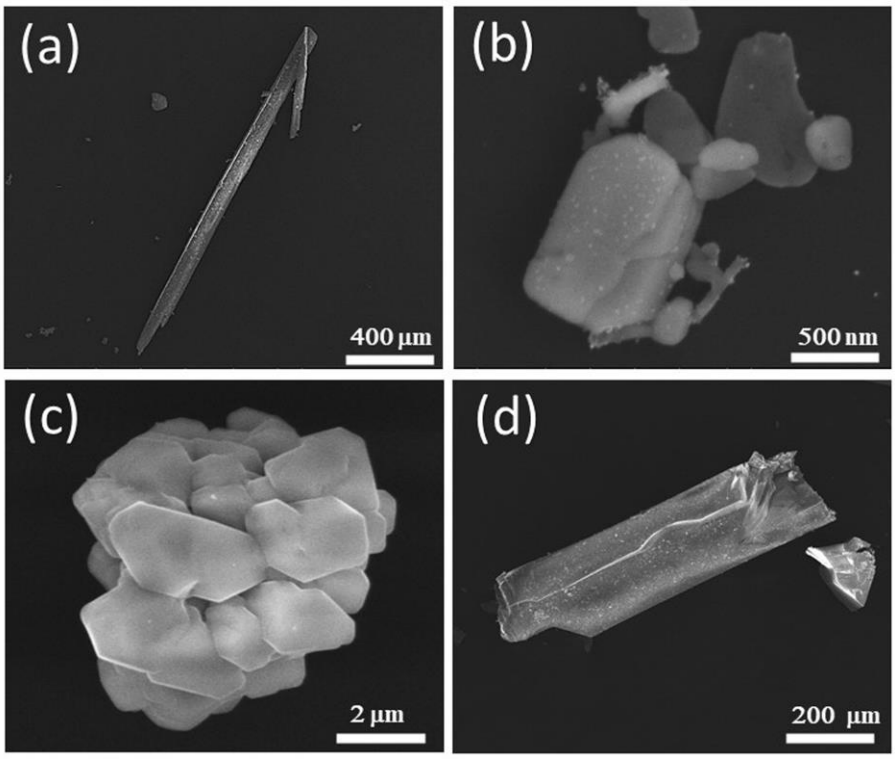

Figure 3.1. SEM images of: (a) SLUG-37 from hydrothermal conditions; (b) SLUG-37 from refluxing; (c) SLUG-37 from room temperature stirring; (d) SLUG-38 from hydrothermal conditions.

The PXRD of SLUG-37 prepared from the three methods confirms that the products are the identical phase and match the theoretical pattern based on the single crystal solution (Figure 2). Elemental analysis of as-synthesized SLUG-37 agrees well with the expected values based on the stoichiometric empirical formula (see Experimental Section, above).

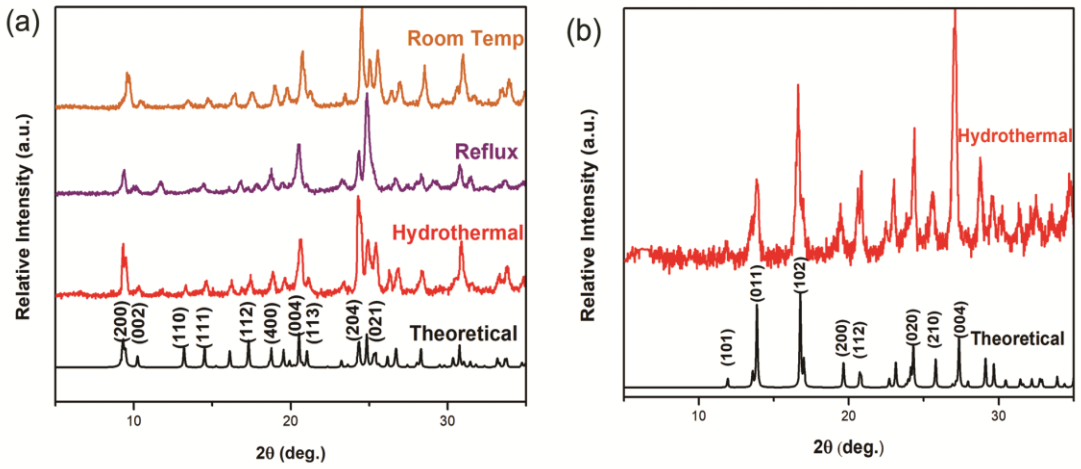

Figure 3.2. PXRD of as-synthesized: (a) SLUG-37 prepared by hydrothermal methods, reflux, and stirring at room temperature (theoretical pattern based on the CIF is shown at the bottom); (b) SLUG-38 from hydrothermal methods and its theoretical pattern.

SLUG-38 could only be achieved by hydrothermal synthesis at 150 °C for 5 d and the block crystals stacked compactly together (Figure 1d). SLUG-38 could not form by reflux or room temperature methods, likely due to its lower stability (*vide infra*). SLUG-38 crystals are rectangular plates ~ 600 μm × 200 μm in size. SLUG-38 also matches its theoretical PXRD pattern.

Single X-ray analysis reveals that SLUG-37 crystallizes in the monoclinic space group C2/c and SLUG-38 crystallizes in the orthorhombic space group *Pnma* (Figure 3, Table 1). For both, the quinoxaline bridges the silver centers into a 1D cationic polymer chain, $[Ag(quinoxaline)^{+}]_{\infty}$. In SLUG-37, the chains are arranged into layers, with the EDS anions residing in the interlamellar space. The interlayer π-π interaction are between the aromatic groups of the quinoxaline ligands with centroid-

to-centroid distances of 3.808(2) to 3.860(6) Å (Figure 4) [34]. The Ag^{+} ion of SLUG-37 is coordinated to two nitrogen atoms, one for each nearest quinoxaline with Ag-N distance 2.194(2) to 2.195(2) Å. The bond angle of N(1)-Ag(1)-N(2) is 169.86(8) and indicative of the presence of slight distortion. This distortion may be attributed to the strong interaction between Ag(I) and the adjacent oxygen of the EDS linker with Ag-O distance in the range of 2.580(4) Å (Figure 4, Table 2). The literature covalent bond length values between Ag (I) and a sulfonate oxygen range from 2.44 to 2.67 Å [30-31]. The remaining two oxygens of each sulfonate end are attributed to non-classical hydrogen bonds[37] to the C-H groups of quinoxaline, creating a linear contact in the range of 3.299(4) to 3.331(3) Å (Table 3). The large degree of electrostatic interaction further accounts for the structural and chemical stability. It also accounts for the inability in all attempts thus far to exchange the ethanedisulfonate anions with other anions in solution such as nitrate, perchlorate, permanganate or chromate.

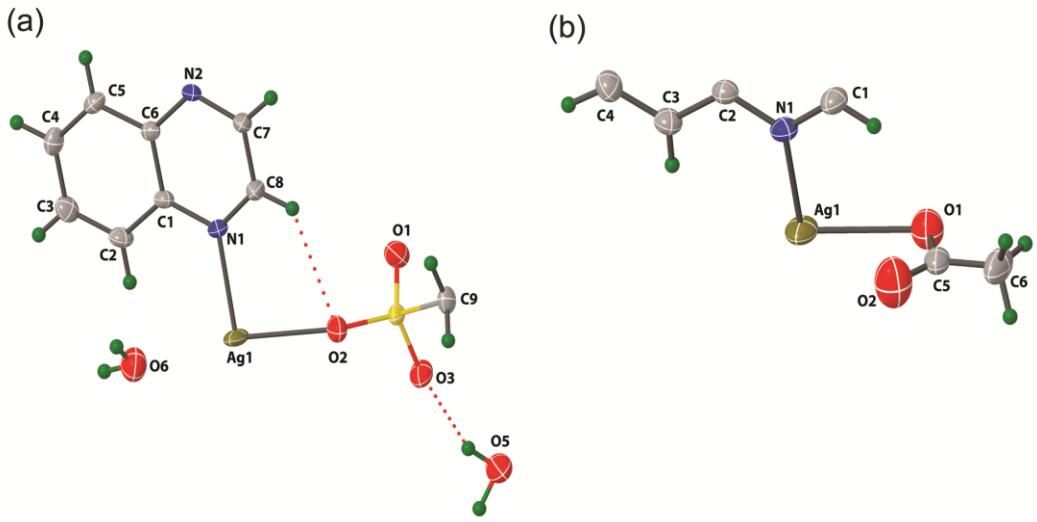

Figure 3.3. ORTEP diagram and atomic labeling of SLUG-37 (left) and SLUG-38 (right).

Table 3.1. Crystal data and structure refinement of SLUG-37 and SLUG-38

	SLUG-37	SLUG-38
empirical formula	$C_9H_8AgN_2O_3S.2(H_2O)$	$C_{10}H_9Ag_2N_2O_2$
formula weight (g)	368.14	297.06
wavelength (Å)	0.71073 Mo-Kα	0.71073 Mo-Kα
crystal system	monoclinic	orthorhombic
space group	C2/c	Pnma
unit cell dimensions (Å)	a = 19.326(4)	a = 9.0264(18)
	b = 7.174(2)	b = 7.330(14)
	c = 17.647(4)	c = 13.210(3)
	β =101.97(3)°	$\alpha = \beta = \gamma =$ 90°
volume ($Å^3$)	2397.0 (10)	874.4 (3)

Z, calculated density (mg/m^3)	8, 12.099	4, 2.257
absorption coefficient (mm^{-1})	1.870	2.280
crystal size (mm)	$0.2 \times 0.08 \times 0.04$	$0.22 \times 0.15 \times 0.10$
color of crystal	orange-yellow	yellow
θ range for data collection (°)	2.848 to 25.048	2.733 to 28.364
index ranges	$-22 \leq h \leq 21$, $-8 \leq k \leq 8$, $-21 \leq l \leq 20$	$-10 \leq h \leq 12$, $-9 \leq k \leq 9$, $-17 \leq l \leq 17$
completeness to θ	98.9% (θ = 25.048)	99.9% (θ = 26.000)
collected/unique reflections	5964/2037 [R(int) = 0.022]	6455/1156 [R(int) = 0.0157]
absorption correction	semi-empirical	semi-empirical
max. and min. transmission	0.651 and 0.745	0.7457 and 0.5675
refinement method	full-matrix least-squares on F^2	full-matrix least-squares on F^2
data / restraints / parameters	2037 / 1 / 179	1165 / 0 / 77
goodness of fit on F^2	1.294	1.085
final indices [$I > 2\sigma(I)$]	$R_1 = 0.0230$, $wR_2 = 0.0640$	$R_1 = 0.0400$, $wR_2 = 0.1060$
R indices (all data)	$R_1 = 0.0301$, $wR_2 = 0.1080$	$R_1 = 0.0423$, $wR_2 = 0.1084$
Largest diff. peak and hole ($e \cdot Å^{-3}$)	0.46 and –0.54	1.43 and –1.221

SLUG-38 also adopts layers of parallel $[Ag(quinoxaline)^{+}]_{\infty}$ chains with silver ions again covalently connected to the nitrogen atoms of the quinoxaline ligands as well as the oxygen atoms of the anion, in this case, acetate: Ag(1)-N(1) 2.282(3) Å and Ag(1)-O(2) 2.567(5) Å (Figure 3, Table 2). The Ag-quinoxaline layers have much longer quinoxaline π-π stacking distances between adjacent 1D chains [4.916(5) to 5.020(4) Å][34]. The two oxygens of the acetate are attributed to non-classical hydrogen bonds [37] to the C-H molecules of quinoxaline in the range of 3.32(6) to 3.55(5) Å (Figure 4,Table 3). Considering the structure, SLUG-38 is less stable than SLUG-37. As a result, the former is somewhat challenging to synthesize, and anion exchange could not be investigated.

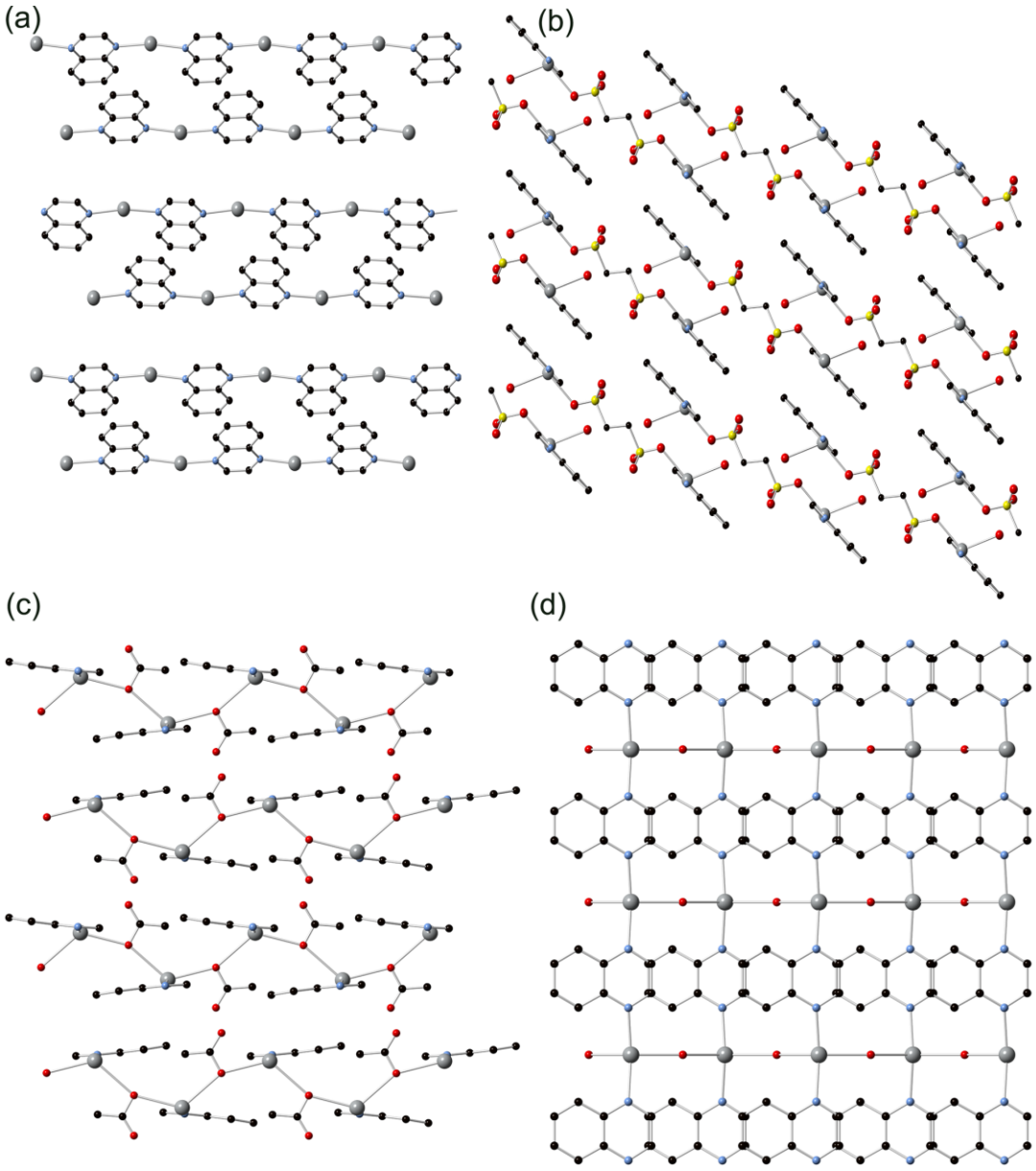

Figure 3.4. Crystallographic views of the two structures with hydrogen atoms omitted for clarity. (a) *a*-projection of SLUG-37; (b) *b*-projection of SLUG-37; (c) *b*-projection of SLUG-38; (d) *c*-projection of SLUG-38 (silver = gray, sulfur = yellow, nitrogen = blue, oxygen = red, carbon = black).

Table 3.2. Selected bond lengths (Å) and angles (°) in SLUG-37 and SLUG-38

SLUG-37		SLUG-38	
Ag(1)-N(1)	2.195(2)	Ag(1)-N(1)	2.282(3)
Ag(1)-N(2)[a]	2.194(2)	Ag(1)-O(2)	2.567(5)
Ag(1)-O(2)	2.580(2)		
N(2)-Ag(1)-N(1)[a]	169.86(8)	N(1)-Ag(1)-N(1)[b]	

Symmetry transformations used to generate equivalent atoms: (a) x,y+1,z; (b) x, -y+3/2,z.

Table 3.3. Non-classical hydrogen bonding distances (Å) and angles (°) in SLUG-37 and SLUG-38

	D—H···A	*d*(D—H)	*d*(H···A)	*d*(D···A)	<(D—H···A)
SLUG-37	C(2)—H(2)···O(2)[c]	0.93 (6)	2.59 (4)	3.331 (3)	137.2 (10)
	C(2)—H(2)···O(1)[c]	0.93 (5)	2.53 (5)	3.309 (3)	142.4 (11)
	C(1)—H(1)···O(2)	0.93 (5)	2.57 (5)	3.299 (4)	134.5 (10)
SLUG-38	C(3)—H(3)…O(1)[d]	0.93 (6)	2.75 (6)	3.320 (5)	121.0 (10)
	C(1)—H(1)…O(1)	0.93 (4)	2.74 (5)	3.442 (4)	133.1 (11)
	C(1)—H(1)…O(2)	0.93 (4)	2.89 (4)	3.536 (5)	128.3 (11)

Symmetry transformations used to generate equivalent atoms: (c) x,y-1,z; (d)-x-1, y+3/2,-z+1.

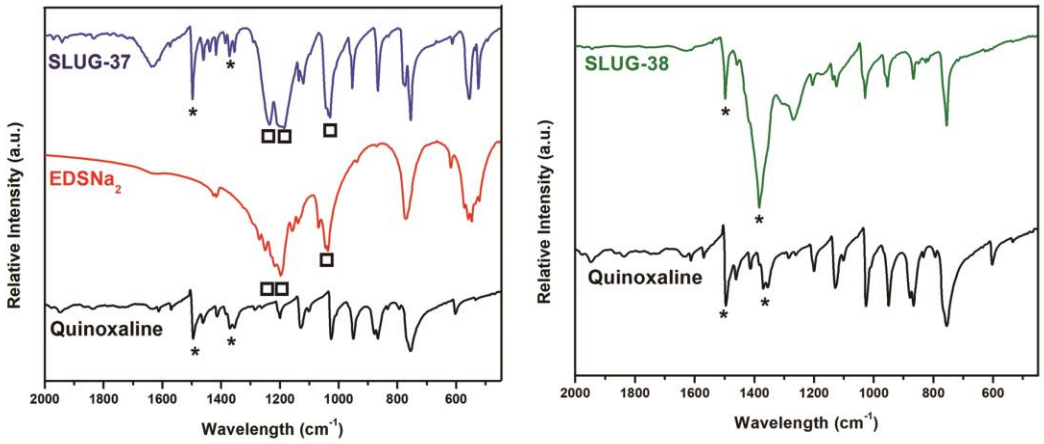

Figure 3.5. FTIR spectra of SLUG-37 (blue, left) and SLUG-38 (green, right). $EDSNa_2$ (red, left) stands for 1,2-ethanedisulfonate disodium salt and quinox (black) stands for quinoxaline. Sulfonate stretches are denoted by ◘ and C=N and C=C stretches of quinoxaline are denoted by *.

The FTIR spectra display characteristic absorption bands for the quinoxaline linker for both SLUG-n materials (Figure 5). The absorption bands with variable intensity in the frequency range 1400 to 1600 cm^{-1} are attributed to the C=N and C=C groups of the quinoxaline ligand. In SLUG-37, the strong bands at ~ 1232, 1210 and 1042 cm^{-1} are assigned to the sulfonate stretches of the interlamellar EDS molecules. These bands appear at lower wavenumbers than the vibrational frequencies of the free ligand, supporting the coordination of quinoxaline and EDS to the Ag centers.

In-situ VT-PXRD and TGA were used to investigate phase transitions and thermal decomposition. For VT-PXRD, the two distinct low angle peaks of SLUG-37 [9° to 10° (2θ), Figure 6a] vanished at 75°C. The TGA trace (Figure 7) showed 3.09% weight loss in this region, which we attribute to the partial loss of free water molecules (calculated: 4.90%). Another weight loss in the TGA between 90 and 98

°C corresponds to interlamellar water (calculated: 9.78%, observed: 8.97%). At the higher temperature of 125 to 175 °C, a new crystalline phase with first peak around 14° (2θ) appeared. In the TGA traces, the corresponding weight loss of 34.1% between 175 and 225 °C is likely due to decomposition of the free, uncoordinated quinoxalines (observed 32.1%, expected 35.4%), which can also be seen in the luminescence studies (*vide infra*). The weight loss of 25.8% around 380 °C in the TGA traces is attributed to the partial loss of methyl sulfonate from interlamellar EDS (calculated 26.1%). According to the VT-PXRD patterns (Figure 6a), silver(II) sulfate (ICDD #01-078-9487) forms between 225 and 350 ºC . At 400°C, new peaks begin to form and are indicative of silver oxide (39.8° and 43.1° 2θ, ICDD #00-019-1155 and #01-074-0878) and silver metal (44.3° and 64.4° 2θ, ICDD #01-087-0719).

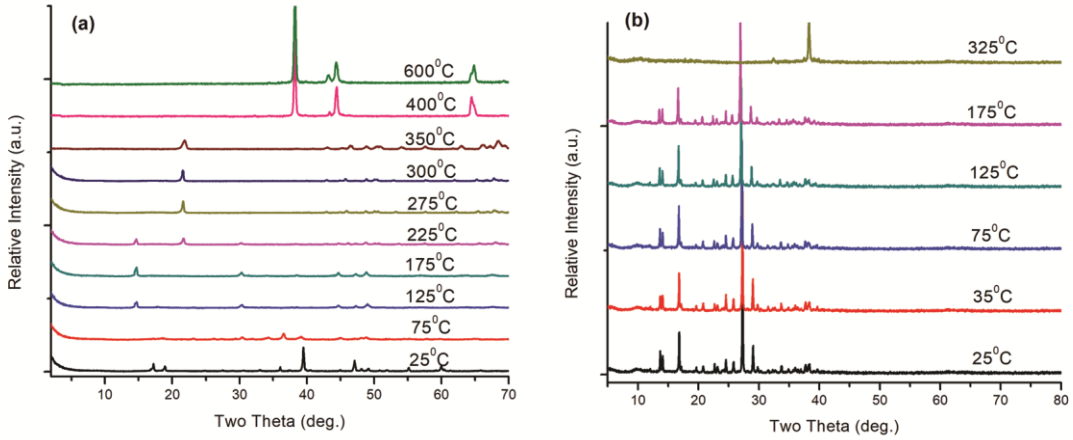

Figure 3.6. VT-PXRD of SLUG-37 (a) and SLUG-38 (b).

The TGA and VT-PXRD of SLUG-38 (Figure 6b and 7, respectively) display much simpler thermal behavior. The material shows no initial weight loss since in

this case there are no occluded water molecules. The material decomposes at *ca*. 230 ^{o}C, presumably due to the weaker hydrogen bonding between the acetate molecules and coordination polymers. Both the intra-framework quinoxaline ligands and acetates are lost in this step (58.5% observed, 58.3% calculated). At 325 °C, SLUG-38 transformed into silver oxide (32.4° and, 37.5° 2θ, ICDD #01-078-5867) and silver metal (38.3° 2θ, ICDD #01-071-4612) (Figure 6b).

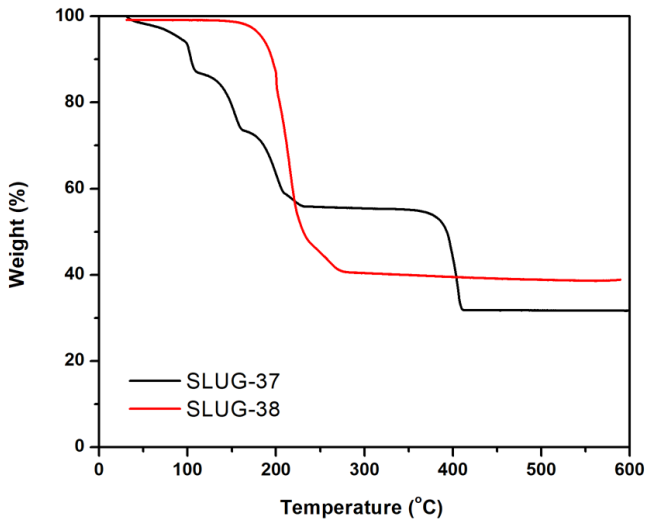

Figure 3.7. TGA traces of SLUG-37 (black) and SLUG-38 (red) under N_2 purge in the range of 30 to 600 ^{o}C.

3.3.2. Luminescent studies

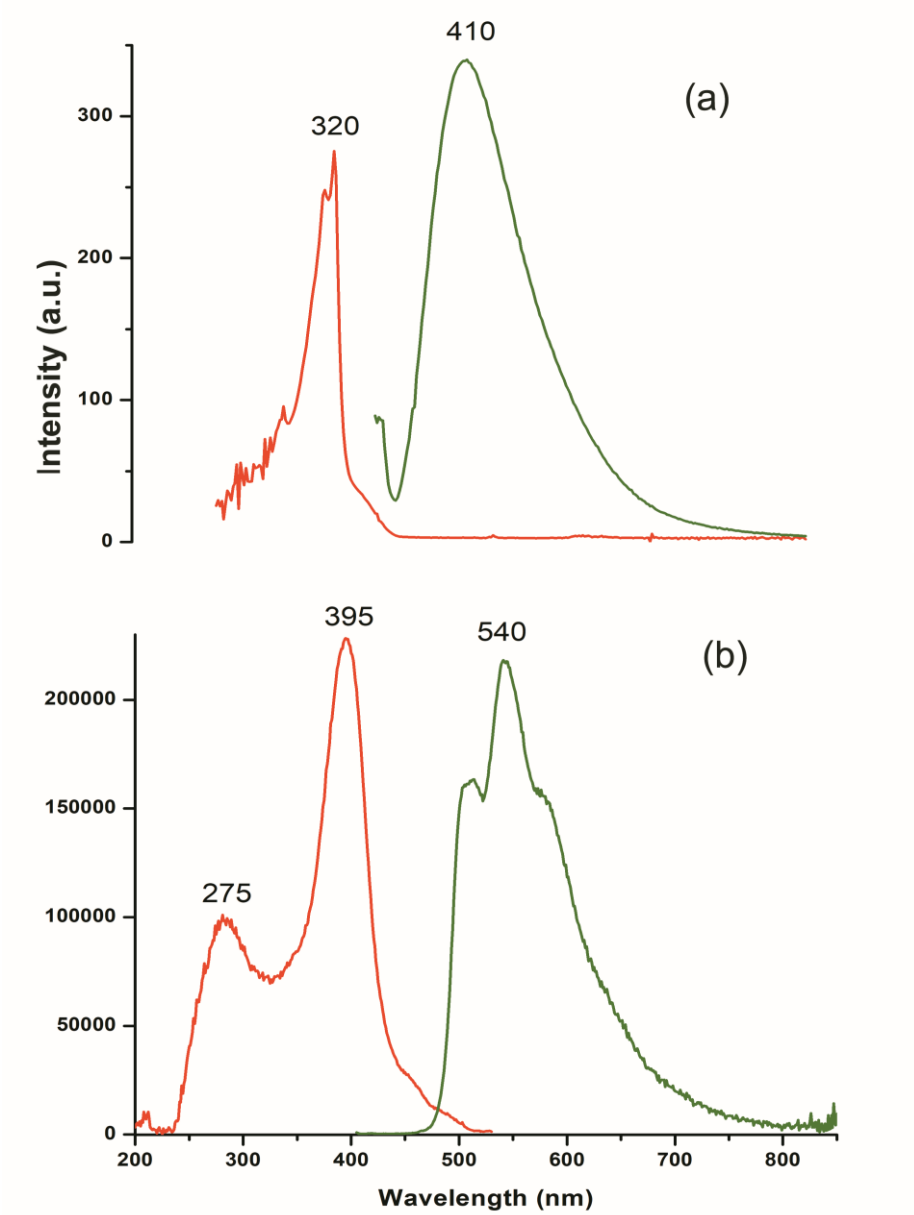

Figure 3.8: Excitation spectrum monitoring the emission at 540 nm (red line, left) and emission spectrum with excitation at 395 nm (green line, right) for SLUG-37.

Luminescence of SLUG-37 was studied in the solid state at room temperature whereas the ligand was measured in acetonitrile due to its hygroscopic property (Figure 8a). SLUG-37 displays two excitation wavelengths at 275 and 395 nm (Figure 8b). Upon maximum excitation at 395 nm, SLUG-37 emits with a red-shifted maximum at 540 nm. Considering that free quinoxaline gives a strong emission at 410 nm (Figure 8a), the main emission of SLUG-37 is assigned to metal-to-ligand charge transfer (MLCT). The ligand has a robust π-conjugated system of quinoxaline ring and uses nitrogen donors to coordinate to Ag(I), which benefits the charge transfer between Ag(I) ion and quinoxaline. The higher energy, weaker emission around 500 nm is presumably due to the free quinoxaline molecules of crystallization residing in the framework that were observed by TGA [16]. The efficient luminescence for this material is likely due to the greater quinoxaline alignment in the π-stacked adjacent chains compared to neat quinoxaline. The emission color is close to white light, which is of much importance for potential application and have rarely been observed for coordination complexes[38]. Because the excitation band also matches well to commercially used UV light-emitted diodes (LEDs), the material may be potentially useful for white LED applications[39]. Without EDS bridging and weaker π–π stacking interaction, SLUG-38 did not perform well towards emission and was therefore not included.

4.3. Conclusions and Remarks

Two Ag-based cationic materials were synthesized by a one-step synthetic method, with high yield and phase purity. The Ag-quinoxaline layers of SLUG-37 are both bridged and charge-balanced by EDS while those of SLUG-38 are only charge-balanced by the acetate anions. Both SLUG-n materials exhibit good thermal stability by VT-PXRD and TGA with transformation to silver sulfate and oxide at higher temperature. White light emitting SLUG-37 displays efficient photoluminescence at 540 nm. While the strong bonding of these materials prevents anion intercalation/exchange, they are an important step in the discovery of cationic extended frameworks where the linker is varied from the typical 4,4'-bipyridine of our other structures. We are currently working on other N-donor ligands for variation in structure type and in turn properties.

4.3. References

(1) Batten, S. R.; Champness, N. R.; Chen, X.-M.; Garcia-Martinez, J.; Kitagawa, S.; Öhrström, L.; O'Keeffe, M.; Paik Suh, M.; Reedijk, J. Terminology of Metal–Organic Frameworks and Coordination Polymers (IUPAC Recommendations 2013). *Pure Appl. Chem.* **2013**, *85* (8), 1715–1724. https://doi.org/10.1351/PAC-REC-12-11-20.

(2) J. Oliver, S. R. Cationic Inorganic Materials for Anionic Pollutant Trapping and Catalysis. *Chem. Soc. Rev.* **2009**, *38* (7), 1868–1881. https://doi.org/10.1039/B710339P.

(3) Tran, D. T.; Zavalij, P. Y.; Oliver, S. R. J. Pb3F5NO3, a Cationic Layered Material for Anion-Exchange. *J. Am. Chem. Soc.* **2002**, *124* (15), 3966–3969. https://doi.org/10.1021/ja017333w.

(4) Sheng, D.; Zhu, L.; Xu, C.; Xiao, C.; Wang, Y.; Wang, Y.; Chen, L.; Diwu, J.; Chen, J.; Chai, Z.; et al. Efficient and Selective Uptake of TcO4– by a Cationic Metal–Organic Framework Material with Open Ag+ Sites. *Environ. Sci. Technol.* **2017**, *51* (6), 3471–3479. https://doi.org/10.1021/acs.est.7b00339.

(5) Zhu, L.; Sheng, D.; Xu, C.; Dai, X.; Silver, M. A.; Li, J.; Li, P.; Wang, Y.; Wang, Y.; Chen, L.; et al. Identifying the Recognition Site for Selective Trapping of 99TcO4– in a Hydrolytically Stable and Radiation Resistant Cationic Metal–Organic Framework. *J. Am. Chem. Soc.* **2017**, *139* (42), 14873–14876. https://doi.org/10.1021/jacs.7b08632.

(6) Li, Y.; Yang, Z.; Wang, Y.; Bai, Z.; Zheng, T.; Dai, X.; Liu, S.; Gui, D.; Liu, W.; Chen, M.; et al. A Mesoporous Cationic Thorium-Organic Framework That Rapidly Traps Anionic Persistent Organic Pollutants. *Nat. Commun.* **2017**, *8* (1). https://doi.org/10.1038/s41467-017-01208-w.

(7) Khlobystov, A. N.; Blake, A. J.; Champness, N. R.; Lemenovskii, D. A.; Majouga, A. G.; Zyk, N. V.; Schröder, M. Supramolecular Design of One-Dimensional Coordination Polymers Based on Silver(I) Complexes of Aromatic Nitrogen-Donor Ligands. *Coord. Chem. Rev.* **2001**, *222* (1), 155–192. https://doi.org/10.1016/S0010-8545(01)00370-8.

(8) Zheng, S.-L.; Tong, M.-L.; Chen, X.-M. Silver(I)–Hexamethylenetetramine Molecular Architectures: From Self-Assembly to Designed Assembly. *Coord. Chem. Rev.* **2003**, *246* (1–2), 185–202. https://doi.org/10.1016/S0010-8545(03)00116-4.

(9) Hong, M.-C.; Chen, L. Design and Construction of Coordination Polymers. In *Design and Construction of Coordination Polymers*; John Wiley & Sons, Inc.: New Jersey, 2009; pp 111–144.

(10) Kim, H.-J.; Zin, W.-C.; Lee, M. Anion-Directed Self-Assembly of Coordination Polymer into Tunable Secondary Structure. *J. Am. Chem. Soc.* **2004**, *126* (22), 7009–7014. https://doi.org/10.1021/ja049799v.

(11) Seeber, G.; Pickering, A. L.; Long, D.-L.; Cronin, L. Controlling Dimensionality of Silver(I) Coordination Networks with Rigid Aliphatic Amino Ligands: From a 2D to a 3D Network of Unprecedented Topology

Comprising Helical Channels. *Chem. Commun.* **2003**, *0* (16), 2002–2003. https://doi.org/10.1039/B305188A.

(12) Dolomanov, O. V.; Cordes, D. B.; Champness, N. R.; Blake, A. J.; Hanton, L. R.; Jameson, G. B.; Schröder, M.; Wilson, C. A Design Strategy for Four-Connected Coordination Frameworks. *Chem. Commun.* **2004**, *0* (6), 642–643. https://doi.org/10.1039/B315243J.

(13) Carlucci, L.; Ciani, G.; Proserpio, D. M.; Sironi, A. Novel Networks of Unusually Coordinated Silver(I) Cations: The Wafer-Like Structure of [Ag(Pyz)2][Ag2(Pyz)5](PF6)3·2G and the Simple Cubic Frame of [Ag(Pyz)3](SbF6). *Angew. Chem. Int. Ed.* **1995**, *34* (17), 1895–1898. https://doi.org/10.1002/anie.199518951.

(14) Tsuda, T.; Ohba, S.; Takahashi, M.; Ito, M. Structures of 1,8-Naphthyridine Silver(I) Perchlorate, Quinoxaline Silver(I) Perchlorate and Phthalazine Silver(I) Nitrate. *Acta Crystallogr. C* **1989**, *45* (6), 887–890. https://doi.org/10.1107/S0108270188014507.

(15) M. Abu-Youssef, M. A.; Langer, V.; Öhrström, L. Synthesis, a Case of Isostructural Packing, and Antimicrobial Activity of Silver(I)Quinoxaline Nitrate, Silver(I)(2,5-Dimethylpyrazine) Nitrate and Two Related Silver Aminopyridine Compounds. *Dalton Trans.* **2006**, *0* (21), 2542–2550. https://doi.org/10.1039/B516723J.

(16) Kokunov, Y. V.; Gorbunova, Y. E.; Kovalev, V. V.; Kozyukhin, S. A. Coordination Polymer of Silver(I) Perrhenate with Quinoxaline: Synthesis,

Crystal Structure, and Luminescence Properties. *Russ. J. Coord. Chem.* **2015**, *41* (11), 747–750. https://doi.org/10.1134/S1070328415110032.

(17) Côté, A. P.; Shimizu, G. K. H. The Supramolecular Chemistry of the Sulfonate Group in Extended Solids. *Coord. Chem. Rev.* **2003**, *245* (1–2), 49–64. https://doi.org/10.1016/S0010-8545(03)00033-X.

(18) Charbonnier, F.; Faure, R.; Loiseleur, H. Structure cristalline de l'éthanedisullonate-1,2 de cuivre tétrahydraté: Cu[SO3(CH2)2SO3].4H2O. *Acta Crystallogr. B* **1977**, *33* (11), 3342–3345. https://doi.org/10.1107/S0567740877010966.

(19) Fei, H.; Oliver, S. R. J. Copper Hydroxide Ethanedisulfonate: A Cationic Inorganic Layered Material for High-Capacity Anion Exchange. *Angew. Chem. Int. Ed.* **2011**, *50* (39), 9066–9070. https://doi.org/10.1002/anie.201104200.

(20) Forster, P. M.; Tafoya, M. M.; Cheetham, A. K. Synthesis and Characterization of Co7(OH)12(C2H4S2O6)(H2O)2—a Single Crystal Structural Study of a Ferrimagnetic Layered Cobalt Hydroxide. *J. Phys. Chem. Solids* **2004**, *65* (1), 11–16. https://doi.org/10.1016/j.jpcs.2003.08.016.

(21) Rogow, D. L.; Zapeda, G.; Swanson, C. H.; Fan, X.; Oliver, A. G.; Oliver, S. R. J. A Metal−Organic Framework Containing Cationic Inorganic Layers: Pb2F2[C2H4(SO3)2]. *Chem. Mater.* **2007**, *19* (19), 4658–4662. https://doi.org/10.1021/cm071429t.

(22) Sergo, K. M.; Han, C. S.; Bresler, M. R.; Citrak, S. C.; Abdollahian, Y.; Fei, H.; Oliver, S. R. J. Erbium Hydroxide Ethanedisulfonate: A Cationic Layered

Material with Organic Anion Exchange Capability. *Inorg. Chem.* **2015**, *54* (8), 3883–3888. https://doi.org/10.1021/acs.inorgchem.5b00073.

(23) Maspoch, D.; Ruiz-Molina, D.; Veciana, J. Old Materials with New Tricks: Multifunctional Open-Framework Materials. *Chem. Soc. Rev.* **2007**, *36* (5), 770–818. https://doi.org/10.1039/B501600M.

(24) Suh, M. P.; Cheon, Y. E.; Lee, E. Y. Syntheses and Functions of Porous Metallosupramolecular Networks. *Coord. Chem. Rev.* **2008**, *252* (8–9), 1007–1026. https://doi.org/10.1016/j.ccr.2008.01.032.

(25) Cui, Y.; Yue, Y.; Qian, G.; Chen, B. Luminescent Functional Metal–Organic Frameworks. *Chem. Rev.* **2012**, *112* (2), 1126–1162. https://doi.org/10.1021/cr200101d.

(26) Hu, Z.; Deibert, B. J.; Li, J. Luminescent Metal–Organic Frameworks for Chemical Sensing and Explosive Detection. *Chem. Soc. Rev.* **2014**, *43* (16), 5815–5840. https://doi.org/10.1039/C4CS00010B.

(27) Allendorf, M. D.; Bauer, C. A.; Bhakta, R. K.; Houk, R. J. T. Luminescent Metal–Organic Frameworks. *Chem. Soc. Rev.* **2009**, *38* (5), 1330–1352. https://doi.org/10.1039/B802352M.

(28) Hadley, S. G. Intersystem Crossing Quantum Yield of Quinoxaline; Evidence for High Yield of Internal Conversion of the First Excited Singlet State to the Ground State. *Chem. Phys. Lett.* **1970**, *6* (5), 549–550. https://doi.org/10.1016/0009-2614(70)85219-8.

(29) Etaiw, S. E. H.; El-bendary, M. M.; Fouda, A. E.-A. S.; Maher, M. Synthesis and Structure Characterizations of Coordination Polymers Based on Silver(I) and Nitrogen Donors. *J. Inorg. Organomet. Polym. Mater.* **2014**, *25* (4), 702–711. https://doi.org/10.1007/s10904-014-0148-3.

(30) North, A. C. T.; Phillips, D. C.; Mathews, F. S. Lorentz-Polarization and Adsorption. *Acta Crystallogr. C* **1968**, *24*, 351.

(31) Sheldrick, G. M. Integrated Space-Group and Crystal-Structure Determination. *Acta Crystallogr. Sect. Found. Adv.* **2015**, *71* (1), 3–8. https://doi.org/10.1107/S2053273314026370.

(32) Sheldrick, G. M. *Bruker Analytical X-Ray Systems*; SHELXTRL; Madison, Winsconsin, USA, 2000.

(33) Dolomanov, O. V.; Bourhis, L. J.; Gildea, R. J.; Howard, J. A. K.; Puschmann, H. OLEX2: A Complete Structure Solution, Refinement and Analysis Program. *J. Appl. Crystallogr.* **2009**, *42* (2), 339–341. https://doi.org/10.1107/S0021889808042726.

(34) Janiak, C. A Critical Account on π–π Stacking in Metal Complexes with Aromatic Nitrogen-Containing Ligands. *J. Chem. Soc. Dalton Trans.* **2000**, *0* (21), 3885–3896. https://doi.org/10.1039/B003010O.

(35) Côté, A. P.; Ferguson, M. J.; Khan, K. A.; Enright, G. D.; Kulynych, A. D.; Dalrymple, S. A.; Shimizu, G. K. H. Intercalation of Alcohols in Ag Sulfonates: Topotactic Behavior Despite Flexible Layers. *Inorg. Chem.* **2002**, *41* (2), 287–292. https://doi.org/10.1021/ic010800q.

(36) Ning, G. L.; Wu, L. P.; Sugimoto, K.; Munakata, M.; Kuroda-Sowa, T.; Maekawa, M. Construction of 2-D Multilayer Structures: Silver(I) Complexes with Linear Aromatic Compounds. *J. Chem. Soc. Dalton Trans.* **1999**, No. 15, 2529–2536. https://doi.org/10.1039/A902692D.

(37) R. Desiraju, G. Strength and Linearity of C–H ⋯ O Bonds in Molecular Crystals: A Database Study of Some Terminal Alkynes. *J. Chem. Soc. Chem. Commun.* **1990**, *0* (6), 454–455. https://doi.org/10.1039/C39900000454.

(38) Wang, M.-S.; Guo, S.-P.; Li, Y.; Cai, L.-Z.; Zou, J.-P.; Xu, G.; Zhou, W.-W.; Zheng, F.-K.; Guo, G.-C. A Direct White-Light-Emitting Metal-Organic Framework with Tunable Yellow-to-White Photoluminescence by Variation of Excitation Light. *J. Am. Chem. Soc.* **2009**, *131* (38), 13572–13573. https://doi.org/10.1021/ja903947b.

(39) Ki, W.; Li, J. A Semiconductor Bulk Material That Emits Direct White Light https://pubs.acs.org/doi/abs/10.1021/ja801601y (accessed Jun 15, 2018). https://doi.org/10.1021/ja801601y.

Chapter (4)

Copper-Bipyridine Coordination Polymers for Water Remediation by Anion Exchange

Abstract

The copper-based coordination polymer (CBN) [Cu(4,4'-bipy)$_{1.5}$•NO_3(H_2O)$_{1.25}$] was investigated for its anion exchange properties. The structure crystallizes in high symmetry orthorhombic crystal system and contains a 3D interpenetrating framework with charge-balancing nitrate anions between adjacent chains. The problematic anion pollutants such as pharmaceuticals and their metabolites and oxo-anions (e.g. chromate, perrhenate) were used to study the anion exchange in aqueous solution. The adsorption capacity for chromate was 242 mg/g, which was far higher than other recent reported cationic materials from our group such as SLUG-21 and SLUG-35. Considering the openness of the structure, CBN was able to perform anion exchange with a series of α,ω-alkanedicarboxylates.

4.1. Introduction

4.1.1. Copper-Bipyridine Coordination Polymers

In the past decades, transition metal coordination polymers have gained attention for their ability to direct certain frameworks and building blocks[1,2] as well as their ion exchange properties.[3–8] These layered materials allow for different arrangements of the polymeric layers depending on the nature of the charge balancing anion, as well as tunability in anion exchange with regards to the size/shape of the

intercalating and de-intercalating anions. In 2010, our group reported a copper-based coordination polymer, SLUG-22, with structural flexibility for reversible anion exchange.[7] The material is a cationic 1D polymer consisting of 4,4′-bipyridine (bipy) organic linker and 1,2-ethanedisulfonate (EDS), as an organic template. SLUG-22 possesses weak electrostatic interaction between the interlamellar anion, in this case EDS, and cationic coordination layers. Two different organic linkers support Cu(I) with enough openness to allow access by incoming guests, displaying reversible anion exchange between organosulfonate and various inorganic species. The Cu-bipy chains are arranged into closed-packed layers by π-π stacking between adjacent 1D cationic layers (Figure 4.1).

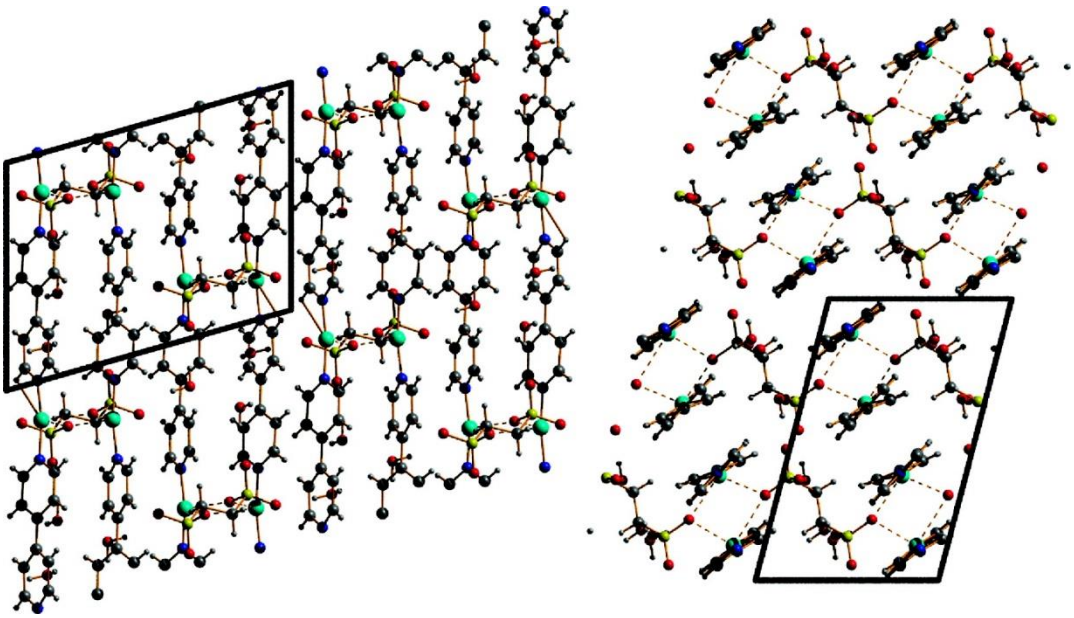

Figure 4.1: Crystallographic *a*-projection (left) and *b*-projection (right) of SLUG-22.[7]

SLUG-22 displayed anion exchange with nitrate and perchlorate whereas perchlorate could exchange with complete reversibility for EDS.

The organosulfonate linker is neither an environmentally friendly anion nor cost-effective for water remediation towards a sustainable ecosystem. Hence, the silver-bipyridine-nitrate (SBN) coordination polymer using nitrate as its counter anion, was introduced as a perchlorate trapping material with record capacity, selectivity, and reversibility.[9] Because nitrate could use it as nutrient for farms that can be readily absorbed by plants at high rate and concentration up to 100 mM.[10] SBN [$Ag(bipy)^{+}(NO_3)^{-}$] was able to successfully exchange harmful oxo-anions such as perchlorate at 354 mg/g and 99% removal within 90 mins. The kinetics of perchlorate uptake by SBN were analyzed and compared to the performance of the commercially available anion exchange resins Amberlite IRA-400 and Purolite A530E, as well as the calcined and uncalcined forms of hydrotalcite, $Mg_6Al_2(CO_3)(OH)_{16}\cdot 4H_2O$ and Ni_3Al-layered double hydroxide. In addition to SBN, our group is interested in ion exchange study for copper-bipyridine-nitrate (CBN) coordination polymers which was first introduced in 1995.[11] CBN was investigated for uptake of the oxo-anion pollutant ReO_4^- and alkanecarboxylates as analogs for pharmaceutical waste.

4.1.2. Oxo-anion Pollutants and Organic Contaminants

Many of the priority pollutants in wastewater listed by the U.S. Environmental Protection Agency (EPA) are oxo-anionic forms, for example, pertechnetate (TcO_4^-), chromate (CrO_4^{2-}) and perchlorate (ClO_4^-).[12] These toxic and harmful anions are problematic in the vitrification of low activity radioactive waste, weakening the integrity of the waste glass by forming spinels.[13] Another class of water-borne toxic anion pollutants are organic, generated through both industrial and personal use. EPA classifies many of these wastes as pharmaceutical and personal care products (PPCPs).[14] Many pharmaceuticals are sold in their acid forms and consequently form anions when dissolved in water. Some of them contain dicarboxylate segements and an analog are the α,ω-alkanedicarboxylates. Pharmaceuticals and their metabolites are a rising problem in wastewater streams and more recently drinking water supplies since water treatment plants cannot entirely remove them. Current conventional treatment processes based on activated carbon and commercial resins do not sufficiently remove these species and are not cost-effective. One alternative studied to possibly replace resins is layered double hydroxides (LDHs), an isostructural group of materials containing cationic brucite type layers that are charged balanced by interlayer anions with general formula $[M^{2+}_{1-x}M^{3+}_{x}(OH)_2](A^{n-}_{x/n})\cdot xH_2O$ [M^{2+} and M^{3+} are a range of metals (e.g. Mg^{2+}/Al^{3+}), A^{n-} is *n*-valent intercalated anion (e.g. CO_3^{2-}), and x is ratio of $M^{3+}/(M^{2+} + M^{3+})$]. However, the target anions cannot be selectively removed and common anions will re-intercalate, such as carbonate or sulfate due to the memory effect.[15,16] Owing to the structural diversities and weak

host-guest interactions, cationic coordination polymers are gaining considerable attention for anion exchange. The flexibility of coordination polymers, and the apparent selectivity for a variety of toxic oxo-anions,[12,17] provides great potential for these materials to be used as a water remediation tool.

Herein we reported anion exchange study of a copper-bipyridine-nitrate coordination polymer. We characterize the material and quantify the exchanges by PXRD, FTIR, TGA and UV-Vis.

4.2. Experimental

4.2.1. Reagents

Copper nitrate ($CuNO_3$•$2.5H_2O$, Alfa Aesar, 99%) and 4,4'-bipyridine [$(C_5H_4N)_2$, Acros Organics, 98%] were used as received for the synthesis. For the exchange studies, the following were used as-purchased: sodium perrhenate ($NaReO_4$, Fisher Chemical, 99+%), disodium malonate ($[^-O_2C\text{-}CH_2\text{-}CO_2^-]Na^{2+}$, TCI America), disodium succinate ($[^-O_2C\text{-}(CH_2)_2\text{-}CO_2^-]Na^{2+}$, TCI America), disodium glutarate ($[^-O_2C\text{-}(CH_2)_3\text{-}CO_2^-]Na^{2+}$, TCI America), adipic acid ($[^-O_2C\text{-}(CH_2)_6\text{-}CO_2^-]Na^{2+}$, TCI America) and disodium sebacate ($[^-O_2C\text{-}(CH_2)_8\text{-}CO_2^-]Na^{2+}$, TCI America).

4.2.2. Synthesis of CBN $[Cu(4,4'\text{-bipy})_{1.5}\bullet NO_3(H_2O)_{1.25}]$

A mixture of $Cu(NO_3)_2.2.5H_2O$ (0.17 g, 0.74 mmol), 4,4'-bipy (0.17 g, 1.11 mmol), and 1,3,5-triazine (0.040 g, 0.49 mmol) in 10 mL of deionized water was transferred to a stainless-steel bomb, which was sealed and placed in a programmable oven. The temperature was raised to 140 °C at 5 deg/min and held at that temperature

for 24 h, then cooled at 0.1 deg/min to 90 °C and held for 12 h, then cooled at the same rate to 70 °C and held for another 12 h, and finally cooled down to room temperature at 0.1 deg/min. The resulting rectangular parallelepiped orange crystals of $Cu(4,4'\text{-bipy})_{1.5} \cdot NO_3(H_2O)_{1.25}$ were collected and rinsed with Millipore water and acetone and then air dried to give 0.22 g (86.9% yield based on bipy).

4.2.3. Anion Exchange Procedure

Anion Exchange: Batch experiments for anion exchange were conducted at ambient pressure and temperature. The exchange reactions were performed by placing CBN (0.1 mmol) and the anion of interest (0.1 mmol) in 50 mL of Millipore water. The resulting systems were kept under magnetic stirring at room temperature for 24 h. Molar fractions were varied according to the charge of the incoming anion. Equimolar quantities were used for all anion exchanges. The post-exchange product was recovered by vacuum filtration and rinsed with water and acetone prior analysis by powder X-ray diffraction (PXRD). CBN regeneration from chromate exchange: 0.24 M of CBN-chromate exchange product was placed into 20 molar excess of $NaNO_3$ solution and stirred at room temperature for 4 days. The regeneration was evaluated by PXRD and UV-vis.

4.2.4. Instrumental Details for Characterization

PXRD data were obtained on a Rigaku Americas Miniflex Plus powder diffractometer, scanning from 2° to 40° (2θ) at a rate of $3°\bullet min^{-1}$ with a 0.02° step size under Cu-Kα radiation (λ = 1.5418 Å). SEM images were collected with a FEI

Quanta 3D Dualbeam microscope. Fourier Transform Infrared (FT-IR) data was collected on a Perkin Elmer, Spectrum One FT-IR spectrometer. Thermogravimetric analysis (TGA) was performed using a TA Instruments 2050 TGA by heating from 25 to 600 °C with a gradient of 10 °C/min and nitrogen flow. UV-vis analysis was performed to assess chromate concentration using a Hewlett-Packard model 8452A. UV-Vis spectrophotometer. Standard curves for chromate were prepared for all UV-Vis experiments to quantify the concentration of the samples.

4.3. Result and Discussion

4.3.1. Synthesis and Structure properties

The parallelepiped orange crystals were synthesized under hydrothermal synthesis, and their structure confirmed by the match of the experimental PXRD pattern to the theoretical pattern simulated from single-crystal data from the literature (Figure 4.2).[11] CBN crystallizes in a high symmetry F*ddd*-D_{2h} space group of the orthorhombic crystal system. The structure is a network with charge balancing nitrate anions between cationic Cu-bipy layers. Slightly distorted trigonal planar Cu(I) centers are linked by rod-like bipy ligands to form porous interpenetrated networks (Figure 4.3). The crystallographic view from the structure showed disordered nitrate ions, indicating that they are loosely bound to the framework. In this case, it is suitable for anion exchange studies in pH 7 aqueous media. Attempts to prepare this compound outside the autoclave by using the same reaction in water at room

temperature or by refluxing for 24 h did not succeed. It appears that hydrothermal conditions are essential for dissolving 4,4'-bipy and achieving the final product.

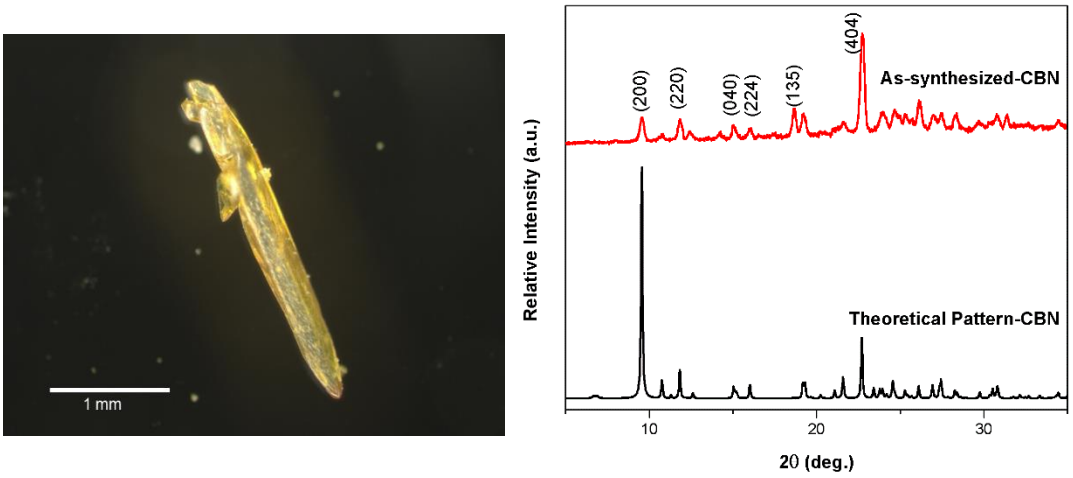

Figure 4.2: (Left) Optical image of CBN. Scale bar is at 1 mm; (Right) PXRD pattern of CBN.

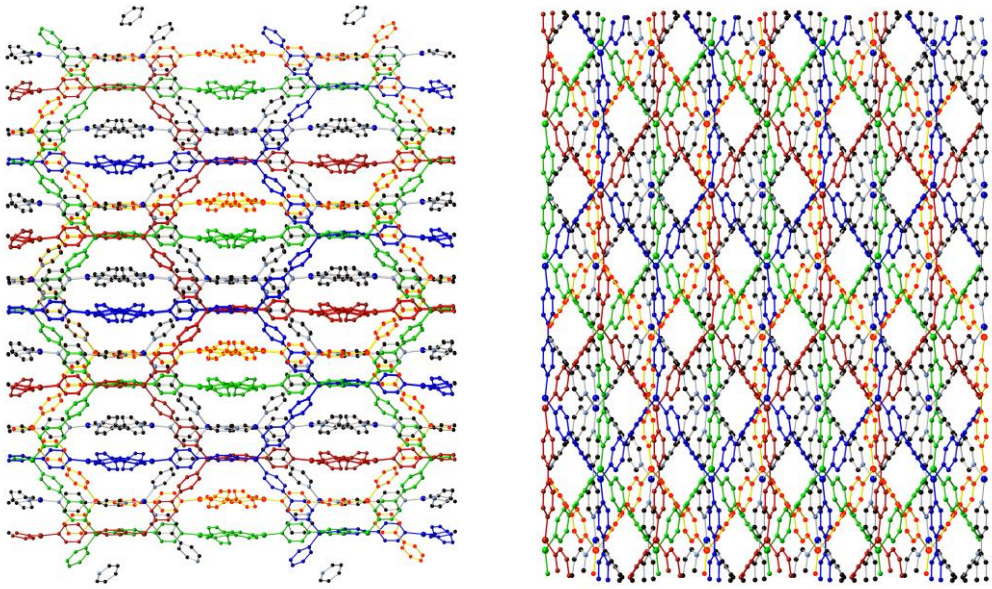

Figure 4.3: 3D view of six-fold interpenetrated CBN (left) and packing along *c* view (right).

The thermal stability of CBN was investigated by TGA under a N_2 purge (Figure 4.4). The TGA trace of CBN indicated a slight loss of 6% at 90-100 °C, likely due to the loss of water 1.25 H_2O per formula unit (calculated: 6.1%, observed: 6.4%). The second weight loss likely corresponds to nitrate ions (calculated: 19.8%, observed: 19.3%). CBN is stable up to *ca.* 250 °C until the 4,4'-bipy ligands in the structure start to decompose, with a major weight loss (observed: 57%, calculated: 61%). The remaining loss might lead to metallic copper that is similar weight loss at the end of TGA of SLUG 22.[7]

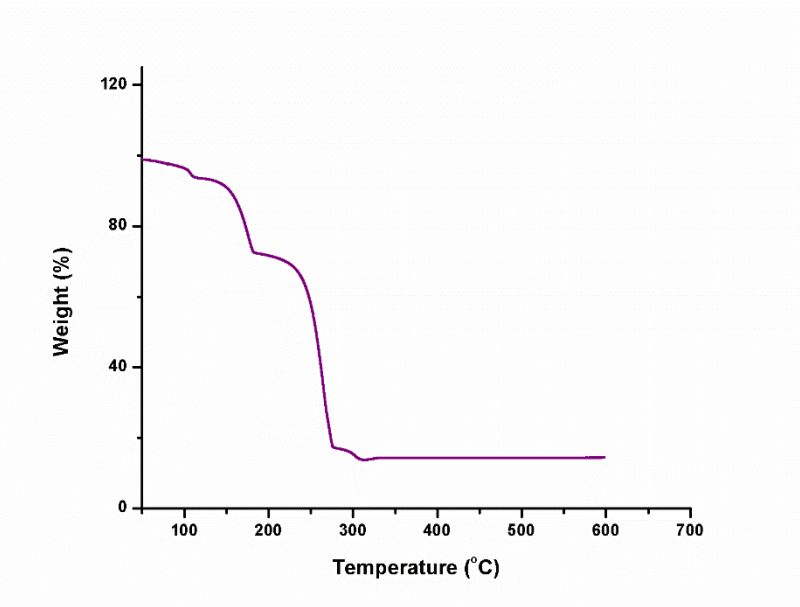

Figure 4.4: TGA trace of CBN.

4.3.2. Anion Exchange Results

Considering that CBN has weakly bound anions between cationic Cu-bipy layers, we studied anion exchange for various α,ω-alkanedicarboxylates and chose perrhenate and chromate as initial examples of oxo-anion pollutants. The anion exchange proceeds under ambient conditions by simply placing CBN into the equal molar ratio of anion solution with mild stirring.

Chromate (CrO_4^{2-}) Exchange: The chromate uptake was monitored by UV-Vis spectroscopy over 20 h. The characteristic absorption peaks of CrO_4^{2-} (372 nm) significantly decreased for 2.75 h and reached equilibrium after 20 h (Figure 4.5). After 2.75 h of exchange, the adsorption capacity of CrO_4^{2-} based on CBN was 230 mg/g (0.45 mol/mol) and for 20 h, the uptake was 242 mg/g (0.48 mol/mol). This

uptake capacity is higher than SLUG-21 (60 mg/g)[4], Zn-Co-SLUG-35 (68.5 mg/g),[6] Co-SLUG-35 (119 mg/g),[6] and ZIF-67 (13.34 mg/g).[18] In addition, the kinetic exchange rate of CBN is higher than Co-SLUG-35 and SLUG-21, however is a lower rate than ZIF-67

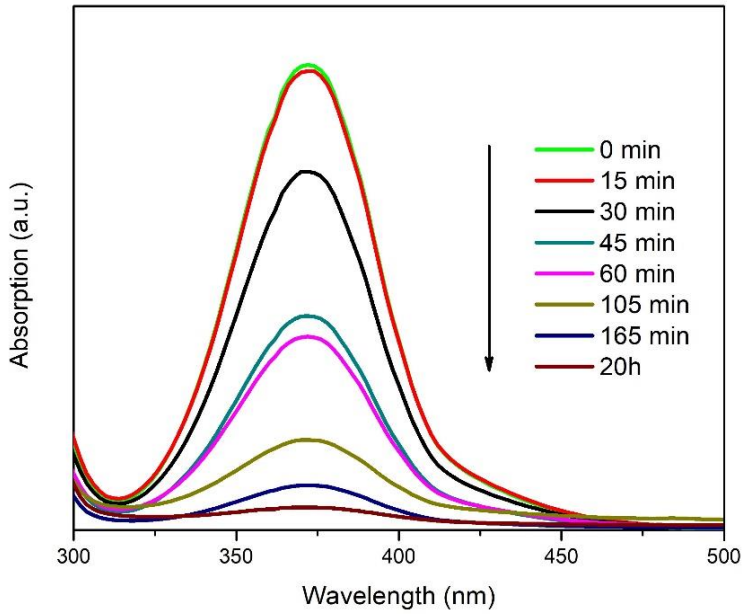

Figure 4.5: UV-Vis absorption spectra of the chromate exchange solution (0.2 mM of CBN, 0.1 mM of chromate in 50 mL Millipore water) at various time intervals (λ_{max} = 372 nm).

The PXRD pattern for the exchange product is indeed different from as-synthesized CBN (Figures 4.6a, 4.6b). The rapid capture and high capacity are likely due to the stability of chromate in the resultant structure. Upon completion of chromate exchange, the solid CBN-chromate materials were strongly resided between Cu-bipy layers. Therefore, the reversibility attempts were not completely successful within 4

days. UV-Vis and PXRD were monitored for reversible exchange for CBN regeneration (Figures 4.6c, 4.7).

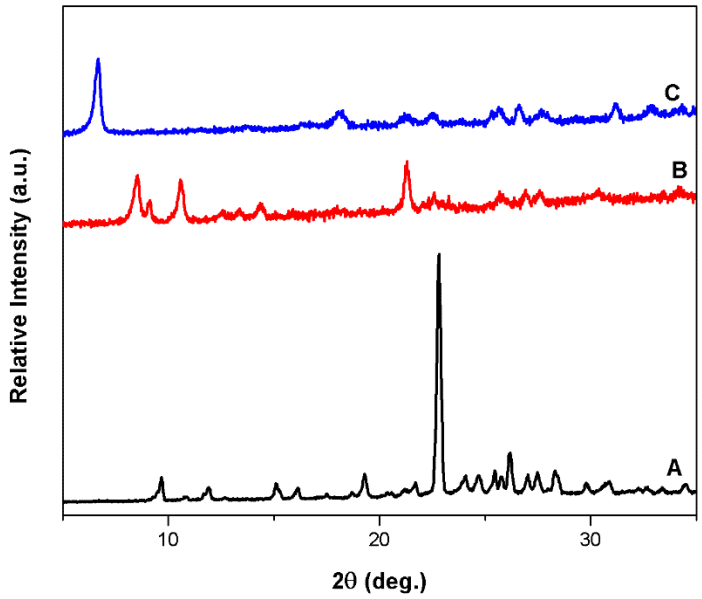

Figure 4.6: PXRD pattern of (a) CBN; (b) after exchange with chromate; (c) CBN regeneration from exchange.

According to the observed results for CBN-regeneration attempts, Hofmeister effects on selectivity might be a key contribution to anion separation. References to the Hofmeister effect most often mirror the order of decreasing anion hydration energy or charge density. Custelcean and co-workers reported the selectivity principles in anion separation using CPs and their solvent-mediated pathway.[19–21] Due to the lower hydration energy of nitrate (-314 kJ/mol) compared to chromate (-958 kJ/mol), the stability of the CBN-chromate structure is likely in fact higher, therefore, limiting the regeneration process.

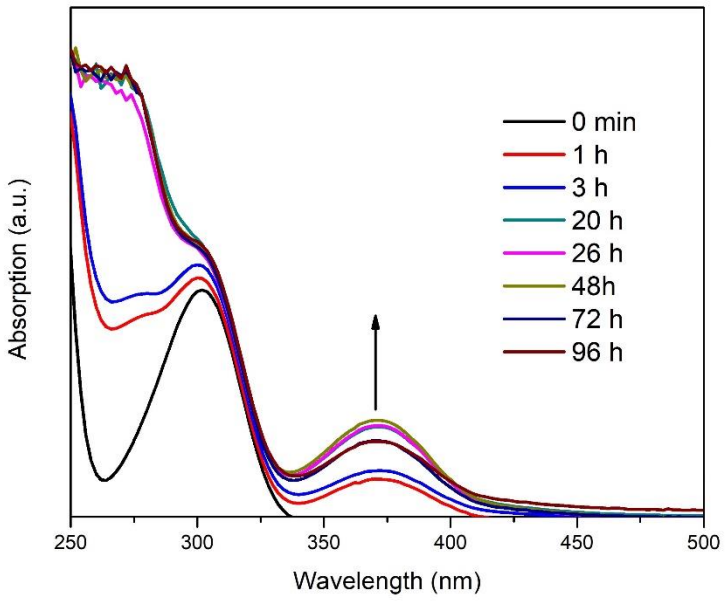

Figure 4.7: UV-vis absorption spectra of nitrate exchange solution for CBN regeneration (0.24 M of CBN-Chromate, 20 molar excess of $NaNO_3$ in 50 mL Millipore water) at various time intervals.

Perrhenate (ReO_4^-) and Tetrafluoroborate (BF_4^-) Exchange: For investigation of CBN for possible anion exchange of radioactive waste, ReO_4^- and BF_4^- were chosen as models for pertechnetate. An equal molar ratio of anion and CBN were placed into 50 mL aqueous solution at ambient condition for 24 h. As monitored by PXRD, the exchanges were not successful (Figure 4.8). It is probably due to the hydration energies difference in NO_3^- (-316 kJ/mol) vs. ReO_4^- (-240 kJ/mol) and BF_4^-(-268 kJ/mol). ReO_4^- and BF_4^- were not able to compete with higher hydration energy of nitrate from CBN. Besides, the low redox stability of Cu(I) might be a reason to the lack of these anions trapping.

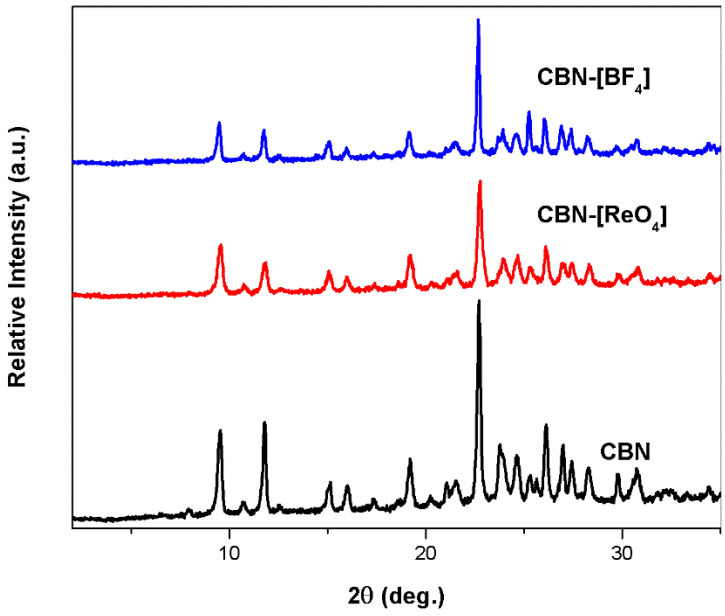

Figure 4.8: PXRD pattern of CBN exchanges with ReO_4^- and BF_4^-.

Various α,ω-alkanedicarboxylates Exchange: We also investigated anion exchange study with straight chain alkanedicarboxylates. Equimolar ratio of CBN and a series of carboxylate groups, [$^-O_2C(CH_2)_nCO_2^-$], malonate (n=1), succinate (n=2), glutarate (n=3), adipate (n=4), suberate (n=6), and sebacate (n=8) were mechanically stirred in aqueous solution for 24 h. The exchange results were investigated by PXRD, TGA and FT-IR.

The intact white microcrystalline powder solids and low 2θ angle PXRD diffraction peaks confirmed the exchange completeness (Figure 4.9). The principal peak of the as-synthesized nitrate-containing CBN is at 9.6° (2θ), corresponding to a layer-to-layer distance of 9.2 Å. As seen in Table 4.1, the relative carbon chain length and size of carbonate end groups [$^-O_2C(CH_2)_nCO_2^-$] was reported. It was anticipated

that malonate (n=1), succinate (n = 2), glutarate (n = 3), adipate (n = 4), suberate (n=6) and sebacate (n = 8) would shift the principal (200) peak to lower 2θ values as the interlayer distance increases.

Table 4.1: Principal PXRD peak (2θ and d-spacing values) for CBN and the dicarboxylate exchanged materials

Anions	2θ (degree)	d spacing (Å)
As synthesized	9.6	9.2
Malonate	7.1	12.4
Succinate	7.0	12.6
Glutarate	6.7	13.2
Adipate	9.0	9.8
Suberate	6.6	13.4
Sebacate	2.0	44.1

The intercalation of these dicarboxylate anions were successful and resulted an increase of *d*-spacing between Cu-bipy layers. The large *d* value is probably correlated to bilayer stacks of the sebacate. FTIR before and after exchange confirmed the anion exchange process, with the nitrate peak replaced by strong carboxylate stretches (1570 cm^{-1}, C=O) (Figure 4.10).

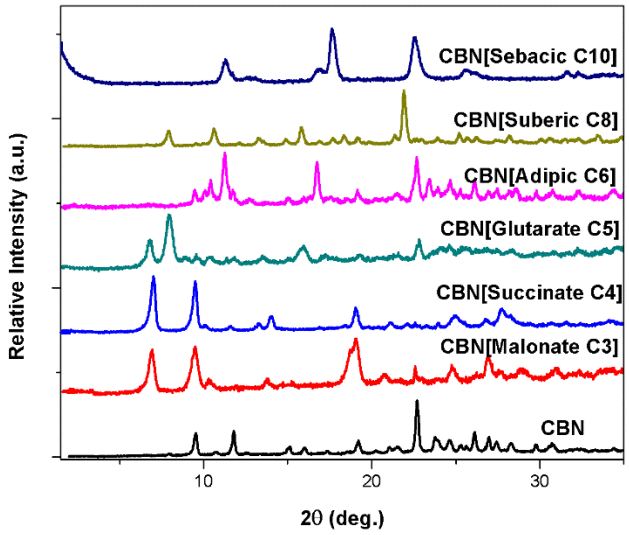

Figure 4.9: PXRD pattern of CBN exchanges with series of α,ω-alkanedicarboxylates.

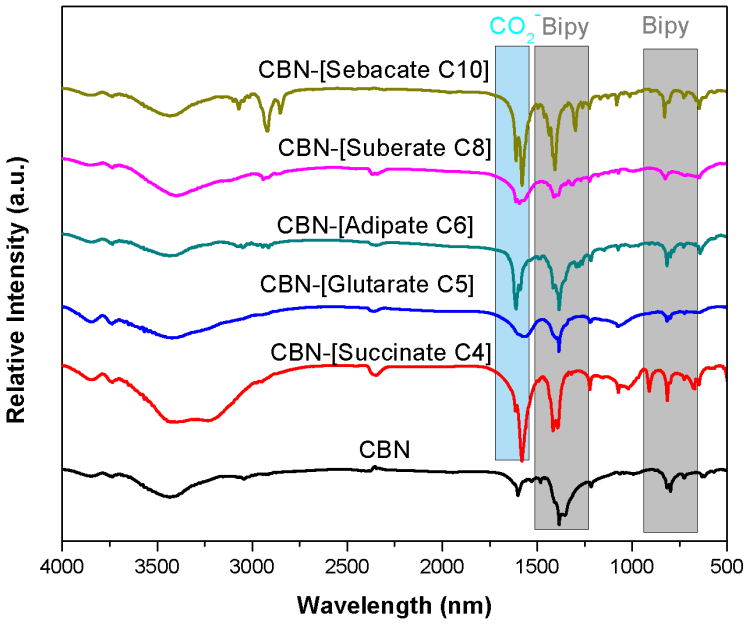

Figure 4.10: FT-IR spectra of CBN exchanges with series of α,ω-alkanedicarboxylates, [$^{-}O_2C(CH_2)_nCO_2^{-}$] where light blue block represents carboxylate stretches whereas grey block represents bipyridine stretches.

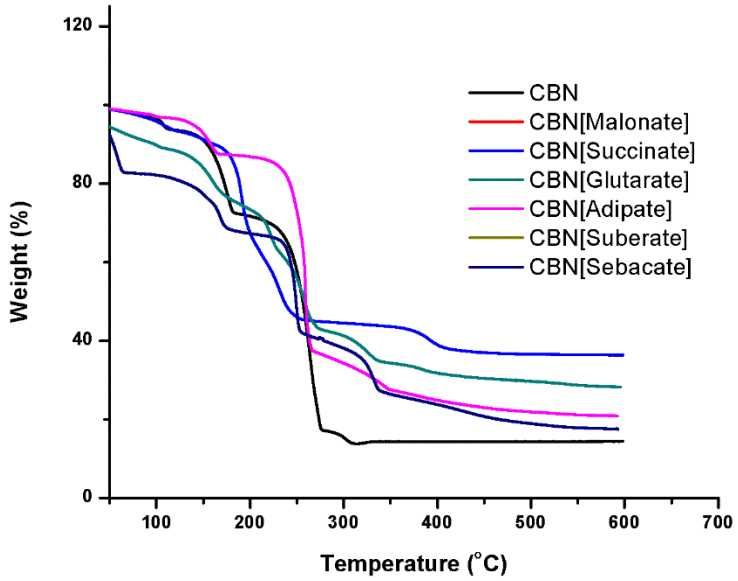

Figure 4.11: TGA data of CBN and exchanges with series of α,ω-alkanedicarboxylates.

TGA analysis was performed to see if the exchange materials are thermally stable compared to as-synthesized CBN (Figure 4.11). The major weight loss of dicarboxylate materials were overall not much different compared to CBN. Therefore, the further analysis of *in-situ* variable temperature(VT) PXRD would be recommended to examine their new crystalline phases of exchange materials.

4.4. Conclusion and Remarks

The Cu(I) based cationic coordination polymer (CP) has been rationally synthesized from simple bipyridine ligand and copper(II) nitrate. The loosely bound nitrates from CBN create a good opportunity to exchange for anion pollutants because nitrate release to the environment would be favorable for the environmental remediation of toxic anions. In this study, CBN has the selective potential to trap toxic oxo-anion, chromate, in the high capacity (242 mg/g). With the formation of a new crystal structure favored? by hydration energy, the chromate would be permanently trapped. Attempts to exchange other oxo-anions such as perrhenate, tetrafluoroborate were not successful, likely due to the lower redox stability of Cu(I). In addition to oxo-anion exchange, the material displays flexibility for variable-length α,ω-alkanedicarboxylates, which may be a pathway to adsorbing problematic organic anions and/or increasing capacity. The completion of the exchange process was supported by PXRD, TGA and FT-IR. Further investigation of VT-PXRD for dicarboxylates-exchange materials would provide the deeper understanding of their anion exchange capabilities. This study might open up further possibilities for introducing other anions or abatement of problematic anions such as pharmaceuticals and their metabolites.

4.5. References

(1) Blake, A. J.; Champness, N. R.; Hubberstey, P.; Li, W.-S.; Withersby, M. A.; Schröder, M. Inorganic Crystal Engineering Using Self-Assembly of Tailored Building-Blocks. *Coord. Chem. Rev.* **1999**, *183* (1), 117–138. https://doi.org/10.1016/S0010-8545(98)00173-8.

(2) Batten, S. R.; Neville, S. M.; Turner, D. R. *Coordination Polymers: Design, Analysis and Application*; Royal Society of Chemistry, 2008.

(3) Yaghi, O. M.; Li, H.; Davis, C.; Richardson, D.; Groy, T. L. Synthetic Strategies, Structure Patterns, and Emerging Properties in the Chemistry of Modular Porous Solids †. *Acc. Chem. Res.* **1998**, *31* (8), 474–484. https://doi.org/10.1021/ar970151f.

(4) Fei, H.; Bresler, M. R.; Oliver, S. R. J. A New Paradigm for Anion Trapping in High Capacity and Selectivity: Crystal-to-Crystal Transformation of Cationic Materials. *J. Am. Chem. Soc.* **2011**, *133* (29), 11110–11113. https://doi.org/10.1021/ja204577p.

(5) Cao, R.; McCarthy, B. D.; Lippard, S. J. Immobilization, Trapping, and Anion Exchange of Perrhenate Ion Using Copper-Based Tripodal Complexes. *Inorg. Chem.* **2011**, *50* (19), 9499–9507. https://doi.org/10.1021/ic201172r.

(6) Fei, H.; Han, C. S.; Robins, J. C.; Oliver, S. R. J. SLUG-35 A Cationic Metal–Organic Solid Solution Based on Co(II) and Zn(II) for Chromate Trapping. *Chem. Mater.* **2013**, *25* (5), 647–652. https://doi.org/10.1021/cm302585r.

(7) Fei, H.; Rogow, D. L.; Oliver, S. R. J. SLUG 22- Reversible Anion Exchange and Catalytic Properties of Two Cationic Metal−Organic Frameworks Based on Cu(I) and Ag(I). *J. Am. Chem. Soc.* **2010**, *132* (20), 7202–7209. https://doi.org/10.1021/ja102134c.

(8) Cui, X.; Khlobystov, A. N.; Chen, X.; Marsh, D. H.; Blake, A. J.; Lewis, W.; Champness, N. R.; Roberts, C. J.; Schröder, M. Dynamic Equilibria in Solvent-Mediated Anion, Cation and Ligand Exchange in Transition-Metal Coordination Polymers: Solid-State Transfer or Recrystallisation? *Chem. – Eur. J.* **2009**, *15* (35), 8861–8873. https://doi.org/10.1002/chem.200900796.

(9) Colinas, I. R.; Silva, R. C.; Oliver, S. R. J. Reversible, Selective Trapping of Perchlorate from Water in Record Capacity by a Cationic Metal–Organic Framework. *Environ. Sci. Technol.* **2016**, *50* (4), 1949–1954. https://doi.org/10.1021/acs.est.5b03455.

(10) Crawford, N. M.; Glass, A. D. M. Molecular and Physiological Aspects of Nitrate Uptake in Plants. *Trends Plant Sci.* **1998**, *3* (10), 389–395. https://doi.org/10.1016/S1360-1385(98)01311-9.

(11) Yaghi, O. M.; Li, H. Hydrothermal Synthesis of a Metal-Organic Framework Containing Large Rectangular Channels. *J. Am. Chem. Soc.* **1995**, *117* (41), 10401–10402. https://doi.org/10.1021/ja00146a033.

(12) Keith, L.; Telliard, W. ES&T Special Report: Priority Pollutants: I-a Perspective View. *Environ. Sci. Technol.* **1979**, *13* (4), 416–423. https://doi.org/10.1021/es60152a601.

(13) Izak, P.; Hrma, P.; Arey, B. W.; Plaisted, T. J. Effect of Feed Melting, Temperature History, and Minor Component Addition on Spinel Crystallization in High-Level Waste Glass. **2001**, 13.

(14) Daughton, C. G. PPCPs in the Environment: Future Research — Beginning with the End Always in Mind. In *Pharmaceuticals in the Environment*; Springer, Berlin, Heidelberg, 2004; pp 463–495. https://doi.org/10.1007/978-3-662-09259-0_33.

(15) Chibwe, K.; Jones, W. Intercalation of Organic and Inorganic Anions into Layered Double Hydroxides. *J. Chem. Soc. Chem. Commun.* **1989**, *0* (14), 926–927. https://doi.org/10.1039/C39890000926.

(16) Hibino, T.; Tsunashima, A. Characterization of Repeatedly Reconstructed Mg−Al Hydrotalcite-like Compounds: Gradual Segregation of Aluminum from the Structure. *Chem. Mater.* **1998**, *10* (12), 4055–4061. https://doi.org/10.1021/cm980478q.

(17) J. Oliver, S. R. Cationic Inorganic Materials for Anionic Pollutant Trapping and Catalysis. *Chem. Soc. Rev.* **2009**, *38* (7), 1868–1881. https://doi.org/10.1039/B710339P.

(18) Li, X.; Gao, X.; Ai, L.; Jiang, J. Mechanistic Insight into the Interaction and Adsorption of Cr(VI) with Zeolitic Imidazolate Framework-67 Microcrystals from Aqueous Solution. *Chem. Eng. J.* **2015**, *274*, 238–246. https://doi.org/10.1016/j.cej.2015.03.127.

(19) Custelcean, R. Anions in Crystal Engineering. *Chem. Soc. Rev.* **2010**, *39* (10), 3675–3685. https://doi.org/10.1039/B926221K.

(20) Custelcean, R.; Bock, A.; Moyer, B. A. Selectivity Principles in Anion Separation by Crystallization of Hydrogen-Bonding Capsules. *J. Am. Chem. Soc.* **2010**, *132* (20), 7177–7185. https://doi.org/10.1021/ja101354r.

(21) Custelcean, R.; Moyer, B. A. Anion Separation with Metal–Organic Frameworks. *Eur. J. Inorg. Chem.* **2007**, *2007* (10), 1321–1340. https://doi.org/10.1002/ejic.200700018.

CHAPTER (5)

Metal-Organic Frameworks as Electrocatalysts for Oxygen Reduction Reaction (ORR)

Abstract

The development of clean energy has been the subject of recent attention. Various energy storage and conversion systems are being established and aimed at the utilization of different clean energy sources. With the approaching commercialization of PEM fuel cell technology, developing active, inexpensive non-precious metal ORR catalyst materials to replace currently used Pt-based catalysts is an essential requirement in order to reduce the overall system cost. Metal-organic frameworks (MOFs) are highly porous materials with large surface area and well-defined pore size distributions which play a crucial role in the ORR reaction. Herein, a series of Zn-doped MIL-101 (Materials of Institute Lavoisier) MOFs was synthesized to study electrocatalytic activity. Two research labs from the UCSC Chemistry Department has collaborated for this project. The Oliver lab, our group, is mainly focused on the synthesis of MOFs whereas the Chen lab conducted the electrochemical performance testing of MOF catalysts. Three MIL101-NH_2 materials with a different weight percentage of Zn content was prepared to explore the effect of zinc content on morphology and catalytic activity of MOFs. The materials were characterized by PXRD, TGA, SEM, and ICP.

5.1. Introduction

5.1.1. Non-Precious Metal Catalysts for Fuel Cell Technologies

In order to avoid environmental pollution and an energy shortage, the application of clean and renewable energy, such as solar, instead of fossil fuels is a forthcoming issue. It is vital to develop and optimize various energy storage and conversion technologies and materials aimed at the utilization of different energy sources.[1] Electrochemical energy storage is considered one of the most promising methods of storing clean energy. In this case, hydrogen-powered fuel cells are one of the best alternatives to fossil fuels as they offer a clean and carbon-free method of converting chemical energy directly into electrical energy. Furthermore, they are almost twice as efficient as fossil fuels (60% efficiency for fuel cells versus 34% for fossil fuels).[2] In many fuel cells, the polymer electrolyte membrane fuel cell (PEMFC), which can efficiently convert chemical energy into electricity through electrochemical reactions, is considered ideal power sources. The approaching commercialization of PEMFC is still hindered by the high cost and limited operational stability of the platinum (Pt)-based cathode catalysts traditionally utilized.[3]

One promising approach in this field is to develop non-precious metal-based electrocatalysts (NPMCs). These catalysts are generally carbon supported transition metal/nitrogen (M-N_x-C) materials (M = Fe, Co, Zn, Ni, Mn, etc. and normally, x = 2 or 4) formed by the pyrolysis of a variety of metal, nitrogen, and carbon precursor materials.[4] It was initially demonstrated in 1964 that transition metal porphyrins,

namely cobalt phthalocyanine, could act as ORR electrocatalysts in alkaline conditions.[5] Later, the catalytic activity of various metal–N_4 complexes supported on carbon was demonstrated in acidic media. However, stability issues arose as the catalyst structures were found to decompose in the presence of acid, resulting in a loss of catalytic activity.[6] In recent years, the electrochemists found a high-temperature pyrolysis procedure which could increase the concentration of ORR active sites while improving the catalytic stability. Several factors were important to the activity and stability of pyrolyzed M–N_x-C electrocatalysts, including transition metal type and loading, carbon support surface properties, nitrogen content, and heat treatment conditions and duration. Unfortunately, until today, the performance of the best non-precious metal catalysts is still inferior when compared to Pt-based catalysts in terms of both activity and stability. However, the incremental improvement in both activity and stability of non-precious metal catalysts towards their practical usage has been seen in recent years. Therefore, this approach is making more active promising fuel cell stack and demand is only going to increase.[7]

5.1.2. MOF-Derived Porous Carbon as ORR Catalysts

Metal-organic frameworks (MOFs) with controllable size and shape are possible pyrolytic precursors to achieve high-performance ORR catalysts. This idea is mainly based on two considerations. First, MOFs represent a new family of crystalline framework materials (more than 6000 members to date) made by linking metal ions (Zn, Fe, Co, etc.) to organic moieties (synthetic small molecules, amino acids, peptides, etc.) through coordination interactions.[8,9] Owing to their diverse

composition, high surface area, and controllable porous structure, MOFs offer an opportunity to obtain high-performance NPMCs if the porosity and uniformity of the catalytic active sites can be maintained after pyrolysis.[1]

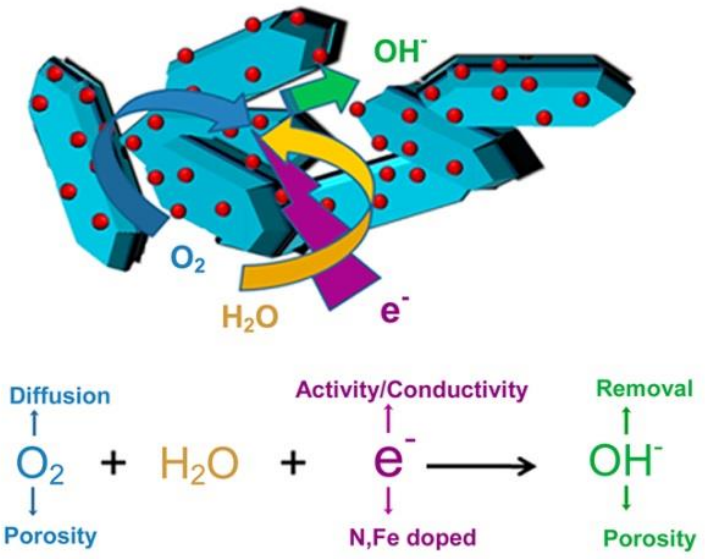

Figure 5.1: Principle of high-performance electrocatalysts (porous NPMC) for oxygen reduction reaction in alkaline solution. Red dots represents metal-doped nanoparticles.[10]

Second, compared with macro- or micro-scale materials, nanoscale materials have a much greater capability to resist drastic structural or morphological damage caused by high-temperature pyrolysis, and the larger surface-to-volume ratio would also help electrocatalytic reactions if the sizes of the pyrolytic products could be kept in the nanometer scale. [1,11,12] Figure 5.1 illustrates the criteria for ORR active NPMC. The first example of a MOF-derived ORR catalyst was found by activating cobalt

imidazolate frameworks (CoIM) at high temperature and it is since this research that more attention has been paid to this field.[13]

From this strategy, one of the classic MOFs, MIL101, $Fe_3F(H_2O)_2O[(O_2C)C_6H_4(CO_2)]_3 \bullet nH_2O$ (where n is ~25), was recently chosen because of its high stability in water, large surface area, and two hydrophilic zeolite-type cavities. Aijaz and co-workers introduced Pt nanoparticles inside the pores of MIL101, without Pt aggregation on the external surface of framework.[14] The resulting Pt@MIL101 composites exhibited excellent catalytic performances by using a two solvent method that could avoid Pt aggregation. The MIL101 synthesis is based on a hydrophilic solvent (water) and a hydrophobic solvent (hexane). The water containing the metal precursor with a volume set equal to or less than the pore volume of the adsorbent (MIL101), which can be absorbed within the hydrophilic adsorbent pores, and hexane is playing an important role to suspend the adsorbent and facilitate the impregnation process (Figure 5.2).

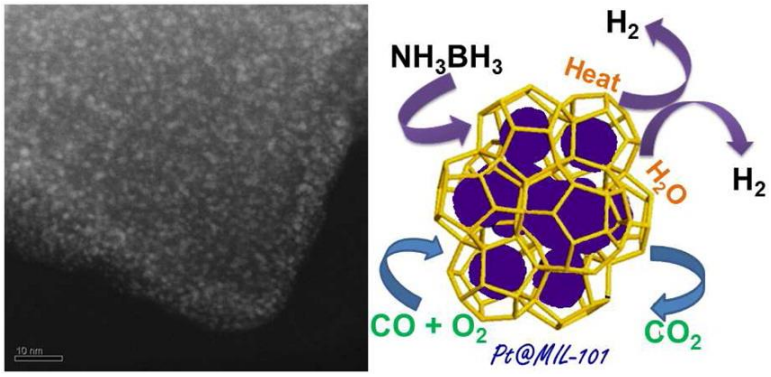

Figure 5.2: Schematic representation of the synthesis of Pt nanoparticles (purple) inside the MIL101 matrix (gold).[14]

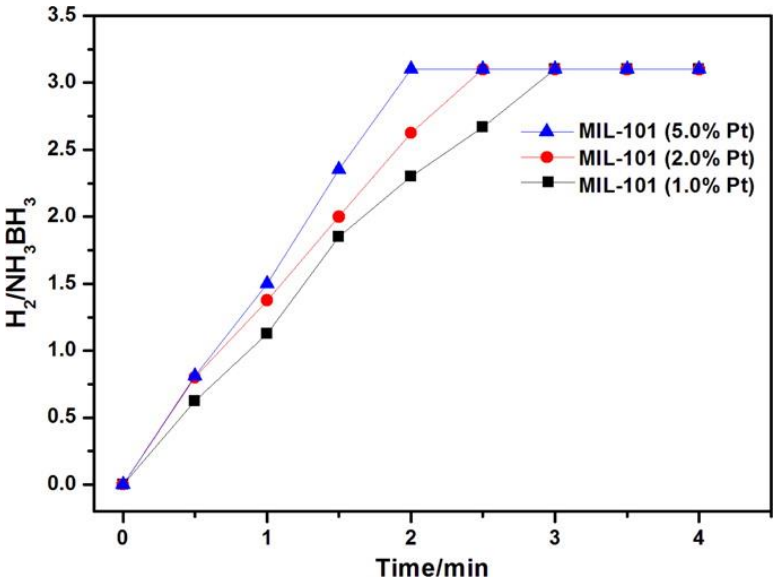

Figure 5.3: Hydrogen generation from aqueous NH_3BH_3 (ammonia borane, AB) in the presence of Pt@MIL101 catalysts at room temperature. Pt/AB (molar ratio) = 0.0014, 0.0029, and 0.0071 at Pt loadings of 1.0, 2.0 and 5.0%, respectively.[14]

Pt@MIL101 with different Pt loadings displayed high activity for the hydrolysis of ammonia borane (AB), exhibiting a hydrogen release of H_2/AB = 3 within 2.5 mins (Figure 5.3). These MOFs provided the opportunity to produce the highly active

species for ORR such as Fe/Fe_3C after pyrolyzing. In addition, the Fe and N co-doped carbon materials have better conductivity than pure carbon, which would benefit electrochemical reactions such as ORR. Therefore, the Chen lab, with extensive electrochemical research expertise, was inspired to collaborate with our group where the desired MOFs could be accessible. In this study, a series of iron oxide N co-doped graphitic nanoparticles were systematically derived from a series of porous MOFs with the same organic linkers, but with metal centers that varied from iron to a mixture of iron and zinc. The catalysts derived from the pyrolysis might maintain similar geometry to the precursor MOFs and the evaporation of zinc increased pore size and surface area while making iron accessible for ORR.

5.2. Experimental Section

5.2.1. Reagents

Iron (III) chloride hexahydride ($FeCl_3•6H_2O$, Fischer Scientific), 2-aminoterepthalic acid (NH_2-BDC) ($C_8H_7NO_4$, Acros Organic) and zinc chloride ($ZnCl_2$, Toyoko Chemical Industry) were used as received for the synthesis.

5.2.2. Synthesis of MIL-101-NH_2 [$Fe_3O(NH_2\text{-}BDC)_3Cl•3(H_2O)$]

The synthesis of the MIL101-NH_2 was based on a previously reported method.[15] Iron (III) chloride hexahydrate and 2-aminoterepthalic acid were mixed in a 1:3 ratio by stirring each into 5 mL of Millipore water and then combined into a 15mL Teflon lined autoclave and heated for 24 hours at 110°C. The sample was then filtered, rinsed with water and ethanol, then dried at ambient conditions to produce orange-red

micro-crystals. A series of MOFs, Fe x%-Zn(1-x%)-MIL101-NH_2, was synthesized following the procedure above where a fraction of the iron (III) chloride hexahydrate was substituted with zinc chloride to vary the zinc content from 0% to 30% of the total metal. Four types of MOFs, 0%Zn-MIL101-NH_2, 10%Zn-MIL101-NH_2, 20%Zn-MIL101-NH_2, and 30%Zn-MIL101-NH_2, were synthesized.

5.2.3. Instrumental Details

Powder X-ray diffraction spectroscopy (PXRD) measurements were taken with a Rigaku SmartLab Plus diffractometer with Cu Kα (λ = 1.54 Å) radiation, operated at 40 kV and 44 mA. Diffraction data of as-synthesized MOFs were recorded from 2° to 35° (2θ) at a rate of 3° per minute with a 0.01° step size. Diffraction data of MOF catalysts were collected from 10° to 80° (2θ) at a rate of 0.33° per minute with a 0.01° step size. Scanning electron microscopy (SEM) images were taken with an FEI Quanta 3D field emission microscope. Thermogravimetric analysis (TGA) was performed using a TA Instruments 2050 TGA by heating from 25 to 600 °C with a gradient of 10 °C/min and nitrogen flow. Inductively coupled plasma optical emission spectrometry (ICP-OES) data were acquired on a Perkin Elmer Optima 4300DV, run in a radial mode using yttrium as an internal standard.

4.3. Results and Discussion

5.3.1. Synthesis and Structure properties

Three MIL101-NH_2 with a different weight percentage of zinc content was prepared to investigate the effect of zinc content of morphology and catalytic activity of MOFs (Figure 5.4).

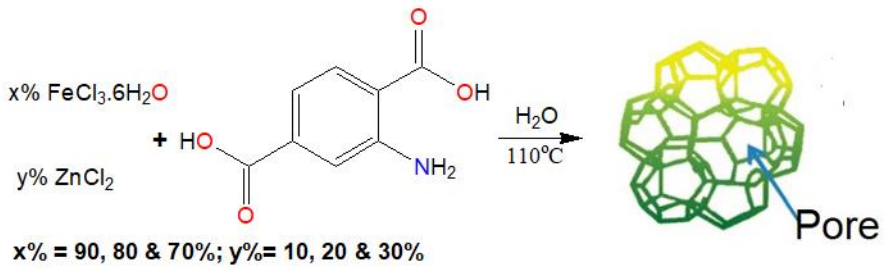

Figure 5.4: Synthetic Scheme of Fe x%- Zn y% MOF101-NH_2.

PXRD of as-synthesized MOFs is presented in Figure 5.5 along with the theoretical spectra of IRMOF-3 and MIL101-NH_2. All as-synthesized x%Zn-MIL101-NH_2 MOFs showed the characteristic low-angle peaks of 8.86° and 17.1° 2θ, corresponding to MIL101-NH_2. As the amount of zinc ratio increased, crystalline peaks at 6.86° and 26.5° (2θ) are attributed to the theoretical spectrum of IRMOF-3.

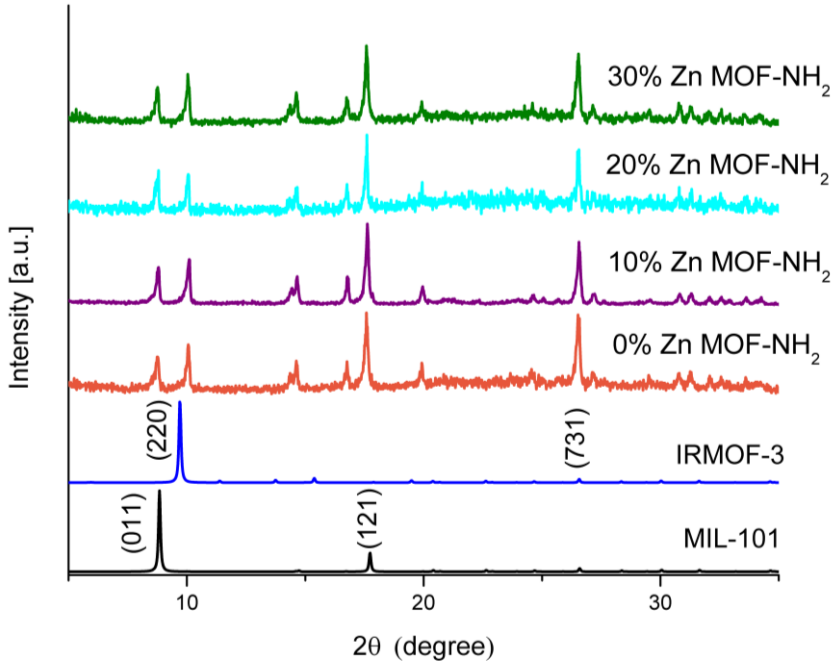

Figure 5.5: PXRD patterns of the series of x%Zn-MIL101-NH_2.

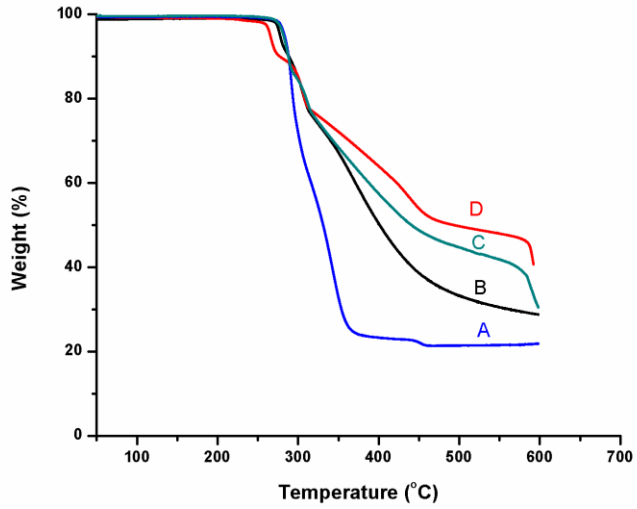

Figure 5.6: TGA traces of (a) 20%Zn-MIL101-NH_2; (b) 0%Zn-MIL101-NH_2 (black); (c) 10%Zn-MIL101-NH_2 (green); and (d) 30%Zn-MIL101-NH_2.

TGA analysis was examined to see if the thermal profile of each material can give insight toward being beneficial for the high-temperature pyrolysis process (Figure 5.6). All as-prepared MOFs shown the same initial weight loss due to the organic components from the frameworks. The remaining data was slightly different, and it is concluded that the different weight percentage of Zn loading might be accounted for. In order to quantify the Fe and Zn metal content for each MOF, ICP study was conducted (Table 5.1).

Table 5.1: ICP of x%Fe-1-x%Zn-MIL101-NH_2.

x%Fe-1-x%Zn-MIL101-NH_2	Fe (ppm)	Zn (ppm)	Fe (%)	Zn (%)
90%Fe-10%Zn MIL101-NH_2	0.035	0.057	92.4	7.6
80%Fe-20%Zn MIL101-NH_2	0.034	0.004	82.3	17.7
70%Fe-30%Zn MIL101-NH_2	0.012	0.003	67.4	32.6

The ICP results are close to the theoretical metal content that was prepared for these MOFs. Due to the high sensitivity of Zn to the atmosphere and surroundings in ICP-OES, a slight data deviation was detected.

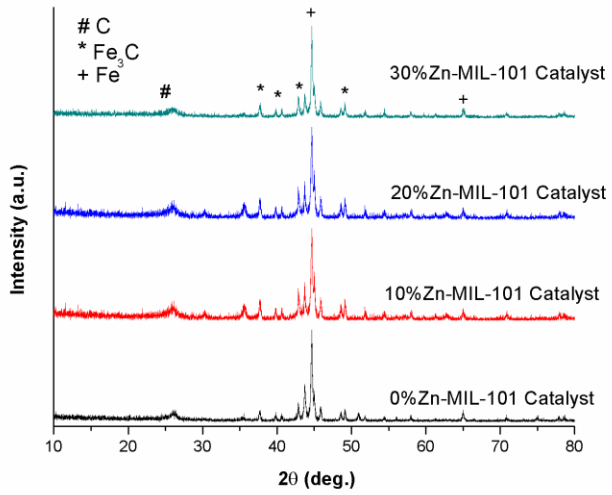

Figure 5.7: PXRD pattern of series of x%Zn-MIL101-NH_2 after pyrolysis at 900 °C.

PXRD patterns of the three samples after pyrolysis are given in Figure 5.7. The diffraction peak at 26.1° appeared in all PXRD patterns is assigned to (002) plane of graphitic carbon, and the peaks at 43.8°, 44.7°, and 50.8° could be assigned to cementite (Fe_3C, JCPDS No. 35-0772). The metallic Fe (JCPDS No. 06-0696) was detected at diffraction peaks at 45.2° and 65.6°. These results indicated that graphitic carbon, Fe_3C, and metallic Fe coexisted in all three catalysts.

It was found that as the amount of zinc in the MOF increased, the resulting catalyst would have an increase in the elemental iron. Eventually, the amount of iron leads to the formation of iron metal and thus there might be an optimal ratio of zinc to iron for the design of these ORR catalysts. Among these different Zn loading on MIL101-NH_2 MOFs, the overall morphology of 20% Zn MOF is shown to be preserved after pyrolysis at 900°C under a nitrogen flow (Figure 5.8). Notably, the

SEM image revealed that the 20% Zn MOF 900°C catalyst was a micrometer-scale porous carbon catalyst whose surface contains Fe? nanoparticles with a diameter of ~0.5 μm.

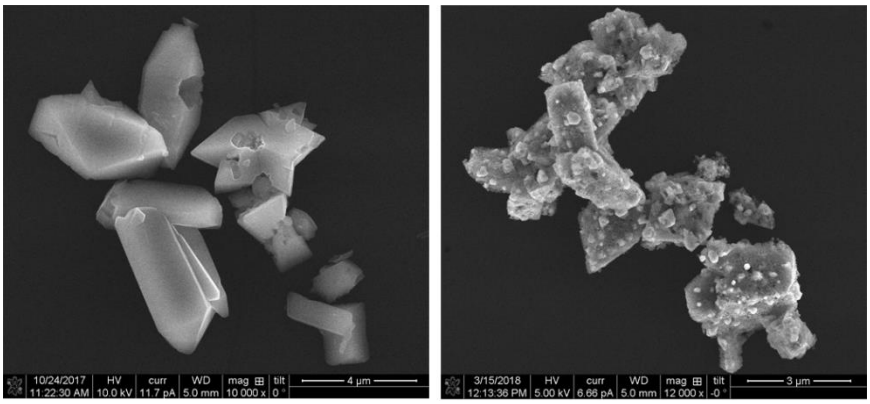

Figure 5.8: SEM image of as-synthesized 20%Zn-MIL101-NH_2 (left) and 20%Zn-MIL101-NH_2 after pyrolysis at 900 °C. Scale bars are 4 μm and 3 μm, respectively.

Upon completion of characterization and choosing the best Zn-MIL101-NH_2 catalysts, the materials were brought Chen lab to test the rest of electrocatalytic performances.

5.4. Conclusion and Remarks

We reported three Zn-doped MIL101-NH_2 materials for potential use as ORR electrocatalysts. These MOFs have been well-characterized and shown to maintain Zn-Fe content from the synthesis. Among them, 20%Zn-MIL101-NH_2 displayed the best morphology and stability as a potential electrocatalyst for ORR. It will be exciting to see the detailed investigation of their electrochemical performance and tolerance towards ORR in the alkaline system.

Many materials have been investigated lately in the search for the best materials for electrochemical energy storage, including MOFs; however, producing an efficient design still remains a big challenge. Expectantly, this study will provide the ability to properly design synthesis procedures to adequately tailor catalytically active sites, with the goal of producing highly active and durable electrocatalyst materials for PEM fuel cell applications.

5.5 References

(1) Li, S.-L.; Xu, Q. Metal-Organic Frameworks as Platforms for Clean Energy. *Energy Environ. Sci.* **2013**, *6* (6), 1656–1683. https://doi.org/10.1039/C3EE40507A.

(2) Vielstich, W.; Gasteiger, H. A.; Yokokawa, H. *Handbook of Fuel Cells: Advances in Electrocatalysis, Materials, Diagnostics, and Durability*; John Wiley & Sons, 2009.

(3) Zhang, S.; Yuan, X.-Z.; Hin, J. N. C.; Wang, H.; Friedrich, K. A.; Schulze, M. A Review of Platinum-Based Catalyst Layer Degradation in Proton Exchange Membrane Fuel Cells. *J. Power Sources* **2009**, *194* (2), 588–600. https://doi.org/10.1016/j.jpowsour.2009.06.073.

(4) Bezerra, C. W. B.; Zhang, L.; Lee, K.; Liu, H.; Marques, A. L. B.; Marques, E. P.; Wang, H.; Zhang, J. A Review of Fe–N/C and Co–N/C Catalysts for the Oxygen Reduction Reaction. *Electrochimica Acta* **2008**, *53* (15), 4937–4951. https://doi.org/10.1016/j.electacta.2008.02.012.

(5) Jasinski, R. A New Fuel Cell Cathode Catalyst. *Nature* **1964**, *201* (4925), 1212–1213. https://doi.org/10.1038/2011212a0.

(6) Alt, H.; Binder, H.; Sandstede, G. Mechanism of the Electrocatalytic Reduction of Oxygen on Metal Chelates. *J. Catal.* **1973**, *28* (1), 8–19. https://doi.org/10.1016/0021-9517(73)90173-5.

(7) Bashyam, R.; Zelenay, P. A Class of Non-Precious Metal Composite Catalysts for Fuel Cells. In *Materials for Sustainable Energy*; Co-Published with

Macmillan Publishers Ltd, UK, 2010; pp 247–250. https://doi.org/10.1142/9789814317665_0034.

(8) Furukawa, H.; Cordova, K. E.; O'Keeffe, M.; Yaghi, O. M. The Chemistry and Applications of Metal-Organic Frameworks. *Science* **2013**, *341* (6149), 1230444. https://doi.org/10.1126/science.1230444.

(9) Cao, X.; Zheng, B.; Rui, X.; Shi, W.; Yan, Q.; Zhang, H. Metal Oxide-Coated Three-Dimensional Graphene Prepared by the Use of Metal-Organic Frameworks as Precursors. *Angew. Chem. Int. Ed.* **2014**, *53* (5), 1404–1409. https://doi.org/10.1002/anie.201308013.

(10) Zhao, S.; Yin, H.; Du, L.; He, L.; Zhao, K.; Chang, L.; Yin, G.; Zhao, H.; Liu, S.; Tang, Z. Carbonized Nanoscale Metal-Organic Frameworks as High-Performance Electrocatalyst for Oxygen Reduction Reaction. *ACS Nano* **2014**, *8* (12), 12660–12668. https://doi.org/10.1021/nn505582e.

(11) Chung, H. T.; Won, J. H.; Zelenay, P. Active and Stable Carbon Nanotube/Nanoparticle Composite Electrocatalyst for Oxygen Reduction. *Nat. Commun.* **2013**, *4*, 1922. https://doi.org/10.1038/ncomms2944.

(12) Zhang, P.; Sun, F.; Xiang, Z.; Shen, Z.; Yun, J.; Cao, D. ZIF-Derived in Situ Nitrogen-Doped Porous Carbons as Efficient Metal-Free Electrocatalysts for Oxygen Reduction Reaction. *Energy Environ. Sci.* **2014**, *7* (1), 442–450. https://doi.org/10.1039/C3EE42799D.

(13) Ma, S.; Goenaga, G. A.; Call, A. V.; Liu, D.-J. Cobalt Imidazolate Framework as Precursor for Oxygen Reduction Reaction Electrocatalysts. *Chem. – Eur. J.* **2011**, *17* (7), 2063–2067. https://doi.org/10.1002/chem.201003080.

(14) Aijaz, A.; Karkamkar, A.; Choi, Y. J.; Tsumori, N.; Rönnebro, E.; Autrey, T.; Shioyama, H.; Xu, Q. Immobilizing Highly Catalytically Active Pt Nanoparticles inside the Pores of Metal–Organic Framework: A Double Solvents Approach. *J. Am. Chem. Soc.* **2012**, *134* (34), 13926–13929. https://doi.org/10.1021/ja3043905.

(15) Bauer, S.; Serre, C.; Devic, T.; Horcajada, P.; Marrot, J.; Férey, G.; Stock, N. High-Throughput Assisted Rationalization of the Formation of Metal Organic Frameworks in the Iron(III) Aminoterephthalate Solvothermal System. *Inorg. Chem.* **2008**, *47* (17), 7568–7576. https://doi.org/10.1021/ic800538r.

CHAPTER (6)

Conclusions and Future Work

6.1. Conclusions

The work presented in this thesis shows the important progress in the synthesis of cationic metal coordination polymers (CPs) for the fields of water remediation, photoluminescence, and electrochemistry. The main project involves developing new and existing silver(I) CPs for their potential applications such as anion exchange and photoluminescence. These silver cationic crystalline polymers perform excellent trapping of oxo-anion pollutants and organic contaminants compared to that of the commercial organic resins. They also display great emission making them potentially useful as white LEDs. Lastly, another small project includes the synthesis of zinc doped iron-based organic frameworks as active electrocatalysts for oxygen reduction reaction in fuel cell technologies.

First, a cationic silver(I) pyrazine (pyz) material that can trap selectively harmful oxo-anions from water such as permanganate, perrhenate and a variety of α,ω-alkanedicarboxylates was reported. The favorable anion exchange reaction is driven by the weakly bound nitrate anions counterbalancing between $[Ag(pyz)^{+}]$ chains. The exchange capacity at 435 and 818 mg/g for permanganate and perrhenate demonstrated higher performance over the anion exchange commercial resin, Purolite 530E, within 24 h. This material also displays superior uptake towards over organic pollutants through a series of α,ω-alkanedicarboxylates. The selectivity amongst these

dicarboxylates was also performed and sebacate, the longest carbon chain length among them, outperform due to its great amphiphilic properties. Hence, this insight presents a significant advance in the methods available for water remediation.

New syntheses of two cationic silver quinoxaline CPs was developed via a one-step synthetic method, with high yield and phase purity. SLUG-37 contains silver-quinoxaline layers, both bridged and charge-balanced by ethanedisulfonate while those of SLUG-38 are only charge-balanced by the acetate anions. Both structures consist of cationic 1D chains arranged into π-stacked layers, with charge-balancing anions residing in the interlamellar space. Both SLUGs display excellent thermal stability by VT-PXRD and TGA with transformation to silver sulfate and oxide at a higher temperature. White light emitting SLUG-37 exhibits efficient photoluminescence behavior at 540 nm.

Lastly, one promising approach in the clean energy storage design is to develop non-precious metal-based electrocatalysts derived from the pyrolysis of metal-organic frameworks (MOFs). The main goal for this project is to investigate the effect of activating zinc on the porous surface of iron carbide containing nitrogen-doped carbon catalysts for the oxygen reduction reaction. The careful synthesis of three different Zn-doped MIL101-NH_2 MOFs was designed by Oliver lab. The electrochemical study involves a collaboration with Chen research group.

6.2. Future Work

The future work of [Ag(pyrazine)$^{+}$][NO_3^{-}] will involve comparing the exchange capacity with well-known LDH s and other cationic extended materials. The batch sorption experiments at lower concentrations (EPA standard ppm) would be interesting to study whether the material can exert anion exchange effectively especially at lower concentration ppm level. Another major future work is to investigate the selectivity exchange experiments in the presence of a multiple-fold excess of potentially competing common anions including sulfate, carbonate, and chloride. One of the future directions includes testing anion exchanges using actual contaminated water from plume sites for the material evaluation. By using HPLC, these alkanedicarboxylates exchange materials could be able to quantify their adsorption capacity. It would be a great interest to elucidate density functional theory (DFT) in order to understand the exchange mechanism at the molecular level.

Although attempts to exchange SLUG-37 with other anions such as nitrate, perchlorate, permanganate or chromate has not been successful, the direct synthesis to incorporate these anions to yield new crystal structures would be rather interesting. Further efforts should be focused on the construction of SLUG-37 with multifunctional sites such as preferential and selective binding with different ions, leading to highly selective and sensitive luminescent coordination polymers. By comparing with similar ligand-based fluorescence in closely-related structures, allowing the luminescence properties to be correlated with structural features of the framework would be fascinating. Considering the structure, SLUG-38 is less stable

and somewhat challenging to synthesize, and anion exchange could not be investigated. Therefore, another future work involves developing the facile synthesis for SLUG-38. The new future direction for this project is exploring other transitional metals such as Ni, Mn or Zn for new potential quinoxaline layered structures. These new crystalline materials are an important step in the discovery of cationic extended frameworks where the linker is varied from the typical 4,4'-bipyridine of previous structures from our group. Suggesting other N-donor ligands such as DNA base-pair molecules for variation in structure type and in turn properties.

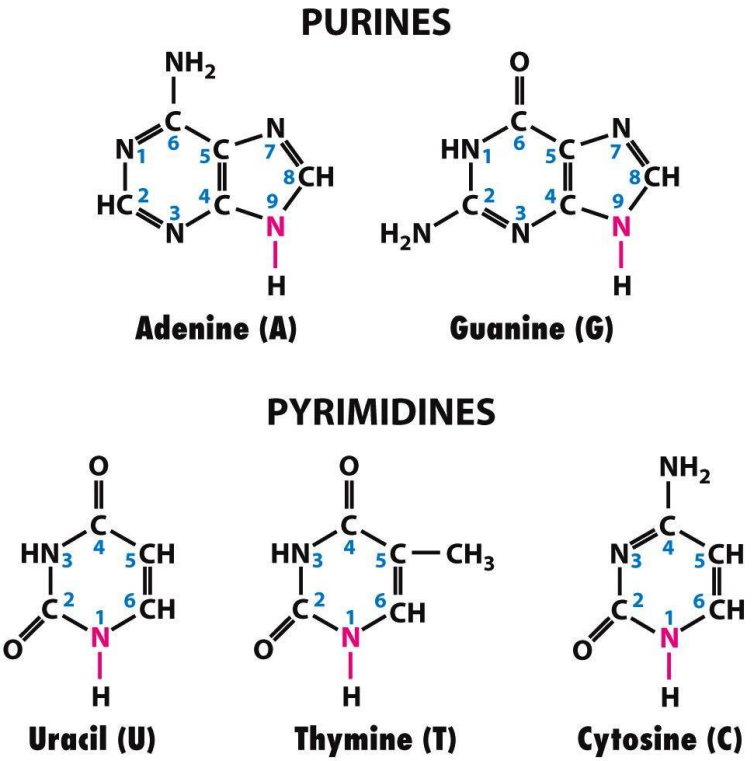

With the goal of producing highly active and robust electrocatalyst materials for oxygen reduction reaction, other possible transitional metals-doped MIL101-NH_2 can be further examined. As a supplementary investigation, these porous crystalline

materials can be tested for other hydrogen production, such as an interesting electrocatalytic hydrogen evolution reaction. One of the challenges for MOFs is that they cannot survive high-temperature pyrolysis. The future work for this part of the project is to develop metal-organic frameworks with the high surface area, porosity, and thermal stability for pyrolysis.

Appendix

Table A1: $[Ag(pyrazine)^{+}][NO_3^{-}]$ Synthesis

Sample ID	Reagents	Ratio (mmol)	F.W. (g/mol)	Target Mass (g)	Actual Mass (g)	Temperature (°C)	Time (h)
ES-I-105A	$AgNO_3$	3	169.87	0.50961	0.5052	70	1
	Pyrazine	1	80.09	0.0800	0.0801		
	MilliQ H_2O				4		
ES-I-105B	$AgNO_3$	3	169.87	0.50961	0.5112	70	1
	Pyrazine	1	80.09	0.0800	0.0777		
	MilliQ H_2O				4		
ES-I-106A	$AgNO_3$	1	169.87	0.50961	0.1696	150	24
	Pyrazine	1	80.09	0.0800	0.0887		
	MilliQ H_2O				10		
ES-I-106B	$AgNO_3$	1	169.87	0.50961	0.1696	150	20
	Pyrazine	1	80.09	0.0800	0.0887		
	MilliQ H_2O				10		
ES-II-10A	$AgNO_3$	2	169.87	0.3397	0.3395	70	1
	Pyrazine	2	80.09	0.1600	0.1587		
	MilliQ H_2O				10		
ES-II-10B	$AgNO_3$	2	169.87	0.3397	0.3375	70	1
	Pyrazine	2	80.09	0.1600	0.1599		
	MilliQ H_2O				10		
ES-II-17A	$AgNO_3$	1	169.87	0.1699	0.16957	150	24
	Pyrazine	1	80.09	0.080	0.0805		
	MilliQ H_2O				10		
ES-II-17B	$AgNO_3$	1	169.87	0.1699	0.1684	150	24
	Pyrazine	1	80.09	0.080	0.0810		
	MilliQ H_2O				10		
ES-II-17C	$AgNO_3$	1	169.87	0.1699	0.1707	150	24
	Pyrazine	1	80.09	0.080	0.0801		
	MilliQ H_2O				10		
ES-II-17D	$AgNO_3$	1	169.87	0.1699	0.1683	150	24
	Pyrazine	1	80.09	0.080	0.0825		
	MilliQ H_2O				10		
ES-II-89A	$AgNO_3$	1	169.87	0.1699	0.1699	150	24
	Pyrazine	1	80.09	0.080	0.0800		
	MilliQ H_2O				10		

ES-II-89B	$AgNO_3$	1	169.87	0.1699	0.1699	175	24
	Pyrazine	1	80.09	0.080	0.0805		
	MilliQ H_2O				10		
ES-II-94A	$AgNO_3$	1	169.87	0.1699	0.1708	130	24
	Pyrazine	1	80.09	0.080	0.0835		
	MilliQ H_2O				10		
ES-II-94B	$AgNO_3$	1	169.87	0.1699	0.1703	130	24
	Pyrazine	1	80.09	0.080	0.0838		
	MilliQ H_2O				10		
ES-II-95A	$AgNO_3$	1	169.87	0.1699	0.1705	70	1
	Pyrazine	1	80.09	0.0800	0.0812		
	MilliQ H_2O				10		
ES-II-95B	$AgNO_3$	1	169.87	0.1699	0.1713	70	1
	Pyrazine	1	80.09	0.0800	0.0848		
	MilliQ H_2O				10		

Table A2: SLUG-37 Synthesis

Sample ID	Reagents	Ratio (mmol)	F.W. (g/mol)	Target Mass (g)	Actual Mass (g)	Temperature (°C)	Time (days)
ES-II-40A	AgOAc	1	169.87	0.1699	0.1670	150	5
	Quinoxaline	1	130.15	0.1301	0.1301		
	EDSNa	1	234.16	0.2342	0.2347		
	MilliQ H_2O				10		
ES-II-43A	AgOAc	1	169.87	0.1699	0.1669	150	5
	Quinoxaline	1	130.15	0.1301	0.1327		
	EDSNa	1	234.16	0.2342	0.2342		
	MilliQ H_2O				10		
ES-II-43B	AgOAc	1	169.87	0.1699	0.1668	150	5
	Quinoxaline	1	130.15	0.1301	0.1324		
	EDSNa	1	234.16	0.2342	0.2343		
	MilliQ H_2O				10		
ES-II-43C	AgOAc	1	169.87	0.1699	0.1704	r.t.	3
	Quinoxaline	1	130.15	0.1301	0.1326		
	EDSNa	1	234.16	0.2342	0.2358		
	MilliQ H_2O				10		
ES-II-45C	AgOAc	1	169.87	0.1699	0.1675	50	1
	Quinoxaline	1	130.15	0.1301	0.1358		

	EDSNa	1	234.16	0.2342	0.2335		
	MilliQ H_2O				10		
ES-II-47B	AgOAc	1	169.87	0.1699	0.1669	50	1
	Quinoxaline	1	130.15	0.1301	0.1310		
	EDSNa	1	234.16	0.2342	0.2342		
	MilliQ H_2O				10		
ES-II-47C	AgOAc	1	169.87	0.1699	0.1662	r.t.	3
	Quinoxaline	1	130.15	0.1301	0.1325		
	EDSNa	1	234.16	0.2342	0.2321		
	MilliQ H_2O				10		
ES-II-55C	AgOAc	1	169.87	0.1699	0.1665	70	1
	Quinoxaline	1	130.15	0.1301	0.1306		
	EDSA	1	234.16	0.1902	0.1917		
	MilliQ H_2O				10		
ES-II-60B	AgOAc	1	169.87	0.1699	0.1666	150	2
	Quinoxaline	1.3	130.15	0.1669	0.1670		
	EDSNa	1	234.16	0.2342	0.2346		
	MilliQ H_2O				10		

Table A3: SLUG-38 Synthesis

Sample ID	Reagents	Ratio (mmol)	F.W. (g/mol)	Target Mass (g)	Actual Mass (g)	Temperature (°C)	Time (days)
JK-I-15	AgOAc	1	169.87	0.1699	0.1666	125	5
	Quinoxaline	1	130.15	0.1301	0.1316		
	MilliQ H_2O				10		
JK-1-23	AgOAc	1	169.87	0.1699	0.1669	125	5
	Quinoxaline	1	130.15	0.1301	0.1305		
	MilliQ H_2O				10		
JK-I-68A	AgOAc	1	169.87	0.1699	0.1695	150	3
	Quinoxaline	1	130.15	0.1301	0.1308		
	MilliQ H_2O				10		
JK-I-68B	AgOAc	1	169.87	0.1699	0.1669	125	5
	Quinoxaline	1	130.15	0.1301	0.1307		
	MilliQ H_2O				10		
ES-II-72	AgOAc	1	169.87	0.1699	0.1670	125	5
	Quinoxaline	1	130.15	0.1301	0.1303		

	MilliQ H_2O				10		
ES-II-73	AgOAc	1	169.87	0.1699	0.1660	100	5
	Quinoxaline	1	130.15	0.1301	0.1306		
	MilliQ H_2O				10		
ES-II-75A	AgOAc	1	169.87	0.1699	0.1653	125	5
	Quinoxaline	1.3	130.15	0.1669	0.1641		
	MilliQ H_2O				10		
ES-II-75B	AgOAc	1	169.87	0.1699	0.1673	125	5
	Quinoxaline	1.3	130.15	0.1669	0.1634		
	MilliQ H_2O				10		
ES-II-78	AgOAc	1	169.87	0.1699	0.1675	125	5
	Quinoxaline	1.3	130.15	0.1669	0.1671		
	MilliQ H_2O				10		
ES-II-83A	AgOAc	1	169.87	0.1699	0.1678	125	5
	Quinoxaline	1.3	130.15	0.1669	0.1667		
	MilliQ H_2O				10		
ES-II-83B	AgOAc	1	169.87	0.1699	0.1684	125	5
	Quinoxaline	1.3	130.15	0.1669	0.1727		
	MilliQ H_2O				10		

Table A4: CBN Synthesis

Sample ID	Reagents	Ratio (mmol)	F.W. (g/mol)	Target Mass (g)	Actual Mass (g)	Temperature (°C)	Time (days)
ES-I-36	$Cu(NO_3)$•2.5 H_2O	0.74	232.59	0.17	0.1724	140 °C- 24 h (5°/min) 90 °C -12 h(0.1°/min)	
	4,4-bipy	1.11	156.18	0.17	0.1751	70 °C -12 h(0.1°/min)	
	1,3,5-triazine	0.49	81.1	0.040	0.407	Cooled at r.t. (0.1°/min)	
	MilliQ H_2O				15		
ES-I-37	$Cu(NO_3)$•2.5 H_2O	0.74	232.59	0.17	0.1711	140 °C- 24 h (5°/min) 90 °C -12 h(0.1°/min)	
	4,4-bipy	1.11	156.18	0.17	0.1737	70 °C -12 h(0.1°/min)	
	1,3,5-triazine	0.49	81.1	0.040	0.0407	Cooled at r.t. (0.1°/min)	
	MilliQ H_2O				15		
ES-I-37	$Cu(NO_3)$•2.5 H_2O	0.74	232.59	0.17	0.1711	140 °C- 24 h (5°/min) 90 °C -12 h(0.1°/min)	
	4,4-bipy	1.11	156.18	0.17	0.1737	70 °C -12 h(0.1°/min)	
	1,3,5-triazine	0.49	81.1	0.040	0.0407	Cooled at r.t. (0.1°/min)	

	MilliQ H_2O				15	
ES-I-39	$Cu(NO_3)$•2.5 H_2O	0.74	232.59	0.17	0.1741	140 °C- 24 h (5°/min) 90 °C -12 h(0.1°/min)
	4,4-bipy	1.11	156.18	0.17	0.1735	70 °C -12 h(0.1°/min)
	1,3,5-triazine	0.49	81.1	0.040	0.0409	Cooled at r.t. (0.1°/min)
	MilliQ H_2O				15	
ES-I-41	$Cu(NO_3)$•2.5 H_2O	0.74	232.59	0.17	0.1768	140 °C- 24 h (5°/min) 90 °C -12 h(0.1°/min)
	4,4-bipy	1.11	156.18	0.17	0.1732	70 °C -12 h(0.1°/min)
	1,3,5-triazine	0.49	81.1	0.040	0.0443	Cooled at r.t. (0.1°/min)
	MilliQ H_2O				15	
ES-I-43	$Cu(NO_3)$•2.5 H_2O	0.74	232.59	0.17	0.1741	140 °C- 24 h (5°/min) 90 °C -12 h(0.1°/min)
	4,4-bipy	1.11	156.18	0.17	0.1735	70 °C -12 h(0.1°/min)
	1,3,5-triazine	0.49	81.1	0.040	0.0409	Cooled at r.t. (0.1°/min)
	MilliQ H_2O				15	
ES-I-55	$Cu(NO_3)$•2.5 H_2O	0.49	232.59	0..1133	0.1152	140 °C- 24 h (5°/min) 90 °C -12 h(0.1°/min)
	4,4-bipy	0.49	156.18	0.0765	0.0784	70 °C -12 h(0.1°/min)
	1,3,5-triazine	0.032	81.1	0.0258	0.0257	Cooled at r.t. (0.1°/min)
	MilliQ H_2O				10	
ES-I-72	$Cu(NO_3)$•2.5 H_2O	0.49	232.59	0..1133	0.1132	140 °C- 24 h (5°/min) 90 °C -12 h(0.1°/min)
	4,4-bipy	0.49	156.18	0.0765	0.0771	70 °C -12 h(0.1°/min)
	1,3,5-triazine	0.032	81.1	0.0258	0.0255	Cooled at r.t. (0.1°/min)
	MilliQ H_2O				10	
ES-I-78	$Cu(NO_3)$•2.5 H_2O	0.49	232.59	0..1133	0.1162	140 °C- 24 h (5°/min) 90 °C -12 h(0.1°/min)
	4,4-bipy	0.49	156.18	0.0765	0.0767	70 °C -12 h(0.1°/min)
	1,3,5-triazine	0.032	81.1	0.0258	0.02	Cooled at r.t. (0.1°/min)
	MilliQ H_2O				10	
ES-I-79	$Cu(NO_3)$•2.5 H_2O	0.49	232.59	0..1133	0.1154	140 °C- 24 h (5°/min) 90 °C -12 h(0.1°/min)
	4,4-bipy	0.49	156.18	0.0765	0.0758	70 °C -12 h(0.1°/min)
	1,3,5-triazine	0.032	81.1	0.0258	0.0261	Cooled at r.t. (0.1°/min)
	MilliQ H_2O				10	
ES-II-72	$Cu(NO_3)$•2.5 H_2O	0.74	232.59	0.17	0.1722	140 °C- 24 h (5°/min) 90 °C -12 h(0.1°/min)
	4,4-bipy	1.11	156.18	0.17	0.1765	70 °C -12 h(0.1°/min)

	1,3,5-triazine	0.49	81.1	0.040	0.0398	Cooled at r.t. (0.1°/min)
	MilliQ H_2O				10	

Table A5: FeMIL101-NH_2 Synthesis

Sample ID	Reagents	Ratio (mmol)	F.W. (g/mol)	Target Mass (g)	Actual Mass (g)	Temperature (°C)	Time (days)
ES-II-61	$FeCl_3.6H_2O$	0.2	270.3	0.054	0.0546	110	1
	2aminoterphthalic acid	0.2	181.15	0.0362	0.0366		
	DMF				15		
ES-II-62	$FeCl_3.6H_2O$	0.1664	270.3	0.45	0.4520	110	1
	2aminoterphthalic acid	0.8280	181.15	0.15	0.1501		
	DMF				10		
ES-II-63	$FeCl_3.6H_2O$	0.1664	270.3	0.45	0.4501	110	1
	2aminoterphthalic acid	0.8280	181.15	0.15	0.1518		
	DMF				10		
ES-II-62	$FeCl_3.6H_2O$	0.1664	270.3	0.45	0.4520	110	1
	2aminoterphthalic acid	0.8280	181.15	0.15	0.1501		
	DMF				10		
ES-II-74	$FeCl_3.6H_2O$	0.1664	270.3	0.45	0.4505	110	1
	2aminoterphthalic acid	0.8280	181.15	0.15	0.1543		
	MilliQ H_2O				10		

Table A6: 10%Zn-FeMIL101-NH_2 Synthesis

Sample ID	Reagents	Ratio (mmol)	F.W. (g/mol)	Target Mass (g)	Actual Mass (g)	Temperature (°C)	Time (days)
ES-II-75A	$FeCl_3.6H_2O$	0.150	270.3	0.405	0.4025	110	1
	$ZnCl_2$	0.1665	136.3	0.0227	0.0217		
	2aminoterphthalic acid	0.8280	181.15	0.15	0.1516		
	DMF				10		
ES-II-75B	$FeCl_3.6H_2O$	0.1664	270.3	0.45	0.4574	110	1
	$ZnCl_2$	0.1665	136.3	0.0227	0.0236		

	2aminoterphthalic acid	0.8280	181.15	0.15	0.1508		
	MilliQ H_2O				10		
ES-II-85	$FeCl_3.6H_2O$	0.150	270.3	0.405	0.4002	110	1
	$ZnCl_2$	0.1665	136.3	0.0227	0.0283		
	2aminoterphthalic acid	0.8280	181.15	0.15	0.1496		
	MilliQ H_2O				10		
ES-II-86	$FeCl_3.6H_2O$	0.150	270.3	0.405	0.4025	110	1
	$ZnCl_2$	0.1665	136.3	0.0227	0.0217		
	2aminoterphthalic acid	0.8280	181.15	0.15	0.1516		
	MilliQ H_2O				10		

Table A7: 20%Zn-FeMIL101-NH_2 Synthesis

Sample ID	Reagents	Ratio (mmol)	F.W. (g/mol)	Target Mass (g)	Actual Mass (g)	Temperature (°C)	Time (days)
ES-II-76A	$FeCl_3.6H_2O$	0.33	270.3	0.36	0.3617	110	1
	$ZnCl_2$	0.133	136.3	0.0454	0.0416		
	2aminoterphthalic acid	0.8280	181.15	0.15	0.1504		
	DMF				10		
ES-II-75B	$FeCl_3.6H_2O$	0.33	270.3	0.36	0.3611	110	1
	$ZnCl_2$	0.133	136.3	0.0454	0.0463		
	2aminoterphthalic acid	0.8280	181.15	0.15	0.1513		
	MilliQ H_2O				10		
ES-II-77	$FeCl_3.6H_2O$	0.33	270.3	0.36	0.3611	110	1
	$ZnCl_2$	0.133	136.3	0.0454	0.0463		
	2aminoterphthalic acid	0.8280	181.15	0.15	0.1513		
	MilliQ H_2O				10		
ES-II-83	$FeCl_3.6H_2O$	0.33	270.3	0.36	0.3611	110	1
	$ZnCl_2$	0.133	136.3	0.0454	0.0463		
	2aminoterphthalic acid	0.8280	181.15	0.15	0.1513		
	MilliQ H_2O				10		

ES-II-94	$FeCl_3.6H_2O$	0.33	270.3	0.36	0.3607	110	1
	$ZnCl_2$	0.133	136.3	0.0454	0.0452		
	2aminoterphthalic acid	0.8280	181.15	0.15	0.1517		
ES-II-95	$FeCl_3.6H_2O$	0.33	270.3	0.36	0.3608	110	1
	$ZnCl_2$	0.133	136.3	0.0454	0.0462		
	2aminoterphthalic acid	0.8280	181.15	0.15	0.1520		

Table A8: 30%Zn-FeMIL101-NH_2 Synthesis

Sample ID	Reagents	Ratio (mmol)	F.W. (g/mol)	Target Mass (g)	Actual Mass (g)	Temperature (°C)	Time (days)
ES-II-77C	$FeCl_3.6H_2O$	1.17	270.3	0.315	0.317	110	1
	$ZnCl_2$	0.5	136.3	0.068	0.0682		
	2aminoterphthalic acid	0.8280	181.15	0.15	0.1496		
	MilliQ H_2O				10		
ES-II-77D	$FeCl_3.6H_2O$	1.17	270.3	0.315	0.327	110	1
	$ZnCl_2$	0.5	136.3	0.068	0.0711		
	2aminoterphthalic acid	0.8280	181.15	0.15	0.1522		
	MilliQ H_2O				10		
ES-II-77G	$FeCl_3.6H_2O$	1.17	270.3	0.315	0.3158	110	1
	$ZnCl_2$	0.5	136.3	0.068	0.0701		
	2aminoterphthalic acid	0.8280	181.15	0.15	0.1517		
	MilliQ H_2O				10		
ES-II-77H	$FeCl_3.6H_2O$	1.17	270.3	0.315	0.3153	110	1
	$ZnCl_2$	0.5	136.3	0.068	0.0726		
	2aminoterphthalic acid	0.8280	181.15	0.15	0.1509		
	MilliQ H_2O				10		